Bright Linearly and Circularly Polarized Extreme Ultraviolet and Soft X-ray High Harmonics for Absorption Spectroscopy

by

Tingting Fan

B.S., University of Science and Technology of China, 2010
M.S., University of Colorado at Boulder, 2013

A thesis submitted to the
Faculty of the Graduate School of the
University of Colorado in partial fulfillment
of the requirement for the degree of
Doctor of Philosophy
Department of Physics
2017

This thesis entitled:
Bright Linearly and Circularly Polarized Extreme Ultraviolet and Soft X-ray High Harmonics for Absorption Spectroscopy
written by Tingting Fan
has been approved for the Department of Physics

____
Prof. Margaret M. Murnane

____
Prof. Henry C. Kapteyn

Date_______________

The final copy of this thesis has been examined by the signatories, and we find that both the content and the form meet acceptable presentation standards of scholarly work in the above mentioned discipline.

Fan, Tingting (Ph.D., Physics)
Bright Linearly and Circularly Polarized Extreme Ultraviolet and Soft X-ray High Harmonics for Absorption Spectroscopy
Thesis directed by Prof. Margaret M. Murnane and Prof. Henry C. Kapteyn

High harmonic generation (HHG) is an extreme nonlinear optical process. When implemented in a phase-matched geometry, HHG coherent upconverts femtosecond laser light into coherent "X-ray laser" beams, while retaining excellent spatial and temporal coherence, as well as the polarization state of the driving laser. HHG has a tabletop footprint, with femtosecond to attosecond time resolution, combined with nanometer spatial resolution. As a consequence of these unique capabilities, HHG is now being widely adopted for use in molecular spectroscopy and imaging, materials science, as well as nanoimaging in general. In the first half of this thesis, I demonstrate high flux linearly polarized soft X-ray HHG, driven by a single-stage 10-mJ Ti:sapphire regenerative amplifier at a repetition rate of 1 kHz. I first down-converted the laser to 1.3 μm using an optical parametric amplifier, before up-converting it into the soft X-ray region using HHG in a high-pressure, phase-matched, hollow waveguide geometry. The resulting optimally phase-matched broadband spectrum extends to 200 eV, with a soft X-ray photon flux of > 10^6 photons/pulse/1% bandwidth at 1 kHz, corresponding to > 10^9 photons/s/1% bandwidth, or approximately a three orders-of-magnitude increase compared with past work. Using this broad bandwidth X-ray source, I demonstrated X-ray absorption spectroscopy of multiple elements and transitions in molecules in a single spectrum, with a spectral resolution of 0.25 eV, and with the ability to resolve the near edge fine structure.

In the second half of this thesis, I discuss how to generate the first bright circularly polarized (CP) soft X-ray HHG and also use them to implement the first tabletop X-ray magnetic circular dichroism (XMCD) measurements. Using counter-rotating CP lasers at 1.3 μm and 0.79 μm, I generated CPHHG with photon energies exceeding 160 eV. The harmonic spectra emerge as a sequence of closely spaced pairs of left and right CP peaks, with energies determined by conservation of energy and spin angular momentum. I explain the single-atom and macroscopic physics by identifying the dominant electron quantum trajectories and optimal phase matching conditions. The first advanced propagation simulations for CPHHG reveal the influence of the finite phase matching temporal window on the spectrum, as well as the unique polarization-shaped attosecond pulse train. The first tabletop XMCD measurements at the $N_{4,5}$ absorption edges of Gd using this light source validate the high degree of circularity, brightness, and stability of this light source. These results demonstrate the feasibility of manipulating the polarization, spectrum and temporal shape of soft X-ray HHG by manipulating the driving laser waveform.

Finally, I present the first bright phase-matched CPHHG driven by lasers at wavelengths of 2 μm and 0.79 μm, which extends CPHHG to a broader wavelength combination and confirms the universal nature of this generation scheme. By analyzing the helicity dependent intensity asymmetry of CPHHG generated using different wavelengths and different gas targets, I show that the helicity dependent intensity asymmetry was mostly caused by the helicity dependent single-atom physics, which exhibits different behaviors for different gas targets. Moreover, the asymmetry can reverse and very interestingly, CPHHG from Ar exhibits a single helicity in the high-photon-energy region of the spectrum, which provide a convenient way to generate CPHHG with a single helicity and CP attosecond pulse trains. Finally, simple simulations and cutoff analysis of CPHHG provide guidance for generating CPHHG at higher photon energies.

Dedication

To my parents and my family.

Acknowledgements

I would like to thank my research advisors professor Margaret M. Murnane and Henry C. Kapteyn. I'm very grateful that they offered me a great opportunity to work in a big supportive research group. Thanks for their patience, guidance, and support in the past six years. Without their constant advice, this thesis will not be possible.

Many people helped with this thesis. I would like to thank Paul Arpin, Wei Xiong, and Chengyuan Ding for their contributions to the linearly polarized soft X-ray high harmonics generation and transient X-ray absorption spectroscopy experiment. I learnt a lot from them and I appreciate their help with that experiment. I'm very grateful to work with Tenio Popminchev, Ronny Knut, Patrik Grychtol, Carlos Hernández-García, Daniel D. Hickstein, Dmitriy Zusin, Christian Gentry, Franklin J. Dollar, Christopher A. Mancuso, Craig W. Hogle, Ofer Kfir, Dominik Legut, Karel Carva, Jennifer L. Ellis, Kevin M. Dorney, Cong Chen, Oleg G. Shpyrko, Eric E. Fullerton, Oren Cohen, Peter M. Oppeneer, Dejan B. Miloševic, Andreas Becker, and Agnieszka A. Jaroń-Becker on the project of circularly polarized soft X-ray high harmonics for X-ray magnetic circular dichroism. I appreciate their contributions to the project and help with the work.

I shared the same lab and laser with Daniel D. Hickstein, Jennifer L. Ellis, and Kevin M. Dorney. I'm grateful for their support as lab mates and their help with fixing the laser and sharing lab equipment. Since I used an optical parametric amplifier to generate high harmonics, so I had higher requirements about the laser

quality. I'm very grateful to people from KMLabs Xiaoshi Zhang, Daisy Raymondson, Mike Walls, and Amelie Auger for their help with fixing the laser. Thank Matt Seaberg, Dan Adams, Nathan Brooks, and David Couch for their help with the beam stabilization system. Thank Stacey Kuo for her help with developing silicon nitride windows. And thank group member Bosheng Zhang, Zhensheng Tao, Seth Cousin, Dennis Gardner, Jorge Nicolas, Chan La-o-vorakiat, Ellen Keister, Mingchang Chen, and all the other group members for their knowledge and assistance. I am grateful to work with these outstanding scientists, post-docs, and students.

I also would like to take this opportunity to thank all the members of my thesis committee: Prof. Margaret M. Murnane, Prof. Henry C. Kapteyn, Prof. Andreas Becker, Prof. Agnieszka A. Jaroń-Becker, and Prof. Ronggui Yang. It is my great honor to have them serve on my thesis committee. I also appreciate Prof. Tenio Popminchev for serving on my Comps III exam committee.

Finally I want to thank my friends for the great time we spent together and for making my PhD life joyful. I would like to give my deepest gratefulness to my parents, my older brother, and my older sister for their love, support, and everything. Lastly, I want to thank my husband for his companion, love, and support.

Contents

Chapter

Appendix

Figures

Figure

Chapter 1

Introduction

In this chapter, I will first discuss extreme ultraviolet (EUV) and soft-X-ray light sources and the main topic of this thesis. Then I will discuss the motivation of this thesis by presenting three applications that can be done using this unique new light source. Finally I will present the outline of this thesis.

1.1 Background

Light is a form of electromagnetic (EM) radiation - electric and magnetic fields traveling at the speed of light in vacuum that can be characterized by the wavelength or frequency of the EM waves. EM waves are produced whenever charged particles are accelerated, and these waves can subsequently interact with other charged particles – either on very large or small scales, enabling the radiation of EM waves with different wavelength or frequency. As Fig. 1.1 shows, the EM spectrum spans an extremely broad scale range, with wavelength ranging from 10^{-12} m to 10^{3} m, or with frequency ranging from 10^{4} Hz (radio frequency) to 10^{20} Hz (gamma rays). EUV radiation is EM radiation with wavelengths from 124 nm down to 10 nm, and therefore (by the Planck-Einstein equation) with photon energies from 10 eV up to 124 eV. Soft X-ray radiation has wavelengths from 10 nm to 0.1

nm, and therefore having photons with energies from 124 eV up to 12.4 keV. Nearly all types of EM radiation can be used for spectroscopy to study and characterize matter. Since the wavelengths of EUV and soft X-ray are on the scale of nanometer, they are extremely useful for applications that need nanometer resolution and extremely important for unrevealing the nano-world.

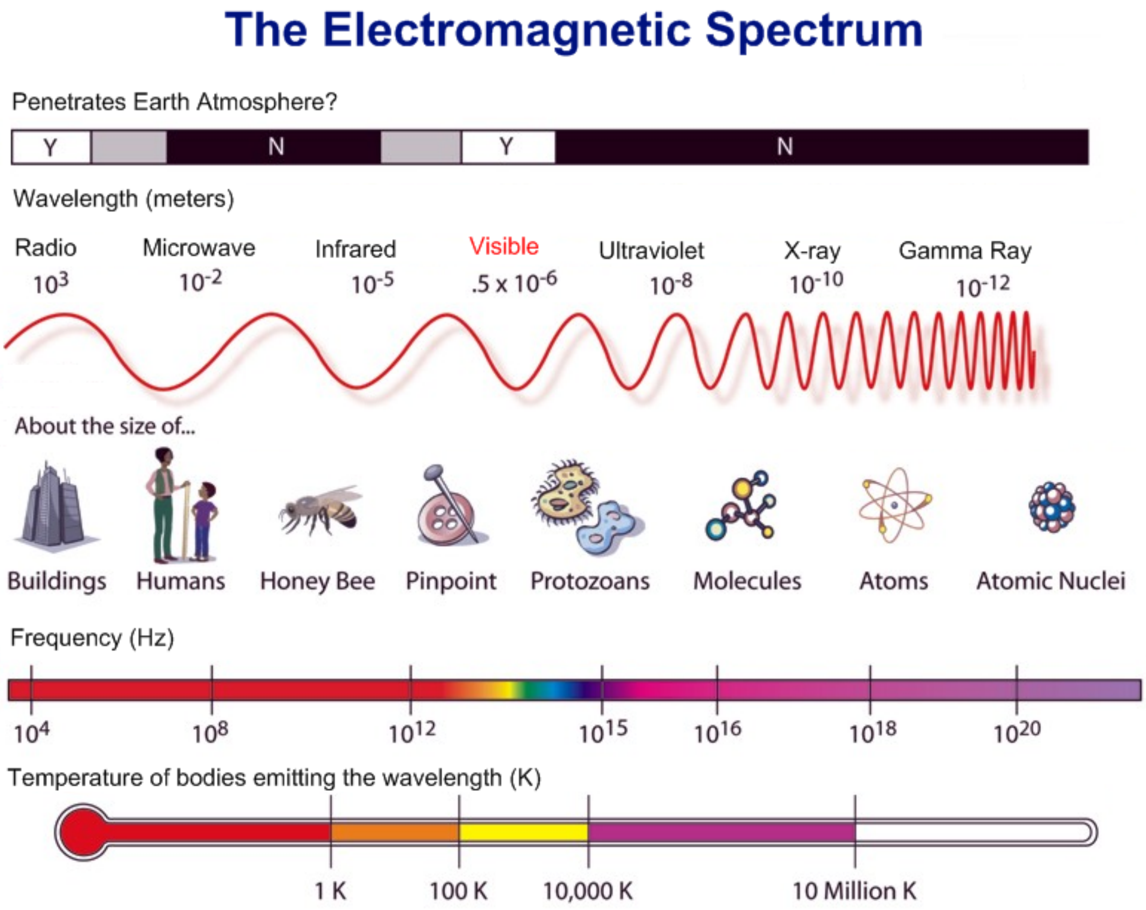

Figure 1.1: The EM spectrum. This figure is captured a NASA diagram.

EUV and soft X-rays are naturally generated by the solar corona. X-rays can be artificially generated by an X-ray tube, which is a vacuum tube that uses a high voltage to accelerate the electrons released by a hot cathode to a high velocity. The high velocity electrons collide with a metal target, the anode, creating the X-rays [1]. X-ray tubes find wide application in medical uses for radiography, computed tomography, Fluoroscopy, and Radiotherapy. However, X-ray tubes generate incoherent lights, limiting its ability in investigating coherent processes. Moreover, microscopic phenomena related to fundamental science and advanced technology often happen on nanosecond to even attosecond time scales. In order to study these ultrafast dynamics, pulsed EUV and soft X-ray beams with pulse duration on the same time scale will be needed.

The generation of coherent pulsed beams in the X-ray region of the spectrum has been pursued for many decades, because of the potential to combine the spatial and temporal coherence of lasers with the atomic-level spectroscopic and spatial resolution characteristics of X-rays. Partially coherent X-ray beams can be generated from large-scale synchrotron facilities; more recently, large-scale X-ray free electron lasers (XFELs) can generate high energy X-ray pulses with excellent spatial coherence, and with temporal coherence limited only by the availability of seeding and jitter between the laser and X-ray pulses [2-4]. However these facilities have kilometer in size and have limited access. Another way to generate pulsed EUV and soft X-rays is plasma-based light source, however this method generates incoherent or partially coherent light with pulse duration around 100 fs.

High-order harmonic generation (HHG), on the other hand, coherent upconverts light from a tabletop femtosecond laser in laboratories, while retaining excellent spatial coherence when implemented in a phase matched geometry, as well as temporal coherence that easily supports zeptosecond to attosecond synchronization with the driving laser [5-9]. Thus HHG provides an advanced light source complementary to facility-scale sources. By producing X-ray pulses with durations of <100 attoseconds [10-12] and wavelengths < 1 nm [7], HHG is opening up new research opportunities in molecular spectroscopy [13-16], materials science [17-23], as well as nanoscale coherent diffractive imaging [24, 25].

Most implementations of HHG used Ti:sapphire driving lasers at a wavelength around ~0.8 μm. In this case, phase matching considerations limit bright HHG to photon energies <≈100 eV, which lie in the EUV region of the spectrum. Phase-matched soft X-ray HHG can be generated, by using longer wavelength mid-infrared (IR) driving lasers, which can be obtained from Ti:sapphire laser pumped optical parametric amplifier (OPA). The efficiency of the HHG process scales rapidly with pulse energy, and requires mJ scale pulse energy to obtain absorption-limited conversion efficiency in the soft X-ray region [7, 26–29]. Thus requires a ~10-mJ pulse energy from the Ti:sapphire laser to pump OPA. The complexity of the traditional two-amplification-stage lasers greatly increases the cost and difficulty of implementing a tabletop HHG soft X-ray source reliably on a daily basis. Thus, the development of stable, compact, high pulse energy, ultrafast laser amplifiers that can generate multi-millijoule, few cycle, mid-IR laser pulses is required for efficient HHG.

In this thesis, I demonstrate a high flux soft X-ray HHG source with a flux of > 10^6 photons/pulse/1% bandwidth at 1 kHz (corresponding to > 10^9 photons/s/1% bandwidth) in a broadband, continuum spectrum extending to 200 eV, by using a compact single-stage 10-mJ 45-fs 1-kHz Ti:sapphire amplifier pumped three-stage OPA. This photon flux represents an approximately three orders-of-magnitude increase compared with past work, which used lower repetition rates, or non-phase matched implementations [27, 30]. Finally, using this unique bright supercontinuum soft X-ray HHG source, I discuss soft X-ray absorption spectroscopy (XAS) of multiple elements and transitions in molecules simultaneously with the ability to resolve near edge fine structure with high fidelity.

Recently the polarization state of HHG can be fully controlled by controlling the driving lasers waveform [31-33]. Polarization is a fundamental property of light and light-matter interaction. Full polarization control of EUV and soft X-ray beams is very useful for scientific research and advanced technology such as studying ultrafast magnetism [34], probing nano-structures and chiral phenomena [35]. People have made lots of efforts to generate circularly polarized (CP) EUV and soft X-ray beams. One way is to modify the undulators of large facilities (synchrotron and free electron lasers), which is very complex [36, 37]. Many applications have been successfully demonstrated using these sources, such as X-ray magnetic circular dichroism (XMCD) measurement of Gd/Fe [34]. People also tried to convert linearly polarized (LP) EUV and soft X-ray beams to circular polarization using optics [38]. However, EUV and X-ray optics are challenging to fabricate and have limited throughput and bandwidth. This method reduces the photon flux by two orders of magnitude and people need to careful design the trade off between the transmission efficiency, covered spectral range, and circularity.

HHG, a unique EUV and soft X-ray light source, was limited to linear polarization for a long time. HHG inherits the polarization nature of the driving laser field. In order to generate CPHHG, the most natural way people think about is to use a CP laser beam. However a CP laser beam will introduce too much transverse displacement to the ionized electron that the electron will miss its parent ion, so no harmonics will be generated.

People have made lots of effect to generated CPHHG, such as HHG in pre-aligned molecules using LP laser fields [39], this method needs an extra pump laser beam to align the molecule first, which is more complicated and can only achieve limited circularity. Another interesting method people recently developed is resonant HHG in elliptical laser fields [40], however the harmonics have limited circularity and are hard to scale to higher photon energies. Also recently people generate CPHHG by using cross-polarized two-color laser fields [41], again this method achieves limited circularity and only generate CPHHG in the EUV region so far. Recently, CPHHG is generated by using two-color counter-rotating CP lasers in non-colinear geometry [42], this method allows angular separation of left and right CPHHG, even allows the separation of different harmonic orders without a spectrometer. Because of the phase matching geometry, the pressure needed to achieve full phase matching is higher in this geometry. While the non-collinear geometry makes it challenging to achieve high gas pressure in the interaction region, so extending CPHHG in non-collinear geometry to higher photon energy strongly depends on the design of the gas cell.

The method I use to generate CPHHG in the EUV and soft X-ray region is using two-color counter-rotating CP laser fields in collinear geometry [31-33]. This is the first method allows the generation of CPHHG beams in the soft X-ray spectral region [33]. This method was first proposed over twenty years ago [43], however, the polarization state was not measured at the moment. And since phase matching is not well studied yet at that moment, bright phase-matched beams were not generated. Later on, theorists did theoretical study of this method from single-atom view [44-49]. Recently the polarization of high harmonics generated using this method is measured to be circular [31]. After that, bright phase-matched CPHHG are generated in the EUV and soft X-ray spectral region [32-33]. And this method has inspired wide studies [50-56].

1.2 Motivation

XAS is a powerful and widely used technique for determining the local geometric and/or electronic structure of matter, as well as charge transfer processes in gas, liquid, and solid phase. Moreover, utilizing the energy dependent absorption of X-rays, XAS can be used to obtain information about the elemental composition of the sample. Most XAS experiments were implemented using large-scale facilities. In the experiment shown in Fig. 1.2, which investigates XAS dynamics of aqueous $[Ru^{II}(bpy)_3]^{2+}$ using a synchrotron source. The authors were able to resolve the charge transfer dynamics after photo-excitation. However, the limited time resolution prevents monitoring the initial fast dynamics as the electronic structure evolves over the first ≈100 fs after the initial excitation [57]. With its unique advantages, HHG allows a much higher time resolution with tabletop size and wide accessibility. Thus, the development of compact, reliable, kHz, high flux, supercontinuum soft X-ray HHG light source is strongly motivated.

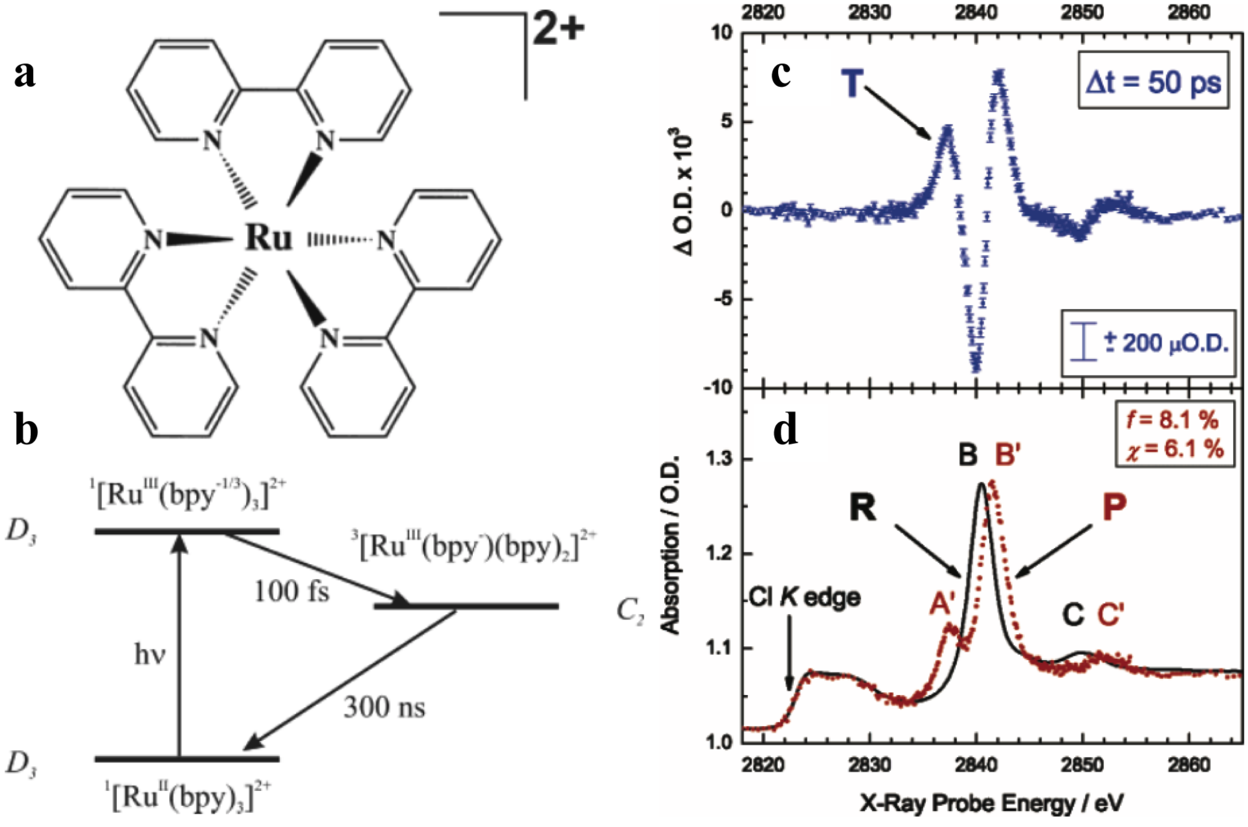

Figure 1.2: (a) Static structure of $[Ru^{II}(bpy)_3]^{2+}$, which is a model system for metal-to-ligand charge transfer process. (b) Photochemical reaction cycle of $[Ru^{II}(bpy)_3]^{2+}$.

An electron moves from the Ru core to the ligands after excitation. After 100 fs, the electron localizes to one of the ligands. Then decays back to the ground state on a 300-ns timescale. (c) Transient X-ray absorption spectrum at 50 ps after laser excitation. (d) Static X-ray absorption spectrum of the L_{III} edge of Ru in ground-state $[Ru^{II}(bpy)_3]^{2+}$ (black trace R), and excited-state absorption spectrum (red trace P) corresponding to the curve in (c). This figure is captured from [57].

EUV and soft X-ray CPHHG can be used to study magnetic materials, nanostructures, and chiral phenomena. XMCD is a kind of XAS of magnetic materials, which measures the differential absorption change of magnetic materials in a magnetic field when the magnetization direction is kept the same for left- and right- CP incident beams, or when the helicity of the incident beam is kept the same for different magnetization directions. By analyzing the XMCD signal, information can be obtained on the magnetic properties of the atom, such as its spin and orbital magnetic moment. This technique has very high sensitivity and allows element specific magnetic properties study. Most XMCD experiments were implemented using large-scale facilities as an example shown in Fig. 1.3(a,b). In this experiment, the authors use the element-specific technique XMCD to study spin reversal in GdFeCo that is optically excited by an ultrafast pump pulse. The authors unexpectedly find that the ultrafast spin reversal in this material, where spins are coupled antiferromagnetically, occurs by way of a transient ferromagnetic-like state [34]. These studies provide concept for the possibility of manipulating magnetic order on the timescale of the exchange interaction, which is useful for ultrafast magnetic storage and spintronics.

Photoelectron Circular Dichroism (PECD) is a relatively novel technique that measures the difference of the photoelectron angular distribution from ionization with left- and right- CP light as shown in Fig. 1.3(c). PECD shows strong asymmetries, typically lying in the 1 to 30 % range, and provides rich 3D data, which can be used to detect chirality in molecules with high sensitivity and to study chiral phenomena. PECD experiments were mostly performed using large-scale facilities [35]. With the demand of those exciting applications, EUV and soft X-ray CPHHG light source, which provides better time resolution, tabletop size, and wide accessibility, is strongly motivated.

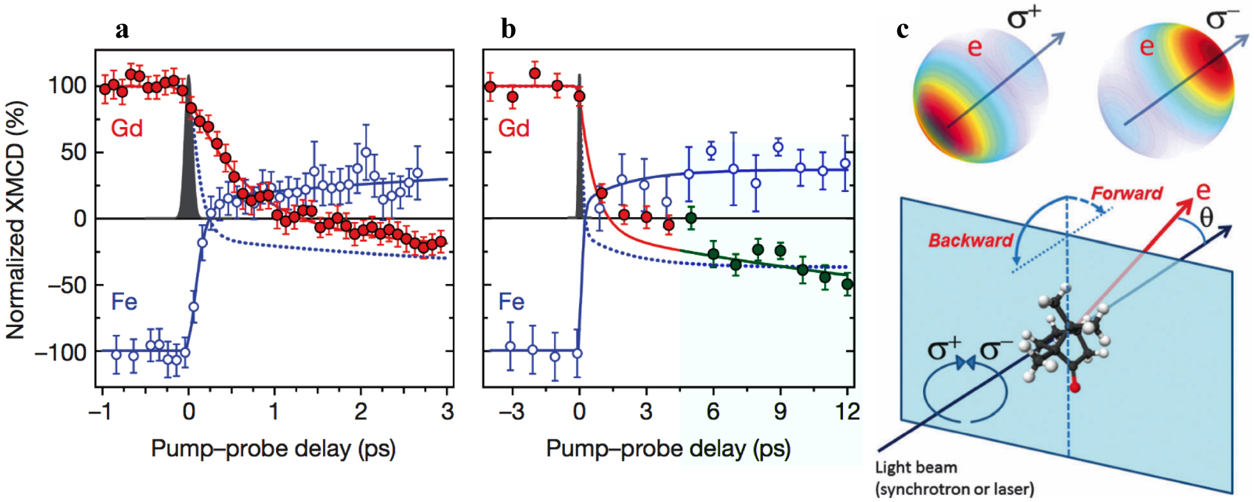

Figure 1.3: (a) Transient magnetic moment dynamics of the Fe (open circles) and Gd (filled circles) measured within the first 3 ps. (b) As (a) but on a 12-ps timescale. The dashed line in both panels depicts the magnetization of the Fe sublattice taken with the opposite sign of the measured Fe data. This figure is captured from [34]. (c) The concept of PECD. The full 3D angular distribution of photoelectrons is imaged after photoionization with either left- or right- CP light. The angle θ is the angle between the direction of the CP beam and the velocity of the electron. The photoelectron angular distribution of a chiral molecule will show a forward–backward asymmetry that reverses in sign when switching from R- to S-enantiomer. This figure is captured from [35].

1.3 Thesis outline

This thesis is organized as follows. It contains four chapters. In the first chapter, I talked about the background and motivation of this thesis. In the second chapter, I will discuss EUV and soft X-ray LPHHG. I will first discuss the history of HHG. Then the physics of HHG from single-atom view, including ionization, propagation, and recombination, i.e. the three-step model, will be presented. After that, I will write about the macroscopic physics of HHG including phase matching, critical ionization, and gas reabsorption. Finally, I will show our work of improving the flux of LPHHG in the soft X-ray region by three orders-of-magnitude by using a single-stage, 10-mJ Ti:sapphire regenerative cavity amplifier pumped three-stage OPA. At the end of the second chapter, I will briefly summarize what I discussed in the chapter.

In the third chapter, I will talk about XAS using soft X-ray LPHHG. I will first discuss the background of XAS technique. Then I will show the experimental setup and static near edge X-ray absorption fine structure (NEXAFS) results in gas, liquid, and solid phase. Moreover, the measurement of transient EUV absorption spectroscopy of Xe will be presented. Finally I will summarize the content of the chapter.

In the forth chapter, I will present the development of the first soft X-ray CPHHG and use it for XMCD measurement of Gd/Fe multilayer. I will first introduce the topic. Then, I will show soft X-ray CPHHG driven by two-color counter-rotating CP laser fields at wavelengths of 1.3 μm and 0.79 μm. The spectral and temporal structure of CPHHG will be discussed. And the single-atom and macroscopic physics of CPHHG will be explained, by identifying the dominant electron quantum trajectories and optimal phase matching conditions. The first advanced propagation simulations for CPHHG reveal the influence of the finite phase matching temporal window on the spectrum, as well as the unique polarization-shaped attosecond pulse train. What's more, the polarization of CPHHG will be analyzed using a simple photon model and advanced simulations. The first tabletop XMCD measurements at the $N_{4,5}$ absorption edges of Gd is presented to validate the high degree of circularity, brightness, and stability of this light source. Moreover, flux characterization of CPHHG will be presented, which shows a similar flux level with LPHHG.

In the second half of the forth chapter, I will present CPHHG driven by two-color counter-rotating CP laser fields, for the first time, at wavelengths of 2 μm and 0.79 μm. The spectral structure will be discussed. And helicity dependent intensity asymmetry of CPHHG will be analyzed and discussed. After that, I will present the cutoff behavior of CPHHG by comparing with LPHHG cutoff of the two driving laser beams, which provide guidance about generating higher-photon-energy CPHHG. Then future directions of CPHHG will be discussed. Finally CPHHG driven by two-color counter-rotating CP fields in non-collinear geometry will be briefly discussed. And at the end the chapter, a summarization will be presented.

Chapter 2

Bright linearly polarized soft X-ray high harmonics

In this chapter, I will first discuss the background of HHG. Then the single-atom and macroscopic physics of HHG will be presented. Finally, I will show the development of EUV and soft X-ray LPHHG light source driven by a single-stage 10-mJ 1-kHz Ti:sapphire regenerative cavity amplifier pumped three-stage OPA. At the end, I will briefly summarize what I discussed in this chapter.

2.1 Background

HHG is an extreme nonlinear effect upconverting many low-energy photons to a single high-energy photon when a strong laser field is focused onto a dense medium of gas atoms. The laser peak intensity needed to drive the HHG process is about 10^{13} to 10^{15} W/cm^2. So HHG greatly relies on the development of high-peak-power laser systems and nonlinear optics. In 1960, Theodore H. Maiman built the first laser at Hughes Research Laboratories based on theoretical work by Charles H. Townes and Arthur L. Schawlow [58, 59]. Shortly after the construction of the first laser, Peter Franken et al. at University of Michigan discovered second harmonic at 347.2 nm in 1961 upon projection of an intense laser beam with a 10^7-W/cm^2 intensity and a 694.3-nm wavelength through crystalline quartz [60]. In

1962, R. W. Terhune, P. D. Maker, and C. M. Savage observed the first optical third harmonic generation in calcite [61] and later on reported third harmonic generation in crystals, glasses, and Liquids [62]. G. H. C. New and J. F. Ward reported the observation of the first third harmonic generation in gas in 1967, particularly in He, Ne, Ar, Kr, and Xe, the motivation for their study of these gases was that the nonlinear susceptibilities are relatively amenable to quantum-mechanical calculation [63]. Because of the relatively weak field intensity used, these harmonics fall into the perturbative regime, which is characterized by rapidly decreasing efficiency with increasing harmonic order because the probability of absorbing n photons decreases as n increases [64].

In 1977, the first HHG was observed in the interaction of intense CO_2 laser pulse, at intensity of > 10^{14} W/cm^2 and wavelength of 10.6 μm, with plasma generated from planar solid targets up to the eleventh harmonic (0.95 μm) [65]. HHG in gases, far more developed and widespread in applications today, was first observed by A. McPherson and colleagues in 1987 by using intense ultraviolet (248 nm) beam at intensity of 10^{15} – 10^{16} W/cm^2 from rare gas, the highest harmonic observed was the seventeenth (14.6 nm) in Ne [66]. Later on in 1988, M. Ferray et al. reported the observation of harmonics as high as 33rd harmonic (32.2 nm) by using Nd: YAG laser radiation from rare gas at intensity of about 10^{13} W/cm^2 [67]. Those harmonics exhibit very different spectrum than earlier very-low-order harmonics. The spectrum contains three regions exhibiting very different behaviors: low-order-harmonics region, the plateau region, and the cutoff region. The intensity of the low-order harmonics decreases as the harmonic order increase as expected from the perturbative theory. In the plateau region, the intensity of the harmonics is found to remain approximately constant over many harmonic orders. And in the cutoff region, the intensity of the harmonics drops abruptly, the end position is called the cutoff [68]. This very-different harmonic spectrum can't be explained by traditional perturbative theories because of the high field intensity used. HHG process is light-matter interaction in the non-perturbative regime and needs to be explained by non-perturbative theories.

Thanks to the introduction of solid-state active materials and of new mode-locking and amplification techniques, the 1990s have seen a revolution in ultrafast laser technology [69]. Ultrafast light sources today are "turnkey" devices, routinely delivering ultrafast light beams with pulse duration as short as 20 fs and with peak field intensity of 10^{15} W/cm^2 at 1-kHz repetition rate. The development of laser technology and nonlinear optics greatly facilitate the advancement of HHG in directions of higher flux, higher cutoff, and shorter pulse duration. First, HHG cutoff has been greatly increased by using laser pulses with higher intensity and shorter pulse duration [70], noble gas with higher ionization potential [71], and laser beams with longer wavelength [27]. HHG with photon energy greater than 1.6 keV has been generated experimentally by using laser beam at a wavelength of 3.9 μm [7]. Second, the pulse duration of HHG has been greatly decreased [72, 73] and isolated attosecond pulses have been generated, by using techniques of polarization gating [74], peak-field intensity gating [10, 12], and phase-matching gating [75]. What's more, HHG flux has been greatly increased by controlling the driving laser waveform [28] and using much better phase-matching geometries, such as hollow-core waveguides [5] and quasi-phase-matching techniques [76, 77].

Now HHG is a well-developed "laser like" light source, routinely available in labs from the vacuum ultraviolet (VUV) to the soft X-ray spectral region with unique advantages of tabletop size, femtosecond to attosecond time resolution, nanometer spatial resolution, and fully spatially and temporally coherent. As a consequence, HHG is widely used for scientific research, such as nanoimaging, molecular dynamics and imaging, nanoscale energy transport, ultrafast surface science, ultrafast magnetics, and so on. Moreover, people can control the properties of HHG to meet the needs for different applications. In the temporal domain, an attosecond pulse train or an isolated attosecond pulse can be generated. In the spectral domain, HHG at different photon energies from the VUV spectral region up to 1.6 keV can be generated, and a broadband supercontinuum or multiple harmonic peaks or an isolated harmonic peak can be generated. Besides, recently the polarization of HHG can be fully controlled from linear to circular as will be discussed in chapter 4. Although HHG light source is mostly used in academic research so far, it is also very possible to see HHG being used in industry, such as in semiconductor metrology devices and precision measurement devices in the future.

In this chapter, I will first discuss the microscopic physics of HHG. Because of the strong laser field used, non-perturbative theory is required to explain the HHG phenomenon. In 1992 and 1993, a theory breakthrough was made by J. L. Krause et al. [78] and P. B. Corkum [79]. They presented a semiclassical theory from single-atom view and successfully reproduce the spectral features of HHG. According to this work, HHG can be successfully explained by a simple three-step model. As Fig. 2.1 shows, when a strong laser field, with an intensity that is comparable to the Coulomb potential bounding the outmost electron of the atom, is focused on the atom, first, the electron can be tunnel ionized from the ground state of the atom and set free in the continuum. Second, the electron moves in the continuum under the force of the laser electric field, the electron is first accelerated away from its parent ion, then accelerated back towards its parent ion when the oscillating laser electric field changes its sign. Finally, the electron has a chance to recombine with its parent ion and releases its kinetic energy acquired in the laser field plus the ionization potential by emitting a high-energy photon. From this model, J. L. Krause et al. showed that the cutoff energy of HHG follows a universal law of $I_p + 3.17U_p$, where I_p is the ionization potential, and $U_p = \frac{e^2E_0^2}{4m_e\omega_0^2}$ is the ponderomotive energy, i.e. the mean kinetic energy acquired by an electron oscillating in the laser field. Here, e is the electron charge, m_e is the electron mass, E_0 and ω_0 are the laser electric field and its frequency, respectively. This model was confirmed later by advanced quantum theory based on strong-field approximation (SFA) by M. Lewenstein et al. [80].

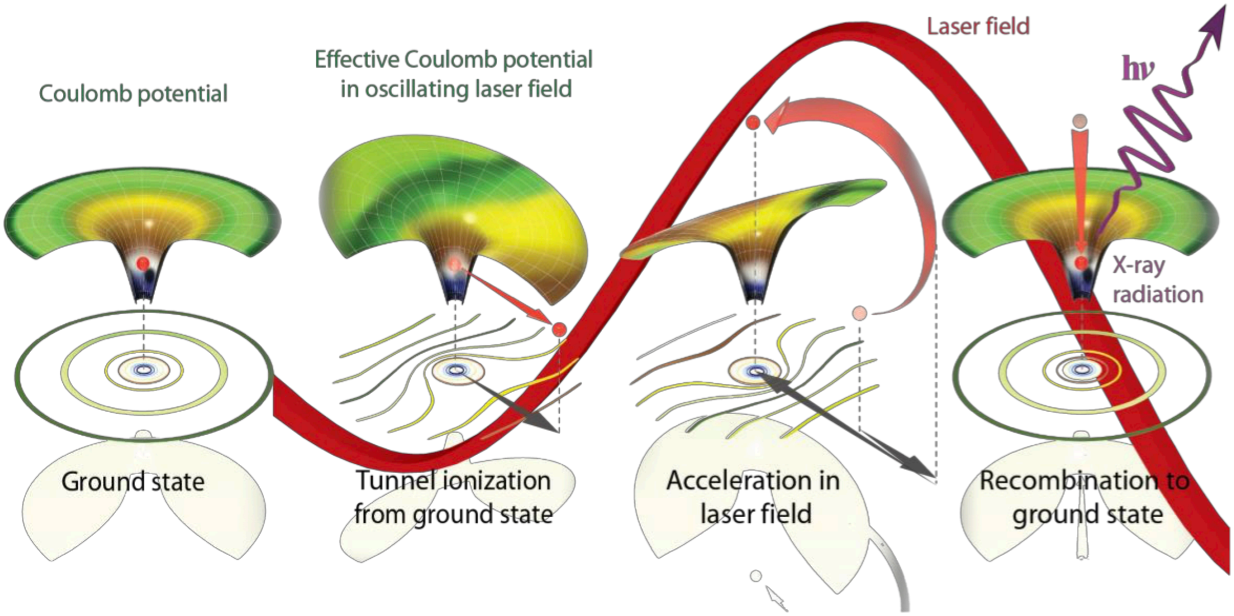

Figure 2.1: Cartoon of the three-step model. The Coulomb potential of an atom with an electron initially in its ground state is strongly perturbed by an oscillating intense laser field. The electron is tunnel ionized through the effective Coulomb potential from its ground state. After ionization, the free electron is first accelerated away from the ion and then accelerated back towards the ion when the laser field switches direction. Finally the electron recollides with its parent ion, giving off excess energy in the form of a high-energy photon. This figure is captured from [81].

Because of the quantum diffusion of the recolliding-electron wavepacket and the quadratic increase in the cutoff energy as a function of the driving-laser wavelength, HHG efficiency from a single atom is super small, scaling as $\lambda^{-5.5}$ to $\lambda^{-6.5}$, where λ is the wavelength of the driving laser field [82-84]. Fortunately, HHG involves light emission from tons of atoms. When the emitted harmonic beam travels in phase with the driving laser beam, all the emitted harmonics are phase matched and can add up constructively, thus a bright HHG beam can be generated. Both the driving laser beam and the HHG beam propagate in a gaseous medium, in order to achieve good phase matching, the macroscopic effect of HHG, i.e. the response of the whole medium, needs to be studied. So later on in this chapter the macroscopic physics of HHG including phase matching, critical ionization, and gas reabsorption will be discussed.

2.2 High harmonic generation from single-atom view

As introduced earlier, from single-atom view, HHG process is completed by three steps: ionization, propagation, and recombination. This is very similar to how a conventional X-ray tube works as shown in Fig. 2.2. Heated filament emits electrons, the electrons are then accelerated by a high voltage, finally X-rays are produced when the high-speed electrons hit the metal target [85]. X-ray tubes convert electric power to X-rays, while HHG converts laser power to X-rays. The single-atom model not only provides a simple intuitive picture of how HHG works, but also reveals the underlying physics and provides a way to calculate the cutoff and single-atom yield of HHG. In this section, I will discuss the three steps separately and show how the cutoff law and single-atom yield of HHG are deducted from this model.

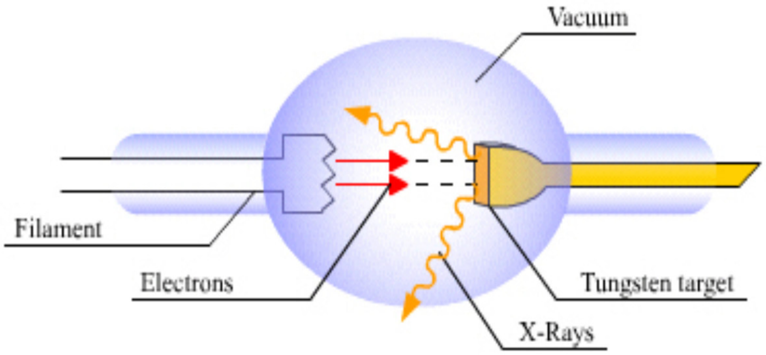

Figure 2.2: Operating principle of X-ray tubes. Heated filament emits electrons, which are then accelerated by a high voltage, finally X-rays are produced when the high-speed electrons hit the metal target. This figure is captured from [85].

2.2.1 Ionization

In the first step of HHG, the electrons are ionized, so in order to understand HHG, it is essential to understand the ionization mechanism first. What's more, in order to generate bright HHG beams, it is essential to know the composition of the medium through which the laser field travels to achieve phase matching, so it is essential to calculate the ionization rate. I will discuss the first question, after that come to the second one.

There are three different ionization mechanisms: multiphoton ionization, tunneling ionization, and barrier suppression ionization as shown in Fig. 2.3. L. V. Keldysh introduced a parameter, known as the Keldysh parameter, to distinguish these three regimes of ionization [86, 87]. Keldysh parameter is the ratio of the tunneling time to the optical period of the laser, where tunneling time is estimated by the width of the barrier divided by the electron velocity. Keldysh parameter is given by:

$$\gamma = \sqrt{\frac{I_p}{2U_p}} \qquad (2.1)$$

Here I_p is the ionization potential, and U_p is the ponderomotive energy as mentioned earlier.

When $\gamma >> 1$, the driving laser has low intensity but high single photon energy. The binding coulomb potential is slightly distorted, and the light-matter interaction is still in the perturbative region, so the multiphoton excitation route for ionization applies as shown in Fig. 2.3(a). When $\gamma < 1$, the atom is exposed to a high-power laser at a low frequency, the atomic potential can be significantly distorted that a potential barrier is formed. Since the frequency of laser is low such that the electron can respond to this changing potential, the electron can tunnel through the static potential barrier in a time less than half the field period as shown in Fig. 2.3(b). When $\gamma << 1$, an extremely strength laser field can completely suppress the potential barrier and the electron will flow over the barrier, known as barrier-suppressed ionization as shown in Fig. 2.3(c) [86, 87].

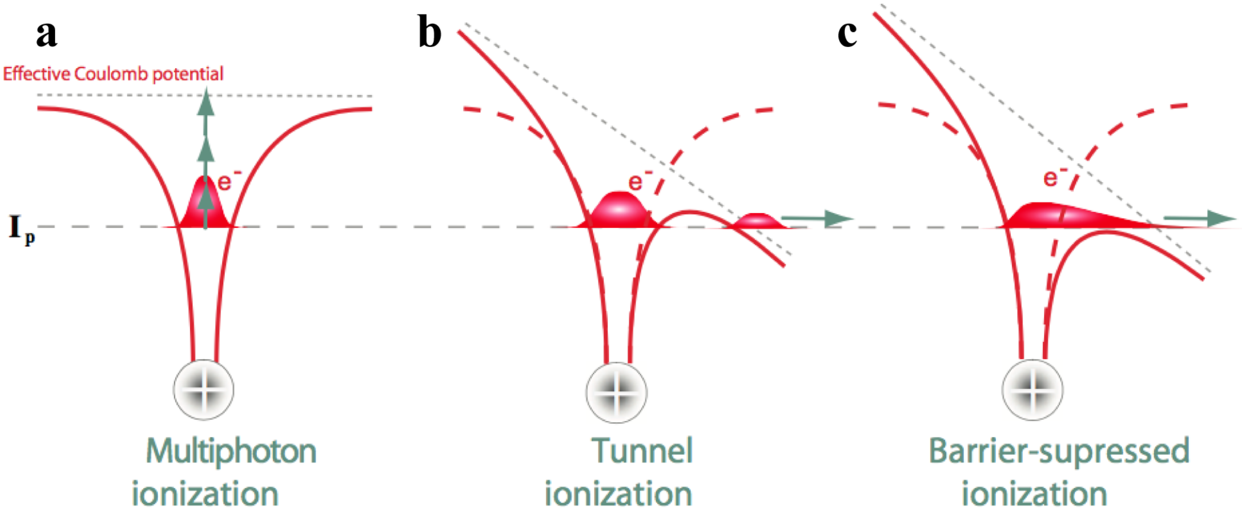

Figure 2.3: Strong-field ionization scenarios. Exposing an atom to an intense laser field will result in an effective potential (solid red line) composed of the Coulomb potential (dashed red line) and the oscillating laser field. At different laser intensities, the electron can be ionized under different mechanisms. This figure is captured from [88].

Tunneling ionization is essential for bright HHG emission because we need a strong laser field to ionize enough atoms to generate bright HHG. However, if the driving laser intensity is too strong, very dense free electrons can be produced that too much dispersion is introduced, preventing HHG from phase matching. For tunneling ionization, the electric field can be regarded as a quasi-static perturbation to the Coulomb potential. In 1986, Ammosov, Delone and Krainov [89] presented a generalized analytical theory, which is known as the ADK ionization theory, to calculate the ionization rate for arbitrary atoms and initial electronic states. The calculated ionization rate is known as the ADK ionization rate:

$$W_{ADK}(t) = -\frac{1}{N(t)}\frac{dN(t)}{dt} = \sqrt{\frac{3E(t)}{\pi(2I_p)^{\frac{3}{2}}}}\,|C_{n*l*}|^2 f(l,m) I_p \left(\frac{2(2I_p)^{\frac{3}{2}}}{E(t)}\right)^{\left(\left({}^{2Z}\!/\!\sqrt{2I_p}\right)-|m|-1\right)} exp\,(-\frac{2(2I_p)^{3/2}}{3E(t)}) \tag{2.2}$$

Where $N(t)$ is the number of neutral atoms at time t, Z is the ion charge (once the electron is detached), I_p is the ionization potential of gas (24.59 eV for He, 21.56 eV for Ne, 15.76 eV for Ar, 14 eV for Kr, and 12.13 for Xe), $E(t)$ is the laser electric field, l and m are the angular momentum and magnetic quantum number, respectively (in atomic units, $\hbar = m = e = 1$). The factor $f(l,m)$ and the constant $|C_{n*l*}|^2$ are given by:

$$f(l,m) = \frac{(2l+1)\,(l+|m|)!}{2^{|m|}\,(|m|)!\,(l-|m|)!}$$

$$|C_{n*l*}|^2 = \frac{2^{2n*}}{n*\,\Gamma(n*\ +l*\ +1)\,\Gamma(n*\ -l*)}$$

Here the effective principal and angular momentum quantum number are given by $n* = Z\,(2I_p)^{-1/2}$ and $l* = n*\ -1$, respectively. $\Gamma(x)$ is Gamma function defined as $\Gamma(x) = \int_0^{\infty} e^{-t} t^{x-1} dt$.

When the ionization is first-order kinetic (neutral atom → ion + e-), the ratio of the number of ions $(N_0 - N(t))$ to the initial number of atoms N_0 is defined as the ionization fraction $\eta(t) = 1 - \frac{N(t)}{N_0}$ can be calculated from equation:

$$\eta(t) = 1 - exp\left[-\int_{-\infty}^{t} W_{ADK}(t')dt'\right] \qquad (2.3)$$

The ADK ionization rates provide a quick and relatively simple way to numerically estimate the ionization level of gas in a strong laser field. From this ionization rate, real time density of free electrons and ions, as well as real time density of neutral atoms can be calculated. Thus the introduced dispersion by neutral atoms and plasmas while the driving laser propagating through the medium can be calculated, from which the phase mismatch between the driving laser field and the emitted harmonic fields can be calculated, which will be discussed in details in section 2.3. Since ionization happens at the peak of the laser field, during the first half of the laser pulse, the ionization fraction behaves like a step function where ionizations occur mostly at crests and troughs of the laser field (ionization occurs every half the optical cycle). While during the second half of the laser pulse, the ionization fraction statutes at some point of time when the magnitude of the laser field becomes smaller. The tunneling ionization level can be precisely estimated by the ADK model, and it turns out the ionization rate is very sensitive to the driving laser intensity, while is almost independent of the driving laser wavelength [89].

2.2.2 Propagation

Once the electron is tunnel ionized, it propagates under the external force applied by the laser electric field. Trajectories of the electron can be analytically calculated by Newton's Second Law [90]. The electron is initially bound to an atom at $x = 0$, and is tunneled into the continuum at time $t = 0$ with an initial velocity $v(0) = 0$ [91], the velocity $v(t)$ and the position $x(t)$ of the free electron, born at arbitrary phase ϕ of the oscillating laser field can be calculated by the following equations:

$$\ddot{x(t)} = \frac{eE_0}{m_e} cos(\omega_0 t + \phi) \qquad (2.4)$$

$$v\,(t) = \dot{x(t)} = \frac{eE_0}{m_e \omega_0}(sin(\omega_0 t + \phi) - sin\,(\phi)\,) \qquad (2.5)$$

$$x\,(t) = -\frac{eE_0}{m_e \omega_0^2}(cos(\omega_0 t + \phi) - cos\,(\phi)) - \frac{eE_0}{m_e \omega_0} sin\,(\phi) t \qquad (2.6)$$

Here e is the electron charge, m_e is the mass of electron, E_0 is the envelop of the laser field, which can be approximated to be constant in the propagation step since the whole process takes place in half optical cycle of the pulse, which is much smaller than the amplitude variation of the envelop. ω_0 is the frequency of the laser electric field. From equation 2.6, we can tell whether the electrons starting from the atomic core located at $x = 0$ can return back to the core or not, which depends on the initial phase ϕ. For the phase of $0 < \phi < \pi/2$, the electron trajectory crosses the core at $x = 0$, which means the electron returns back to the core. However, for the phase of $\pi/2 < \phi < \pi$, the electron drifts away from the ion and never returns. From equation 2.5, we can calculate the kinetic energy of the returning electron as $E_{KE} = \frac{1}{2} m_e v_f^2$, here v_f is the velocity when the electron returns back to the core. As Fig. 2.4 shows, when the initial phase $\phi = 17^o$, the electron gains the maximum kinetic energy of 3.17 U_p when it returns back to the core. Below the cutoff, two kinds of trajectories, short trajectories and long trajectories, lead to the same final kinetic energy.

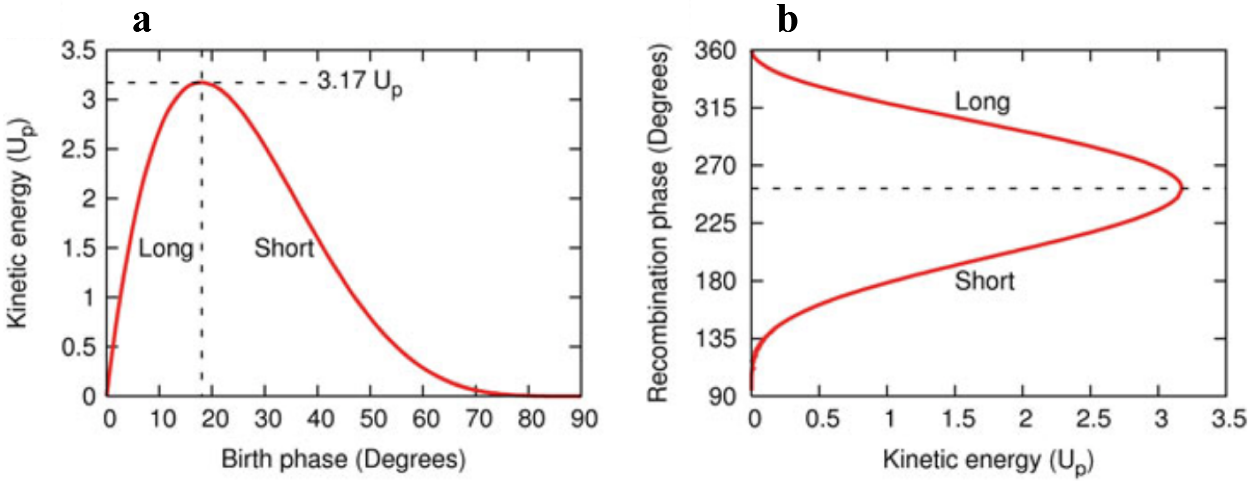

Figure 2.4: (a) Plot of the kinetic energy of the returning electron as a function of its birth phase. (b) Plot of the recombination phase of the returning electron as a function of its kinetic energy. The kinetic energy reaches a maximum of $3.17 U_p$ at the birth phase of 17◦. This figure is captured from [92].

2.2.3 Recombination

Once the electron returns to its parent ion, it has a chance to recombine with its parent ion and goes to its initial ground state giving off any excess energy (its kinetic energy plus the ionization potential I_p) in the form of a high-energy photon. So the photon energy of the emitted photon is:

$$w = I_p + E_{KE} \qquad (2.7)$$

Since the maximum kinetic the electron can gain in the laser field is $3.17U_p$, the single-atom cutoff energy is:

$$w_{cutoff} = I_p + 3.17U_p = I_p + 9.33\times10^{-14} \times I \times \lambda^2 \qquad (2.8)$$

Here w_{cutoff} and I_p are in unit of eV, I is the intensity of driving laser field in unit of W/cm², λ is the wavelength of the driving laser field in unit of μm.

From equation 2.8, it is clear that there are three ways to increase HHG cutoff. 1. HHG cutoff can be increased by increasing the ionization potential of gas, and this is well confirmed and realized experimentally. Experimentally, we can generate HHG with the highest photon energies from He, then Ne, then Ar, then Kr, then Xe. What's more, we can produce HHG with higher photon energies from ions than from atoms. The higher is the ion charge, the higher cutoff we can generate since the ionization potential is higher [93]. 2. HHG cutoff can be increased by increasing the intensity of the driving laser field. However, when the laser intensity is too high, the medium can be over ionized that too much dispersion is introduced that the process cannot be phase matched as will be discussed in details in section 2.3. HHG with higher photon energies can be produced, by using lasers with shorter pulse duration to limit the amount of ionization [70, 94]. 3. HHG cutoff can be effectively increased, by using driving lasers with longer wavelength, which is well confirmed and developed experimentally [7, 26-28]. This method can dramatically increase the cutoff while using relatively low intensity, so good phase matching can be guaranteed to generate bright HHG beams. Equation 2.8 gives the singe-atom cutoff, experimentally the process needs to be phase matched to generate bright beams. Phase matching is possible only for ionization levels below the critical ionization rate as will be discussed in the section 2.3, so experimentally, the phase matching cutoff is always smaller than the single-atom cutoff.

In the picture of the three-step model, HHG is only one of the strong-field nonlinear phenomena. Other important processes are high-energy above threshold ionization (HATI) [95, 96] and nonsequential double ionization (NSDI) [97, 98]. Recombination of the returning electron with its parent ion leads to harmonic emission. When the returning electron elastically scattered off its parent ion in the backward direction, the kinetic energy spectrum of the ionized electrons shows a characteristic plateau of electron peaks, separated by one fundamental photon energy, with a sharp drop around $2U_p$ and a cutoff of $10U_p$, this phenomena is knows as HATI. When the returning electron inelastically collides with its parent ion, another electron can be ionized so that the atom is doubly ionized. This process is called NSDI, in which a knee is observed in the photoelectron intensity dependence at the point where the single ionization saturates, indicating that the two processes are coupled.

This classical mechanical propagation model, treating the free electron as a particle, provides much insight into the physical process and many properties of the produced harmonic radiation. In the temporal domain, ionization happens every half optical cycle around the peak of the field, and there are many electron trajectories for each ionization group corresponding to ionization at different phases, harmonic emissions by recombination of these electrons form a harmonic burst. So a train of harmonic bursts with a period of half the optical cycle is produced. The Fourier transform of such a pulse train in the time domain gives odd harmonic orders of the fundamental frequency in the spectral domain. And since there are returning electrons with different kinetic energies, leading to harmonic emission up to the cutoff are generated with approximately equal probability, corresponding to the plateau region of the harmonic spectrum, which is in sharp contrast to the case of low-order harmonics in the perturbative regime, where the single-atom intensity of harmonic falls off exponentially with harmonic order [78].

However, the three-step model does not consider the quantum wave nature of the electron. In the quantum picture, the wavefunction of the electron is initially confined in a bound state due to the potential of the nucleus. Once part of the wavefunction tunnels into free space, the well-confined wavefunction begins spread out spatially. So the classical picture misses some of the physics that is important to the scaling of harmonic yield with the driving laser wavelength. When the electron's wavepacket travels back to its parent ion, the recombination probability is determined by the overlap of the returning electron wavefunction with the wavefunction of the electron in the bound state of the ion. The electron wavefunction spreading is proportional to the time that the electron spends in the continuum in all three spatial dimensions, which is longer when the wavelength of the driving laser field is longer, so there is a λ^{-3} scaling of the single-atom harmonic yield due to the free electron's wavefunction spreading. On the other hand, since the cutoff is scaled as λ^{2}, assuming the total single-atom yield from fundamental light to harmonic light is approximately constant, then the harmonic intensity is distributed over a broader range when longer-wavelength-driving beams are used, so the conversion efficiency into a single harmonic is reduced by another factor of λ^{-2}. This end up with an unfavorable single-atom efficiency scaling as λ^{-5} for a single harmonic order when using driving beams with longer wavelength. Detailed quantum mechanical calculations and experimental results have shown that the single-atom yield of a single harmonic order is scaled as $\lambda^{-5.5}$ to $\lambda^{-6.5}$ [82-84, 99, 100]. Fortunately it turns out that when HHG is driving by lasers with longer wavelength, higher gas pressure is needed to phase match the generation process, compensating the decreased single-atom harmonic yield [27]. In the next section, the collective response of the gas medium, i.e. the phase matching of HHG, will be discussed.

2.3 Macroscopic effect of high harmonic generation

In the last section, physical picture of HHG from single-atom view is discussed. Experimentally, HHG process involves collective behavior of tons of atoms. In this section, macroscopic picture of HHG will be discussed, including phase matching, critical ionization rate, and gas reabsorption.

2.3.1 Phase matching

Harmonic emission from a single atom is super small, however if the emitted light from tons of atoms add up constructively, i.e. the emitted light from tons of atoms are phase-matched, bright HHG beams can be generated. When the driving laser travels with the same phase velocity as the emitted harmonics, the newly emitted harmonics will travel with the same phase with earlier emitted harmonics, allowing constructive add up. So phase matching of HHG is to ensure the same travel velocity of the driving laser pulse and the harmonic beam. The phase mismatch between the driving laser pulse and the qth order harmonic is $\Delta k = qk_0 - k_q$. In this thesis, I generate harmonics in a hollow core waveguide for the advantages of maintaining a high laser intensity over a long distance, maintaining very high gas pressure, and allowing a better harmonic beam profile by cleaning up the driving laser beam profile.

In the waveguide geometry the phase mismatch mainly comes from three factors: the waveguide geometry, neutral atoms dispersion, and plasma dispersion [5, 101]. The intrinsic-phase introduced phase mismatch is negligible in this geometry since the driving laser light propagates as a plane wave in the waveguide with a uniform intensity distribution [28]. The total phase mismatch in the fiber geometry is:

$$\Delta k = -\frac{q\mu_{11}^{2}\lambda}{4\pi a^{2}} + P\left[\frac{2\pi(1-\eta)q}{\lambda}\Delta n\right] - P[\eta(q-\frac{1}{q})N_{1atm}r_{e}\lambda] \qquad (2.9)$$

Here, q is the harmonic order, $u_{11} = 2.405$ is the 1st root of the Bessel function $J_0(u_{11}) = 0$, a is the inner radium of the hollow core waveguide, P is the gas pressure, η is the ionization fraction discussed in the last section, λ is the wavelength of the driving laser beam, $\Delta n = n_{1atm}(\lambda) - 1$, $n_{1atm}(\lambda)$ is the index of fraction of the driving laser beam in one atmosphere of the gas medium, N_{1atm} is a constant of the gas density at one atmosphere, $r_e = \frac{1}{4\pi\varepsilon_0}\frac{e^2}{m_e c^2} = 2.818 \times 10^{-15}$ [m] is the classical electron radius. When $q \gg 1$, $q - \frac{1}{q} = q\left(1 - \frac{1}{q^2}\right) \approx q$, so the phase mismatch equation can be rewrote as:

$$\Delta k = q\left\{-\frac{\mu_{11}^{2}\lambda}{4\pi a^{2}} + P\left[\frac{2\pi(1-\eta)}{\lambda}\Delta n\right] - P\eta N_{1atm}r_{e}\lambda\right\} \qquad (2.10)$$

When $\Delta k = 0$, the process is fully phase matched. In equation 2.10, the first item is the waveguide geometry term and it is negative, which means in the waveguide the driving laser beam travels with a velocity bigger than the speed of light. The second term is the neutral atom dispersion term and it is positive, which means in neutral atoms the driving laser beam travels with a velocity smaller than the speed of light. The third term is the plasma dispersion term and it is negative, which means in plasma the driving laser beam travels with a velocity bigger than the speed of light. The second and third terms are proportional to the gas pressure with opposite signs, so experimentally we can tune the gas pressure to make $\Delta k = 0$. Since the first item is negative, the sum of the second and third term needs to be positive to achieve full phase matching. When the sum of the second and third term is negative, the driving laser field and the harmonic fields can never be phase-matched, making harmonic output weaker.

2.3.2 Critical ionization level

From equation 2.10 we can see once the ionization fraction becomes bigger than a certain ionization level η_c, know as the critical ionization level, the sum of the second and third term changes sign from positive to negative. When the ionization level is higher than η_c, it is not possible to compensate the geometry term and the process can't be phase-matched. By setting the sum of the second term and third term in equation 2.10 to zero we get the critical ionization level to be:

$$\eta_c = \left(1 + \frac{N_{1atm} r_e \lambda^2}{2\pi \Delta n}\right)^{-1} \propto \frac{\Delta n}{\lambda^2} \qquad (2.11)$$

From equation 2.11 and Fig. 2.5, we see that the critical ionization level depends on the driving-laser wavelength and the refractive index of the driving beam in the gas target. The critical ionization rate is smaller when the wavelength of the driving beam is longer and when the refractive index of the driving beam in the gas is smaller [27].

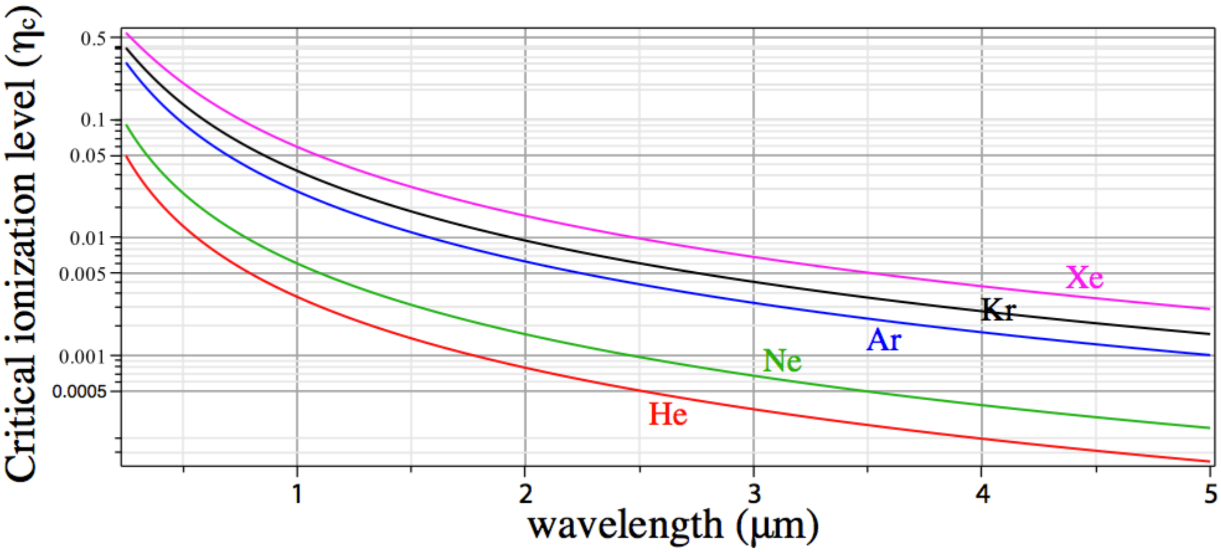

Figure 2.5: Critical ionization level of Xe, Kr, Ar, Ne, and He as a function of driving-laser wavelength. This figure is captured from [102].

2.3.3 Gas reabsorption

Harmonics are generated as the driving laser beam propagates through the gas medium in the z direction, with phase matching conditions fullfilled, earlier generated harmonics are added to newly generated ones coherently, which means the generated harmonics will be brighter if the gas medium is longer. However, the gas mediums are not transparent to the harmonics, the gas medium not only emits harmonics, but also reabsorbs them. Reabsorption limits the brightness of phase-matched HHG. Fig. 2.6 is captured from Ref. [9], in this figure $L_{coh} = \pi/\Delta k$ is the coherence length (Δk is the phase mismatch discussed earlier in this section). $L_{abs} = 1/\rho\sigma$ is the absorption length, i.e. the length over which the intensity of the harmonic light propagating in the medium drops to $1/e$, here ρ is the gas density, σ

is the photoionization cross section. Even when the coherence length is infinite, the harmonic emission saturates as soon as the medium length is longer than a few L_{abs}, since harmonics emitted beyond that are reabsorbed. As the coherence length decreases, the efficiency saturates at smaller values. For $L_{coh} < L_{abs}$, the efficiency is more than 10 times smaller than the asymptotic value corresponding to infinite coherence length [9]. In Ref. [9], the authors present the optimizing conditions are:

$$L_{med} > 3L_{abs} \; and \; L_{coh} > 5L_{abs}$$

Here L_{med} is the gas medium length. This condition ensures half of the maximum output corresponding to the asymptotic value when $L_{coh} \gg L_{abs}$.

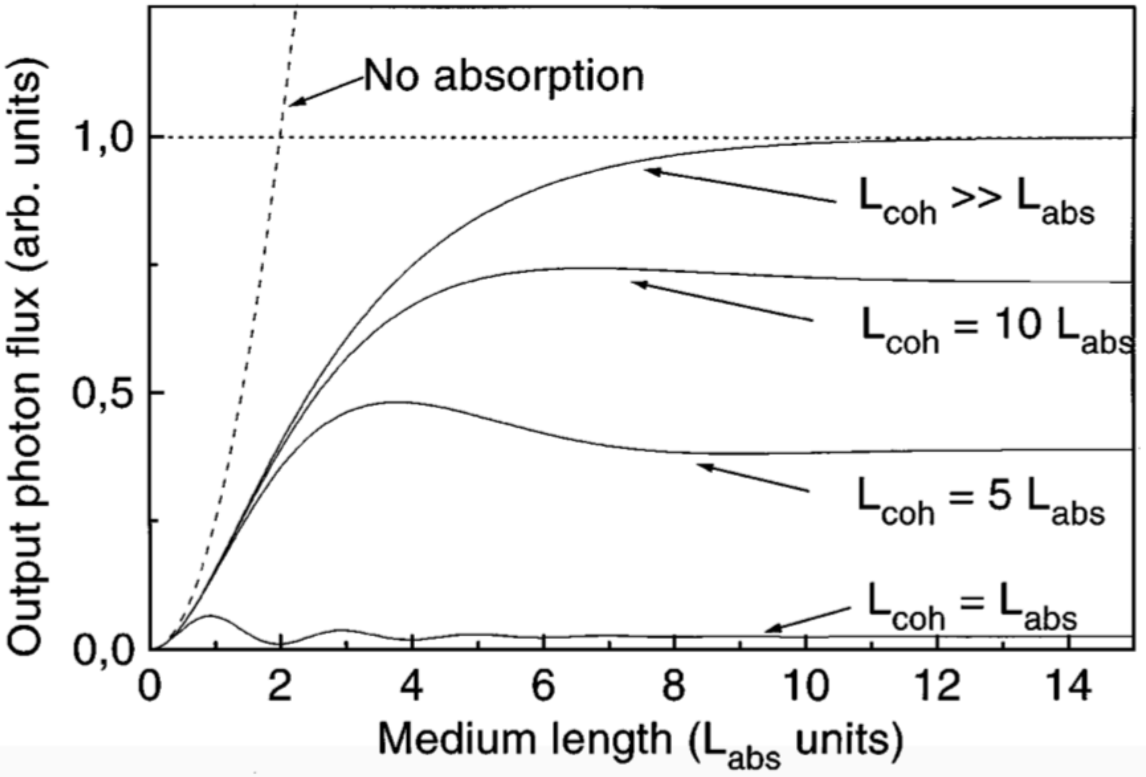

Figure 2.6: On-axis flux of HHG (arbitrary units) as a function of the medium length (in units of absorption length). The dotted line corresponds to a zero absorption case. This figure is captured from [9].

In summary, HHG is a collective response of tons of atoms. While the ultrafast laser pulse propagates through the gas medium, the gas atoms are ionized, introducing phase mismatch between the driving laser beam and the generated harmonic beam. When the ionization fraction is below the critical ionization level, the phase mismatch can be compensated, by tuning gas pressure such that HHG is fully phase matched. Phase matching enables bright harmonic emission, however the brightness was limited to a maximum value by gas reabsorption of emitted harmonics.

2.4 Experiments and results

Most implementations of HHG used Ti:sapphire driving lasers at a wavelength around ~0.8 μm. In this case, phase matching considerations limit bright HHG to photon energies ≤100 eV, which lie in the EUV spectral region. This limits applications of HHG to very thin samples and a relatively small number of elements that have absorption edges in the EUV region. Other work extended HHG into the soft X-ray region using short 12-fs laser pulses in a non-phase matched implementation, with a flux of 10^5 photons/s in 1% bandwidth [103]. As discussed in the last section, by using laser beams with longer wavelength, the cutoff energy of high harmonics can be effectively increased. However, because of the unfavorable single-atom yield when the wavelength of the driving beam is longer, early experiments only generated un-phase-matched harmonics at low flux [104, 105].

In 2008, T. Popmintchev et al. demonstrated that phase matching can be obtained at higher gas pressures when using a longer-wavelength-driving laser, mitigating the unfavorable scaling of the single-atom response and theoretically predicted that phase-matched high harmonic frequency upconversion driven by mid-IR pulses could be extended to extremely high photon energies [26]. This concept was further demonstrated by experimentally reaching a 330 eV cutoff when driving with a 1.3-μm laser system [27], a 520 eV cutoff when driving with a 2-μm laser system [28], and a 1.6 keV cutoff when driving with a 3.9-μm laser system [7]. However, these preliminary studies were done using lasers operating at tens of Hz repetition rates, generating harmonics with a total photon flux of 10^6 photons per second in 1% bandwidth [28], which is insufficient for broad applications in spectroscopy or imaging. To fully harness the unique properties of soft X-ray HHG, kHz or higher repetition-rates are required in a phase-matched geometry. This goal requires the development of stable, compact, high pulse-energy, ultrafast laser amplifiers that can generate multi-millijoule, few cycle, mid-IR laser pulses required for efficient HHG.

Note that since HHG is a highly-nonlinear process, it is very sensitive to fluctuations in peak laser intensity or beam pointing. Moreover, the efficiency of the HHG process scales rapidly with pulse energy, and requires mJ scale pulse energy to obtain absorption-limited conversion efficiency in the soft X-ray region [7, 26-28]. To obtain this pulse energy in a femtosecond mid-IR pulse, OPA [106] and optical parametric chirped-pulse amplification (OPCPA) [29] can be employed [7, 26-28, 30, 107, 108]. However, each approach has shortcomings for HHG. OPCPA systems are still experimental in this parameter range, and do not yet possess the stability, multi-mJ, kHz repetition rates, and reliability required for HHG application. Similarly, although Ti:sapphire laser pumped OPAs are a well-established technology, this approach requires a ~10-mJ pulse energy from the Ti:sapphire laser. The complexity of the traditional two-amplification-stage lasers required to pump an OPA greatly increases the cost and difficulty of implementing a tabletop HHG soft X-ray source reliably on a daily basis.

In our experiment, we demonstrate a single-stage, 10-mJ, ultrafast (45-fs) Ti:sapphire amplifier, with a repetition rate of 1 kHz. Then, I use this laser (with an output of 8.5 mJ to achieve the best output mode for pumping OPA, so optimal OPA output mode is achieved to pump HHG for the best HHG mode and conversion efficiency) to pump a three-stage OPA system. From the OPA, I generate a signal beam with a 1.3-μm wavelength, a 30-fs pulse duration, and sufficient energy (2.25 mJ) for optimally-efficient, phase-matched HHG conversion, as well as an idler beam with a 2-μm wavelength, a 35-fs pulse duration, and a 1.4-mJ pulse energy. As shown in Fig. 2.7, the signal beam is then focused into a hollow-core waveguide with a 1-cm length and a 150-μm inner diameter by a calcium fluoride lens with a 25-cm focal length.

After the fiber, the driving laser beam is blocked by thin-film filters, while most part of the HHG beam passes through the thin film filters, then goes through an X-ray spectrometer, finally its spectrum is recorded by an X-ray CCD. This geometry allows high flux, soft X-ray HHG source with a photon flux of > 10^6 photons/pulse/1% bandwidth at 1 kHz (corresponding to > 10^9 photons/s/1% bandwidth) in a broadband continuum spectrum extending to 200 eV. This photon flux represents an approximately three orders-of-magnitude increase compared with past work, which used lower repetition rates, or non-phase-matched implementations [27, 30]. And I will show in chapter 3 that using this unique bright supercontinuum soft X-ray HHG light source, XAS of multiple elements and transitions in molecules is demonstrated simultaneously, with 0.25 eV spectral resolution, and with the ability to resolve near edge fine structure with high fidelity.

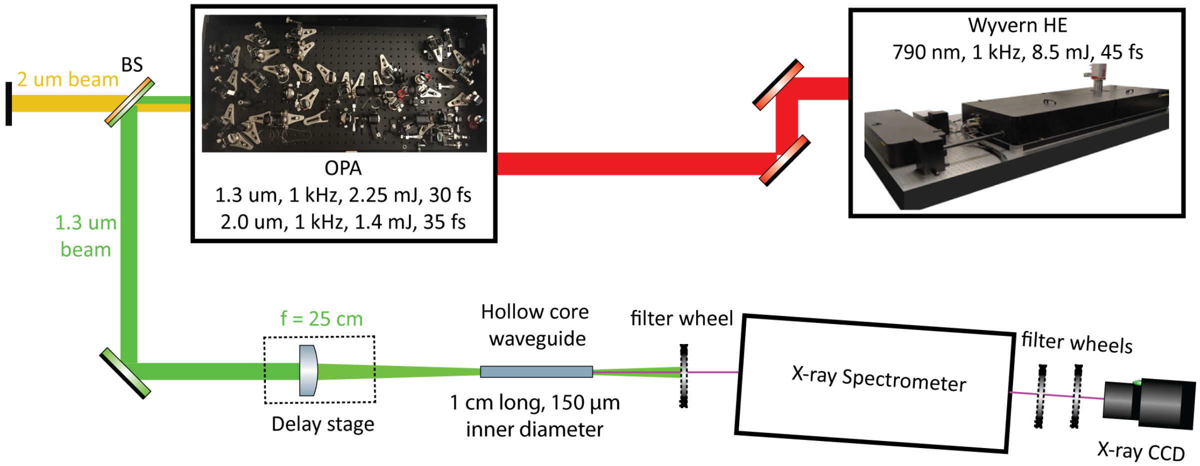

Figure 2.7: Schematic diagram of the experimental setup.

2.4.1 Single-stage 10-mJ femtosecond amplifier

I first discuss the 10-mJ, single-stage, 1-kHz regenerative Ti:sapphire amplifier system (KMLabs Wyvern HE™) and high-efficiency OPA that generates high quality 1.3-μm driving pulses for soft X-ray HHG. The maximum output pulse energy obtainable from an ultrafast Ti:sapphire regenerative amplifier is primarily limited by two factors: thermal lensing [109] and optical damage. At a specific crystal temperature and pump power, the mode area can be increased to decrease the amplified pulse peak intensity, thus reducing optical damage. The thermal lens is also reduced by increasing the mode area, since the focal length of the thermal lens is proportional to the mode area [110]. However, at room temperature, the focal length of the thermal lens is not tolerable (≈10 cm, at 300 K, at a pump power of 50 W at 532 nm, and mode radius of 500 μm). In order to achieve a thermal lens focal length of tens of meters (≈25 m, at 77 K, at a pump power of 50 W at 532 nm, and mode radius of 500 μm), which is require by the elongated cavity length, the crystal must be cryogenic cooled.

Therefore, to limit optical damage while not introducing a detectable thermal lens, three design ideas were combined. First, optical damage was limited by increasing the cavity length (mode area) and also ensuring that the seed pulse was stretched to 150 ps using high groove density gratings (1800 lines/mm). As a result, the amplified pulse fluence of 1.0 J/cm^2 at 150 ps is below the damage threshold of commercial broadband optics (typically ≈1.5 J/cm^2 at 150 ps). Second, by employing closed-cycle cryogenic cooling of the Ti:sapphire crystal, the temperature of the Ti:sapphire crystal can be maintained below 70 K, even when pumped with 50 W of 532-nm light. This dramatically (i.e. by >>100x) reduces the thermal lens present in the laser crystal [111], and ensures the thermal lens not detectable even using a longer cavity. The maximum output (compressed) pulse energy is 10.6 mJ when pumped with 50 mJ of 527-nm light from a Nd:YLF pump laser. Since the efficiency of the diffraction grating based compressor is 70%, this represents an optical-to-optical efficiency of the regenerative amplifier of ~30% before compression. To our knowledge, this represents at least a 25% improvement in the pulse energy obtainable from a single-stage 1-kHz Ti:sapphire amplifier [112]. This increased pulse energy is critical since the OPA and HHG processes are non-linear: therefore the conversion efficiency into the mid-IR and then to soft X-rays increases dramatically with increasing energy of the Ti:sapphire driving pulse.

The OPA and HHG processes are also extremely sensitive to the beam mode and the pulse duration. The 10-mJ single-stage regenerative Ti:sapphire amplifier has a nearly perfect Gaussian mode output as shown in Fig. 2.8, with M square values for both x-axis and y-axis of ~1.1, which means almost all the pulse energy is in the lowest-order Gaussian mode. This feature ensures good conversion efficiency and output mode for the OPA, which in turn ensures high HHG efficiency (since a good OPA mode efficiently couples into a waveguide and facilitates good phase matching). The pulse duration after the compressor is ≤ 45 fs, and is primarily limited by the bandwidth of the thin film polarizer (TFP) inside the amplifier cavity. Unlike a conventional regenerative cavity, the dispersion introduced by the material in the regenerative cavity is not the limiting factor for the pulse duration because only 12 passes through the Ti:sapphire crystal are needed to reach the full output power (15 mJ before compression), which is approximately the same number of passes used in a typical multipass Ti:sapphire amplifier, but with much higher efficiency. In contrast, a typical regenerative amplifier requires 20-40 passes. In the future, a shorter pulse can be achieved when broader bandwidth, higher-damage-threshold TFPs become available.

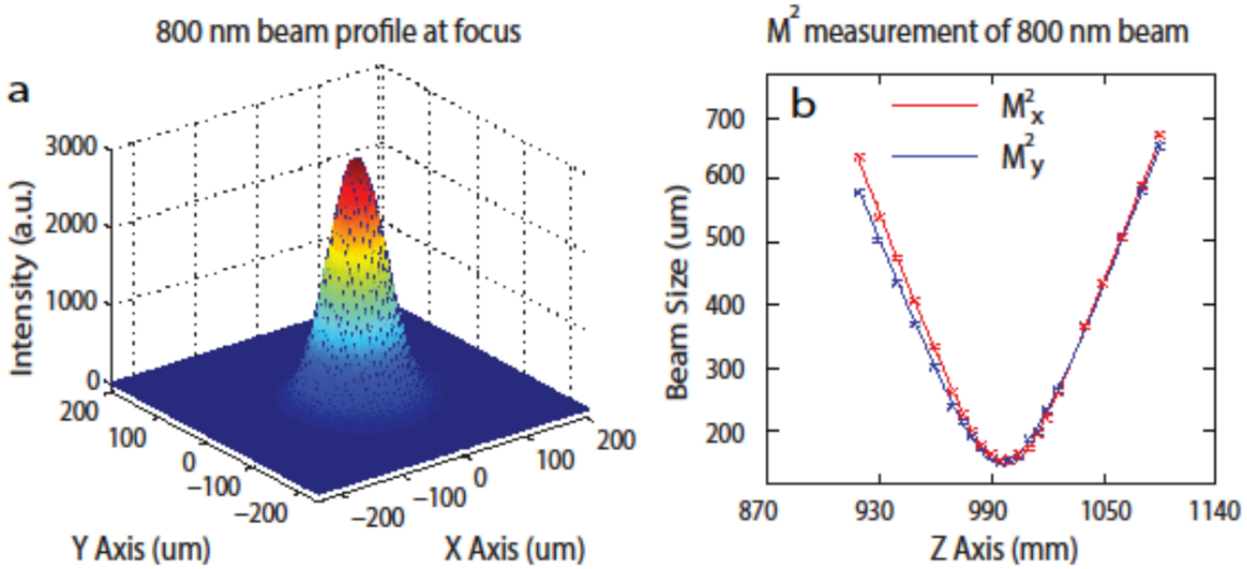

Figure 2.8: (a) Output beam profile of the single-stage Ti:sapphire regenerative amplifier (KMLabs Wyvern HE™) when it is focused by a 1-m focal length lens. (b) M square of the amplifier output was measured to be ~1.1 for both x-axis and y-axis. Data taken at 10 mJ, 1 kHz.

2.4.2 Home-built three-stage optical parametric amplifier

To obtain high-quality 1.3-μm pulses to drive soft X-ray HHG, we use a homebuilt three-stage OPA that achieves greater than 40% conversion of the 0.79-μm light into 1.3-μm (signal) and 2-μm (idler) beams as shown in Fig. 2.9. Type II BBO crystals are used as the nonlinear crystals in the OPA to amplify the seed from the white light generation process for the reasons that type II phase matching enables a much longer phase matching distance for higher conversion efficiency, and type II phase matching allows a much broader tunability of the output wavelength. Crystal thicknesses of 2.5 mm, 2.0 mm and 1.5 mm were used in the first, second, and third OPA stage respectively. The high energy OPA design is the standard one used by many groups worldwide, similar for example to the HE-TOPAS from Light Conversion. Due to the excellent beam quality of the high-energy regenerative amplifier, very high conversion efficiency of 43% is possible in the OPA.

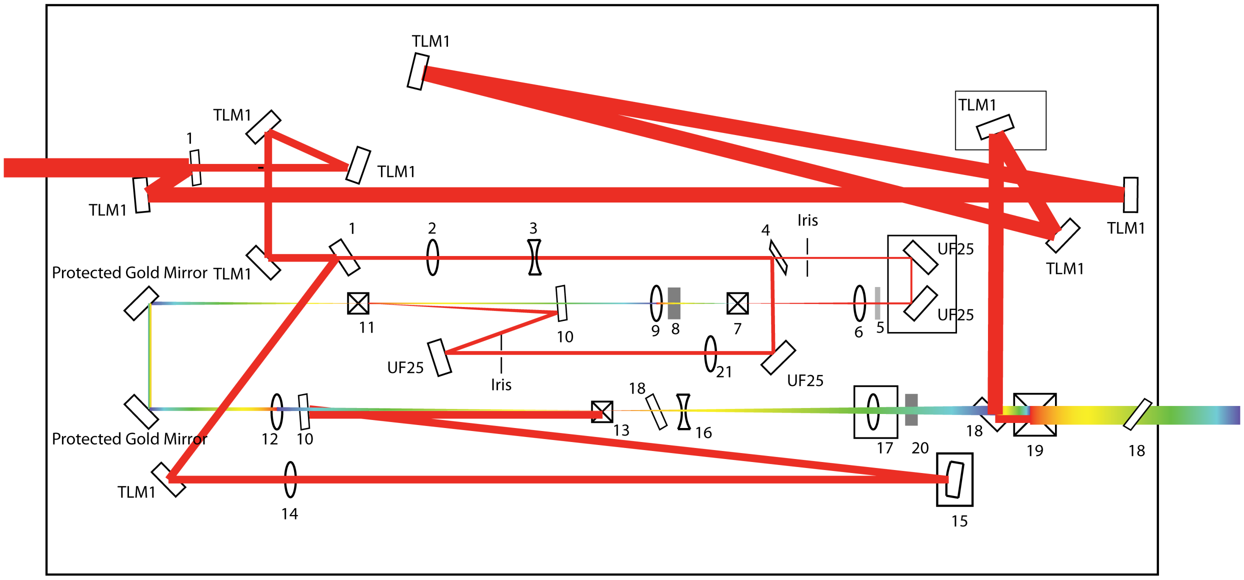

1. Beamsplitter, R: 90%, T: 10% 2. f = 200 mm, AR @ 800 nm 3. f = -125 mm, AR @ 800 nm 4. Beamsplitter, R: 80%, T: 20% 5. 800 nm half waveplate
6. f = 100 mm, AR @ 800 nm 7. YAG crystal 8. ZnSe crystal to chirp the whitelight 9. f = 50 mm, AR @ 800 nm 10. Dichroism mirrors HR @ 720-840 nm, AR @ 1.1-2.6 um, 0 degrees angle of incidence 11. BBO crystal: 5 x 5 x 2.5 mm, type2, theta = 28 deg, phi = 0 deg P/P @ 800--2080 nm 12. f = 300 mm IR coating
13. BBO crystal: 8 x 8 x 2 mm, type2, theta = 28 deg, phi = 0 deg P/P @ 800--2080 nm 14. f = 2 m 15. f = 500 mm, convex 16. f = -25 mm IR coating
17. f = 75 mm IR coating 18. HR @ 720-840 nm, AR @ 1.1-2.6 um, 45 degree angle of incidence 19. BBO crystal 12 x 12 x 1.5 mm type 2, theta = 28 deg, phi =0 deg, p/p @ 800--2080 nm 20. MgF2 birefrigent crystal – separate signal and idler in time
TLM1 and UF25 are dielectric mirrors high reflection at 800 nm

Figure 2.9: Schematic diagram of the high-energy three-stage OPA.

For these measurements, the total pulse energy used to drive the OPA was 8.5 mJ. In the first stage, 1% of the pulse energy is used for white light generation and the first stage pump. The second stage uses 9% of the pulse energy as the pre-amplification pump, while 90% of the pulse energy is used to pump the third stage. The output OPA signal pulse energy is 2.25 mJ, with a spectral full-width of greater than 200 nm centered at 1.3 μm. The pulse energy of the idler beam is 1.4 mJ, giving a total conversion efficiency from the pump to the signal plus idler of approximately 43%. The good coupling efficiency of the OPA mode into the waveguide and the resultant recorded soft x-ray flux (as discussed in the following section) demonstrates that the OPA mode is of high quality, and indeed was the motivation for the new regenerative amplifier design. Additionally, the broad spectrum of the 1.3-μm light originates from white light generation, and supports an ultrashort pulse duration of 30 fs (characterized by a second harmonic FROG measurement as shown in Fig. 2.10). As expected in parametric down conversion of multi-cycle ultrafast pulses, this signal pulse duration is considerably shorter than the 45-fs 0.79-μm pump pulse.

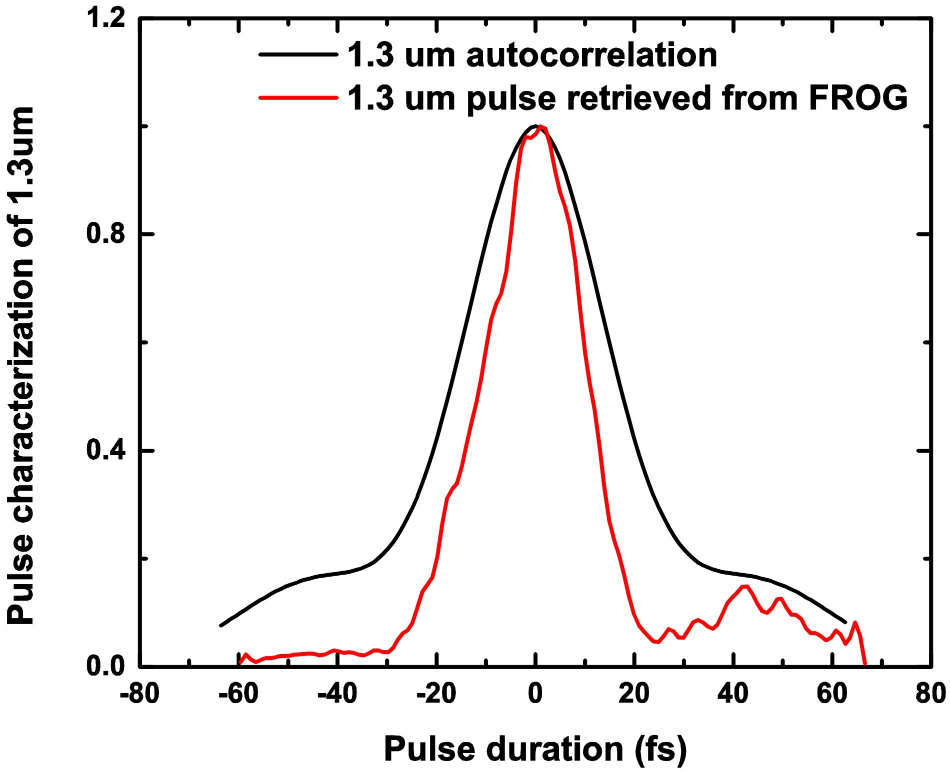

Figure 2.10: Pulse duration of the 1.3-μm beam from OPA was measured to be 29.6 fs by SHG FROG, which is shorter than the pulse duration of the pump beam because OPA is a non-linear process, and the signal beam is generated at the most intense part of the pump beam.

2.4.3 High flux soft X-ray high harmonics

Bright soft X-ray high harmonics are generated by focusing the 2.25-mJ 1.3-μm OPA signal beam into a gas-filled hollow-core waveguide (1-cm length and 150-μm inner diameter) using a 25-cm focal length lens. The coupling efficiency is more than 50% even with high gas pressure in the waveguide, so that the driving pulse peak intensity inside of the waveguide can reach 5 × 10^{14} W/cm^2, with the energy well coupled into the EH_{11} mode. The waveguide geometry is essential for achieving fully phase-matched high flux soft X-ray harmonics for two reasons. First, use of a guided mode ensures nearly plane-wave propagation of the mid-IR driving beam, to maintain a flat uniform phase and high peak intensity over a long interaction distance. And second, the waveguide confines the gas, allowing high gas pressures (>1 atm) to be used, which is critical for achieving absorption-limited phase-matched HHG flux for longer-wavelength driving beams. This high-pressure gas medium, together with an abrupt transition to vacuum out of the interaction region, become increasingly important as the HHG driving laser wavelength is increased, because the phase matching pressure (multiple atmospheres) is higher than for 0.79 μm driven HHG. Moreover, since the single-atom HHG yield drops, more emitters are needed to obtain high flux harmonics.

To generate bright soft X-rays, the waveguide is filled with Ar or Ne. Since each noble gas has a different refractive index and ionization potential, each gas optimizes at different phase matching pressures and laser intensities, and also extends efficient HHG to some maximum phase-matched photon energy cutoff. By controlling the gas pressure inside the waveguide and the 1.3-μm pulse energy before the waveguide, we can optimize the HHG flux at the phase matching pressure as shown in Fig. 2.11. For a 1-cm long, 150-μm inner diameter waveguide and 1.3-μm driving lasers, the optimized pulse energies, phase matching pressures and phase matching cutoff photon energies are 0.95 mJ, 700 Torr and 110 eV for Ar, and 1.6 mJ, 1300 Torr, and 200 eV for Ne. By accounting for the absorption of the metal filters, the efficiencies of the spectrometer (Hettrick Scientific), and the quantum efficiency of the CCD camera (Andor, Inc.), the photon flux of the harmonics is estimated to be more than 10^6 photons/pulse in 1% bandwidth up to 200 eV (Fig. 2.11), corresponding to 10^9 photons/s in 1% bandwidth at kHz repetition rates. This photon flux represents an approximately three orders-of-magnitude increase compared with past work (which used lower repetition rates or non-phase matching geometry) [27, 30]. Additionally, a long-term stability test demonstrates that the HHG flux is stable over many hours, limited primarily by beam pointing drift (when no beam-pointing stabilization is used).

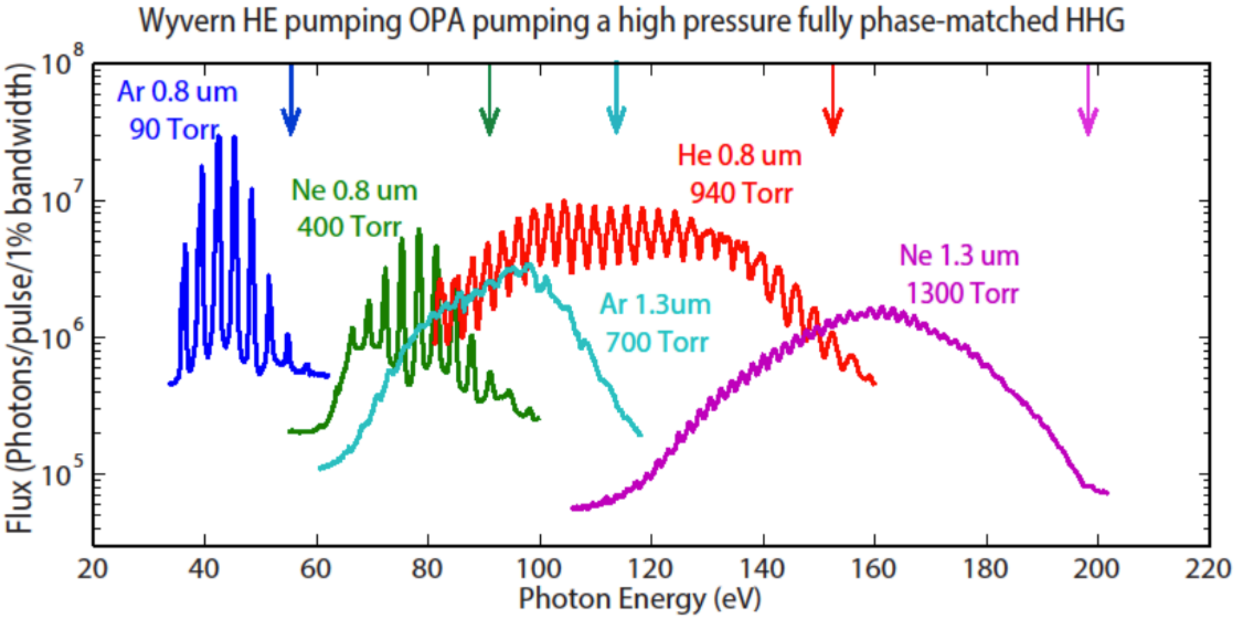

Figure 2.11: Flux of the experimentally-optimized fully-phase-matched HHG emission from a 1-cm long, 150-μm inner diameter waveguide driven by laser beam with wavelengths of 1.3 μm and 0.8 μm in various noble gases (Ar, Ne, and He). The vertical arrows indicate the maximum predicted phase-matched HHG cutoff for each gas and laser wavelength. The HHG flux obtained using a driving laser with a wavelength of 1.3 μm is comparable to that achieved using 0.8 μm.

Since numerous experiments have been implemented utilizing 0.8-μm-driven EUV harmonics, we compared the optimized fully-phase-matched HHG flux driven by 0.8-μm light with the HHG flux driven by 1.3-μm light. We used the same waveguide for comparison, since the geometry and quality of the waveguide might affect the harmonic yield. The pulse energy used for the 0.8-μm-driven HHG from Ar, Ne, and He is 0.40 mJ, 1.5 mJ and 2.2 mJ, respectively. We find that at 100-eV photon energy, the 1.3-μm-driven HHG flux is within a factor of two of the 0.8-μm-driven HHG flux, while above 150 eV, the 1.3-μm HHG flux becomes much more efficient. This suggests that many applications based on EUV harmonics can now be extended to the soft X-ray region. Although our laser/OPA system did not provide sufficient pulse energy to generate fully optimized phase-matched HHG flux from He, we were in-fact able to generate coherent light up to ~300 eV from He (as shown in Fig. 3.5(a)). However, the HHG flux obtained was significantly lower (by ~100x) than the data of Fig. 2.11, which still represents a record HHG flux of 10^7 photons/s in 1% bandwidth at 300 eV, at kHz repetition rates. We predict that a further modest increase in pulse energy (by ≤ 2x) will allow us to generate flux comparable to that of Fig. 2.11 up to the water window using He as the nonlinear medium.

2.5 Summary

In summary, in this chapter I first introduced the background of HHG. Then the single-atom and macroscopic physics of HHG were discussed. Finally, I demonstrated a unique single-stage, 10-mJ, 1-kHz, Ti-Sapphire regenerative amplifier design capable of generating high-flux coherent soft X-rays using a two-step frequency upconversion process. Simplifying the driving laser into a single-stage laser greatly enhanced the stability and mode quality of the pump, which facilitates its application for an OPA-driven HHG setup. The 1.3-μm light generated from OPA is coupled into a high-pressure gas-filled waveguide to generate the soft X-ray HHG beams. By properly controlling the gas pressure and pulse intensity to fully phase match the HHG process, we achieve a photon flux of more than 10^9 photons/s/1% bandwidth up to 200 eV at kHz repetition rates, which is enhanced by > 10^3 compared with past work. The high-flux, broadband HHG spectra provide a unique opportunity to measure soft X-ray absorption spectra from multiple orbitals of an element or multiple elements simultaneously. Additionally, the kHz repetition rate ensures high quality absorption spectra in a short data acquisition time, which is important for time-resolved experiments. In the next chapter, I will discuss XAS using this soft X-ray HHG light source.

Finally I would like to mention recent advances in this field. Phase-matched carrier-envelop-phase (CEP) controlled Soft X-ray supercontinua, with pulse energies up to 2.9±0.1 pJ and a flux of $(7.3\pm0.1)10^7$ photons per second, across the entire water window (with coverage from 200 eV across the entire water window up to the oxygen K-shell edge at 543 eV), was demonstrated last year by using 400-μJ, 1.9-cycle (12-fs) CEP stable pulses at 1.85-μm wavelength at a repetition rate of 1 kHz [113]. This light source supports 13-as transform-limited attosecond pulses. And with this light source, NEXAFS at the carbon K-edge of a polyimide film was measured and the fine-structure peaks of the carbon binding orbitals were identified [114].

Chapter 3

X-ray absorption fine structure using soft X-ray high harmonics

In this chapter, I will talk about XAS using soft X-ray LPHHG. I will first discuss the background of this technique. Then I will show the experimental setup and static NEXAFS results in gas, solid, and liquid phase. And the measurement of transient EUV absorption spectroscopy of Xe will be presented. Finally I will summarize the content of the chapter.

3.1 Introduction

XAS is a widely used technique for determining the local geometric and/or electronic structure of matter. XAS measures the absorption of X-rays as a function of the incident X-ray photon energy [57]. And XAS data is obtained by measuring the transmission of the sample when X-ray beam with photon energy in a range where core electrons of the sample can be excited incidents on the sample. As shown in Fig. 3.1(a), if X-rays of intensity I_0 are incident on a sample, the extent of absorption depends on the X-ray photon energy E and the sample thickness t. According to Beer's Law, the transmitted intensity I_t is:

$$I_t(t) = I_0 e^{-\mu(E)t} \qquad (3.1)$$

Here μ(E) is the energy-dependent X-ray absorption coefficient, as shown in Fig 3.1(b) is a typical spectrum of μ(E). The samples can be in gas-phase, solution, or solids. XAS experiments were usually performed using synchrotron radiation sources [116] and free electron laser sources [117-120], which provide intense and tunable X-ray beams. Thanks to the rapid development of HHG light source [7, 27, 28, 30, 108, 113-115], more and more experiments are performed using HHG [114, 115].

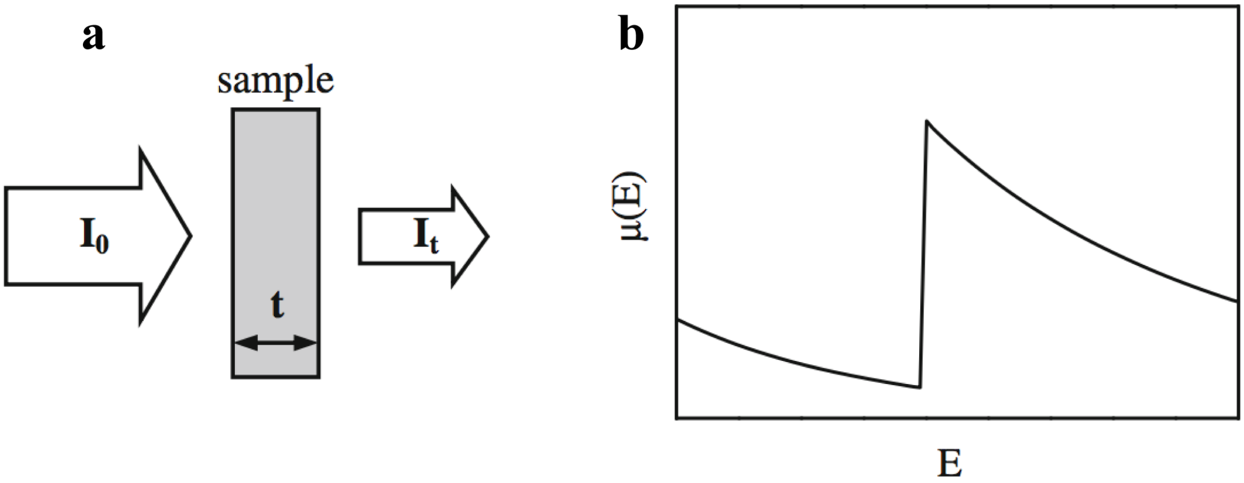

Figure 3.1: (a) Schematic of incident and transmitted X-ray beam for XAS. (b) Typical spectrum of XAS, absorption coefficient μ(E) versus photon energy E around an absorption edge. This figure is captured from [121].

A typical XAS spectrum shows three general features [57, 122]: 1. An overall decrease in X-ray absorption with increasing photon energy (Fig. 3.2(b)). This feature is a well-known phenomenon of X-ray absorption by atoms, X-rays with higher photon energy has a higher transmission through materials [123]. 2. The presence of saw-tooth-like features with a sharp rise at discrete energies, called absorption edges (Fig. 3.2(b)). The energy positions of these features are unique to a given absorbing atom. They occur near the ionization energy of inner shell electrons and contain spectral features due to core-to-unoccupied valence orbital transitions and core-to-continuum transitions. The "name" of the edge depends upon which core electron is excited: the principal quantum numbers n = 1, 2, and 3, correspond to the K-, L-, and M-edges, respectively. For instance, excitation of a 1s electron occurs at the K-edge, while excitation of a 2s or 2p electron occurs at an L-edge (2s at L_1, $2p_{1/2}$ at L_2, and $2p_{3/1}$ at L_3) (Fig. 3.2(a)) [124]. 3. X-ray absorption fine structures that can be divided into two parts as shown in Fig. 3.3(a). NEXAFS, also know as X-ray absorption near edge structure (XANES), is the low-energy part just below, at, and just above the edge. It is usually around the absorption edge up to 20-50 eV above the edge. This region includes bound-bound and bound-continuum (e.g. shape resonance) transitions, as well as multiple-scattering processes. The other part at energies significantly (tens to hundreds of electronvolts) above the edge is called extended X-ray absorption fine structure (EXAFS), which shows an oscillatory structure. In this region the scattering of the ejected photoelectron of neighboring atoms can be approximated by single-scattering events. Feature 3 carries lots of information about molecular and electronic structures that we are interested in, if a pump-probe experiment is implemented, a movie of molecular or electronic dynamics could be recorded by following the dynamics of the fine structures.

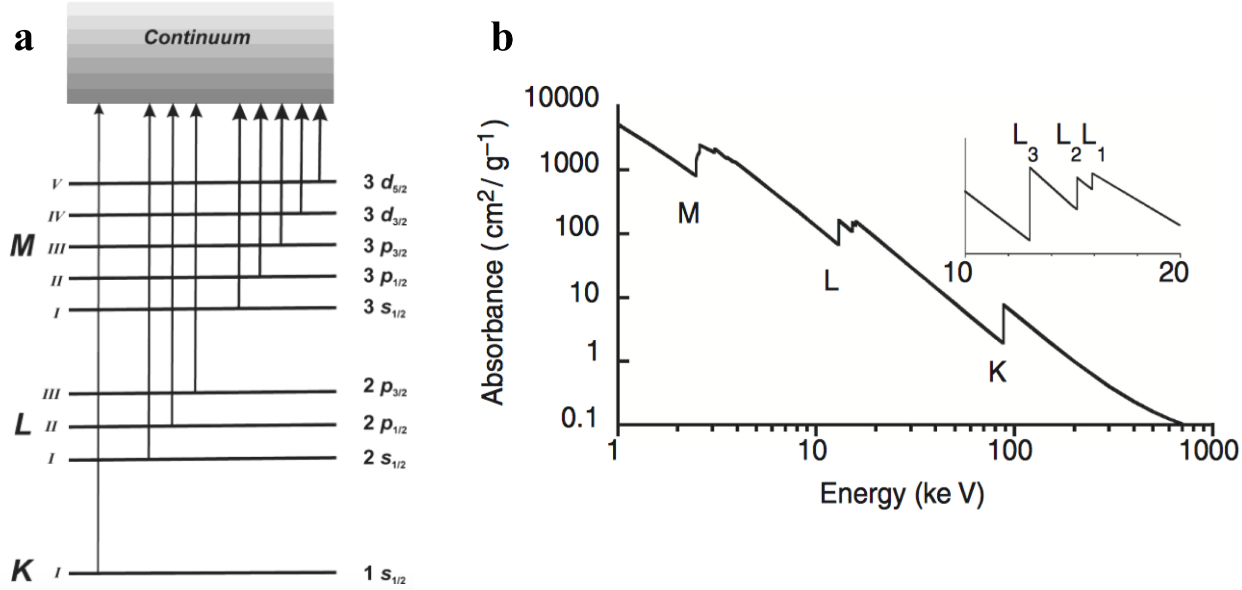

Figure 3.2: (a) Transitions resulting from the absorption of X-rays. The transitions are accompanied by the production of a photoelectron. This figure is captured from [57]. (b) Low-resolution X-ray absorption spectrum for Pb. Three major transitions are seen (K, L, and M edges), corresponding to excitation of an electron from n = 1, 2, and 3 shells, respectively. At higher resolution (inset) both the L and the M edges are split. This figure is captured from [125].

In the EXAFS regime, because of the high photoelectron kinetic energies, the only significant contributions to the final state wavefunction in the vicinity of the absorbing atom comes from paths in which the electron is scattered only once as shown in Fig. 3.3(b). The oscillatory structure is present due to the interference between the outgoing photoelectron wave and the wave single-scattered back at neighboring atoms. EXAFS contains information about coordination number, interatomic distances, as well as structural and thermal disorder around a particular atomic species. The fact that multiple-scattering events can be neglected allows the analysis of EXAFS data by a simple Fourier transformation, providing a powerful tool for structural analysis [122].

Different than EXAFS, which is mainly a structural technique, NEXAFS is very close to the absorption edge and is characterized by transitions of the photoelectron to unoccupied bound states. NEXAFS is therefore sensitive to the chemical bonding. What's more, NEXAFS contains transitions of the photoelectron to the continuum and such transitions lead to strong multiple scattering of the excited photoelectron as shown in Fig. 3.3(b). This is very different than EXAFS, which is dominated by single-scattering events. These multiple-scattering effects depend on the three-dimensional geometrical arrangements of the atoms in a local cluster around the X-ray absorbing atom. So NEXAFS contains information about both the electronic and molecular structure. Theoretical calculations of the fine structure in this region are complex and the accuracy of such simulations is still limited although significant progress has been made over recent years [126, 127]. Therefore, analysis typically compares the measured spectra to those of known standards and quantifies the ratios by which these standards are present in the sample using linear combination fitting [121].

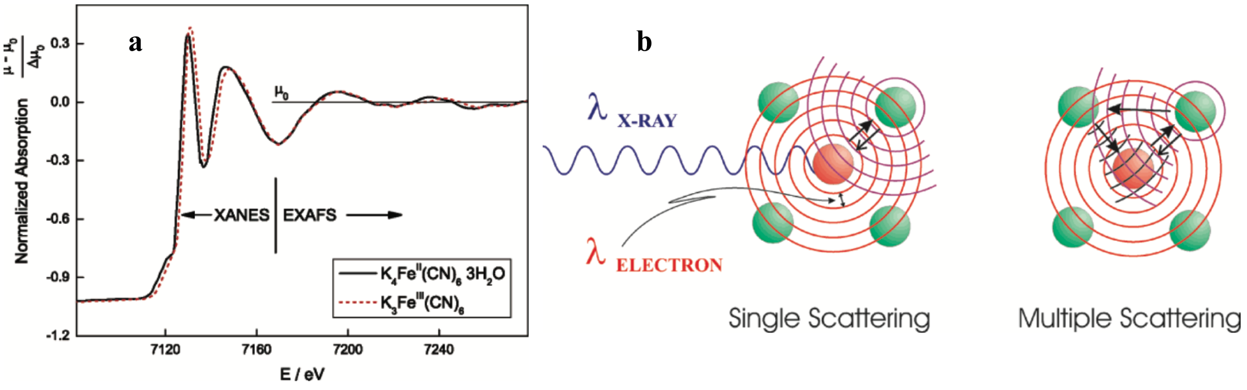

Figure 3.3: (a) K edge X-ray absorption spectra of iron in $K_4Fe^{II}(CN)_6$ and $K_3Fe^{III}(CN)_6$ bulk samples. The relative absorption with respect to the high-energy background is plotted. (b) Pattern of an outgoing and backscattered photoelectron wave in the case of EXAFS (single-scattering events) and NEXAFS (multiple-scattering events). This figure is captured from [57].

In our experment, we focus on measuring NEXAFS of gas, solid, and liquid samples by using the soft X-ray LPHHG. In the next sections of this chapter, I will present the experimental setup, sample geometries, and results. I will also present the measurement of EUV transient absorption dynamic of Xe. Finally, I would like to introduce the definition of the absorbance $A(E)$, which will be frequently used in the later sections of this chapter:

$$A(E) = -log_{10}(I_t(E)/I_0(E)) \qquad (3.2)$$

Where $I_0(E)$ is the X-ray intensity before or without the sample, $I_t(E)$ is the X-ray intensity transmitted through the sample.

3.2 Experimental setup

As shown in Fig. 3.4, the system starts from the single-stage Ti:sapphire amplifier running at a 8.5-mJ pulse energy, a 790-nm central wavelength, a 45-fs pulse duration, and a 1-kHz repetition rate with an excellent mode, which ensures the good conversion efficiency and output mode of the OPA, and thus the good coupling efficiency of the OPA output into the fiber and bright soft X-ray HHG emission. In pump-probe geometry, 15% of the output power of the amplifier transmits through a beamsplitter and is used as a pump beam. The other 85% of the output power is reflected into the three-stage OPA, with 43% conversion efficiency, generating a 1.88-mJ, 30-fs signal beam at 1.3 µm and a 1.22-mJ, 35-fs idler beam at 2 µm. The signal beam is then focused by a 25-cm focal length lens, into a 1-cm long, 150-µm inner diameter, hollow-core waveguide. The beam propagates from atmosphere to vacuum after passing through a 250-µm thickness CaF_2 window with Brewster angle. Nobel gases are filled into the waveguide through two gas inlets drilled by CO_2 laser and are efficiently pumped out from the entrance and exit of the fiber by differential roughing pumps. This geometry allows high gas pressure (1000 Torr) in the fiber between the two gas inlets, a sharp pressure drop after the gas inlets to tens of miliTorrs in the following connected tubes, and down to 10^{-4} Torr after the differential pumping block. This pressure distribution ensures good coupling efficiency around the entrance of the fiber and less reabsorption around the exit of the fiber.

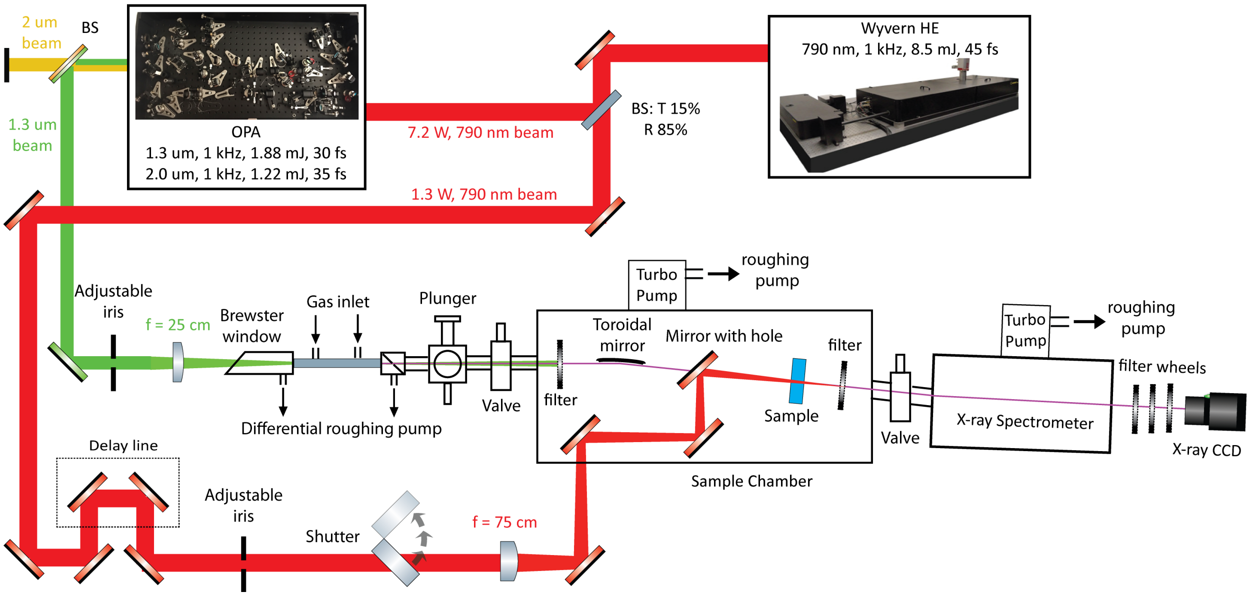

Figure 3.4: Schematic of the experimental system.

An iris is put before the lens to optimize phase matching and harmonic flux by controlling the input driving laser power. A plunger is mounted after the fiber, which provides easy transition between two phases in vacuum by pushing down or pulling up the handle. At one phase nothing is in the beam, allowing the free propagation of the beam. At the other phase a 45-degree mirror is inserted in the beam, directing the beam away from the setup to another direction for fiber-coupling mode and efficiency check purpose. A third phase can be added in the plunger where an iris with a very small opening is inserted in the beam, blocking most of the driving laser beam while letting HHG beam pass through, taking advantage of the supermall divergence of the HHG beam, to avoid burning of the filters and samples when a too-high driving laser intensity is used to drive HHG.

After the plunger, a high vacuum valve is used to separate the soft X-ray generation system from the sample chamber, and another high vacuum valve is used between the sample chamber and the soft X-ray characterization system, which includes the Hettrick Scientific X-ray spectrometer, thin film filters, and the EUV-X-ray camera. Therefore, the soft X-ray generation system, the sample chamber, and the detection system are well separated, and we can work on each part of the X-ray beamline without venting the whole system.

In the sample chamber, the driving laser beam is blocked by a thin-film filter (0.2-μm Al or 0.2-μm Ag depends on the photon energy we generated and which part of the HHG spectrum we are interested in). Most of the HHG beam goes through the filter and is refocused by a nickel coated toroidal mirror down to 100 μm in diameter at a grazing incident angle of 4 degree. The efficiency of the toroidal mirror is around 30%. Then a mirror with hole is used to combine the pump and probe beams by letting the probe beam (HHG) pass though the hole, while the pump beam is reflected by the mirror. So the pump and probe beams nearly collinearly propagate through the sample. The sample is mounted on a three-dimensional motorized translation stage and a rotational stage for best coupling of the HHG beam though the sample. Then the pump beam is block by another thin-film filter and the HHG beam propagates to the detection system. After the sample chamber, the EUV-X-ray spectrometer, which is consisted of a pair of Kirkpatrick-Baez (KB) mirrors and a set of EUV-X-ray gratings, focuses and spectrally disperses the X-ray beam on the EUV-X-ray CCD.

For the pump beam, we can use either the 15% output of the amplifier or the residual 800-nm light (3 to 4 mJ) after the OPA. And by using nonlinear crystals, wavelengths of 200 nm, 267 nm, 400 nm, 500 nm, 1 μm, and 2 μm have all been achieved for the pump light. The pump beam goes through a delay line, which allows the timing match between the pump and probe beams. An iris is used to control the pump power. A shutter, which is synchronized with the CCD camera, is inserted to the pump beam to enable one shot pump-on and one shot pump-off measurement, which allows the subtraction of the pump-off measurement from the pump-on measurement in order to improve the signal to noise ratio.

3.3 Soft X-ray absorption spectroscopy

We measured the NEXAFS of samples in gas, solid, and liquid phase using the soft X-ray HHG beamline as shown in Fig. 3.4. In this section, I will discuss the sample geometries and the results.

3.3.1 Gas phase

A gas cell with a 2-mm path length and a 150-to-200-μm-diameter aperture, as shown in Fig. 3.5, is used for the gas phase experiment. The gas is supplied from a channel on the side by a 1/8-inch diameter hose. The gas density inside the gas cell is controlled by tuning the gas pressure in the hose. Typically, the pressure inside the gas cell is from 20 to 50 Torr to introduce enough absorption while still keep a good X-ray signal. The sample chamber is pumped by a 300 liters/s turbo pump, therefore, although the sample gas is leaking from the gas cell through the entrance and exit holes for the X-ray beam, the background gas pressure inside the sample chamber is being kept around 10 mTorr. Considering the sample chamber length is 40 cm, the absorption from background gas in the sample chamber to the total absorption signal is less than 10%. This number can be greatly improved by increasing the pumping capacity. If the background pressure is reduced to less than 1 mTorr, the absorption from the background gas in the chamber to the total absorption signal will be reduced to less than 1%, which could be neglected. For static XAS measurements, the absorption of background gas is not a problem, but for the dynamic XAS experiments, it will limit the signal to noise ratio.

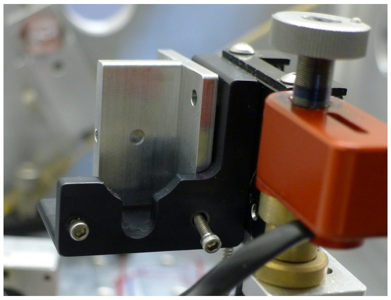

Figure 3.5: Picture of the gas cell.

By passing the harmonics through the sample cell flowing with gas, the absorption signal from the sample can be observed from the transmitted HHG spectrum (Fig. 3.6(b)). For SF_6 gas, using harmonics generated from Ne, we simultaneously observe three Sulfur 2p inner well resonance absorption peaks [128] $6a_{1g}$, $2t_{2g}$, $4e_g$, as well as the $2t_{2g}$ and $4e_g$ shape resonances. When the SF_6 gas transmission is measured using HHG from He, one additional Sulfur 2s Fano-type resonance absorption peak [129] $2s^{-1}\ 6t_{1u}$ appears in the spectrum. The absorption peak $6a_{1g}$, which is not obvious in the spectrum of the harmonics from Ne, is much sharper in the He HHG spectrum. Note that in the He data, an absorption at a photon energy of 285eV originates from the carbon K-edge, due to carbon contamination on the spectrometer optics. Thus, we can measure the absorption spectrum of multiple elements simultaneously.

Figure 3.6(b) also shows the 4d giant resonance absorption in Xe [130] at high spectral resolution using harmonics from Ar gas, which clearly resolves absorption from different spin states. This demonstrates element specificity and sensitivity to electronic structure over a very broad ~250 eV spectral range in a tabletop setup. High quality absorption spectra can be obtained by taking the logarithm of the ratio between the transmitted harmonic spectrum without and with the sample gas, for the same exposure time. Figure 3.6(c) shows the SF_6 Sulfur L-edge 2p orbital NEXAFS structure. Different transitions and spin states are clearly resolved and assigned using synchrotron data [128], and the 1.2 eV energy splitting due to the Sulfur 2p orbital spin states splitting in the absorption peaks $6a_{1g}$ and $2t_{2g}$ agrees well with synchrotron data as shown in Fig. 3.6(d, e). Although the energy resolution is currently 0.25 eV, limited by 160 g/mm groove density of the grating used in the setup, further increases in spectral resolution will be possible using a higher groove-density grating.

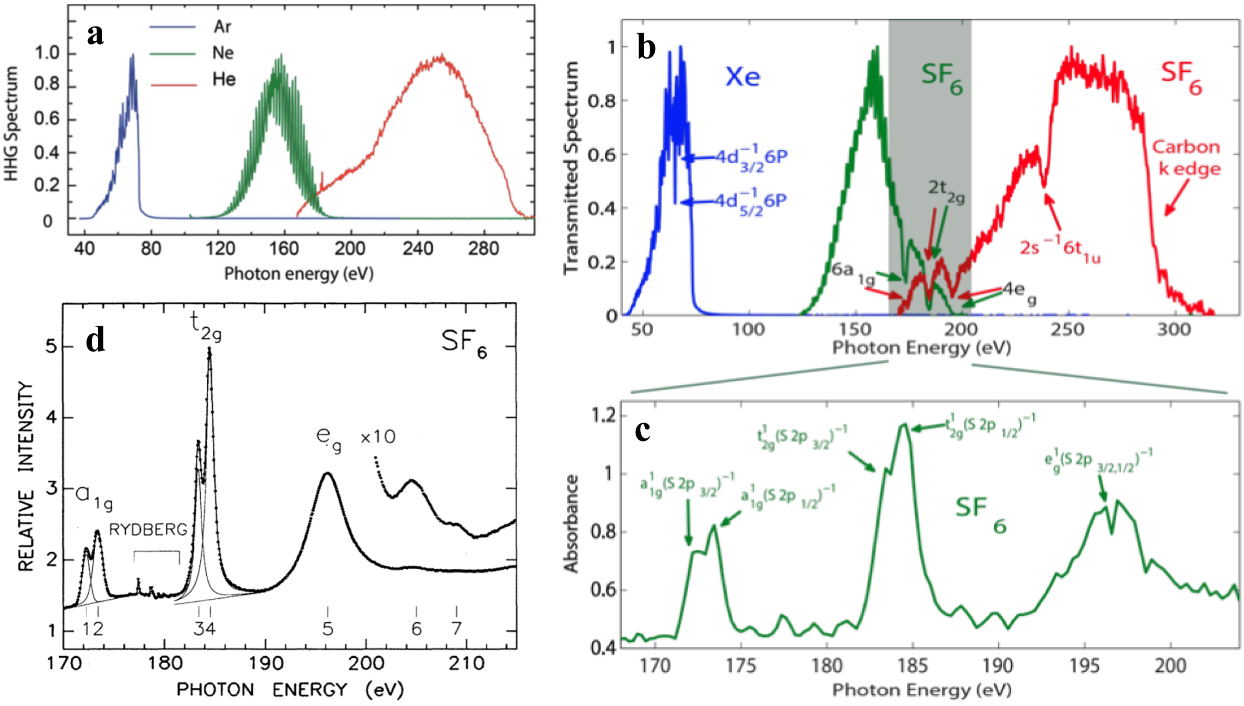

e SF_6 sulfur 2*p* inner-well resonances: Assignments and fit results.

Peak	Energy (eV)	Assignment	Intensity (arb. units)	Width (FWHM, eV)
1	172.27	$a_{1g}^1\ (\mathrm{S}\ 2p_{3/2})^{-1}$	1.00	0.87
2	173.44	$a_{1g}^1\ (\mathrm{S}\ 2p_{1/2})^{-1}$	1.62	1.06
3	183.40	$t_{2g}^1\ (\mathrm{S}\ 2p_{3/2})^{-1}$	2.71	0.76
4	184.57	$t_{2g}^1\ (\mathrm{S}\ 2p_{1/2})^{-1}$	5.53	0.85
5	196.2	$e_g^1\ (\mathrm{S}\ 2p_{1/2,3/2})^{-1}$	15.7	4.1
6	205	multielectron excitation?		
7	209	multielectron excitation?		

Figure 3.6: (a) Normalized HHG spectra from Ar, Ne and He with driving laser wavelength at 1.3 μm. (b) Normalized raw data for 1.3 μm driven HHG from Ar (blue), Ne (green), and He (red) after transmission through a 2-mm long sample cell of Xe (HHG from Ar), and SF_6 (HHG from Ne and He). Note that the apparent gap between 70 eV and 100 eV is because of Al filters used to block the driving laser light—full tuning across this range can be achieved by switching to other filters. (c) NEXAFS spectrum of SF_6 Sulfur L-edge 2p orbital. The high quality NEXAFS spectra were obtained in a 300-s exposure time. However, changes in the absorption

signal can be monitored in real time, with exposures as short as 0.1 s. The modulations between the resonance absorption peaks $6a_{1g}$, $2t_{2g}$, and $4e_g$ arise from individual harmonic peaks that are separated by 1.9 eV. These modulations can be reduced by increasing the driving pulse energy into the hollow waveguide, implementing beam pointing stabilization, and reducing the integration time. (d) Synchrotron data for SF_6 NEXAFS, which is captured from [128]. (e) Assignments of SF_6 sulfur 2p inner-well resonances, which is captured from [128].

We also measured the NEXAFS of gas CS_2 using the soft X-ray HHG source as shown in Fig. 3.7(a). We see NEXAFS of both SF_6 and CS_2 match excellently with measurements done by synchrotron (Fig 3.7(b)), demonstrating the brightness and stability of this soft X-ray HHG light source, as well as its ability in resolving absorption fine structures.

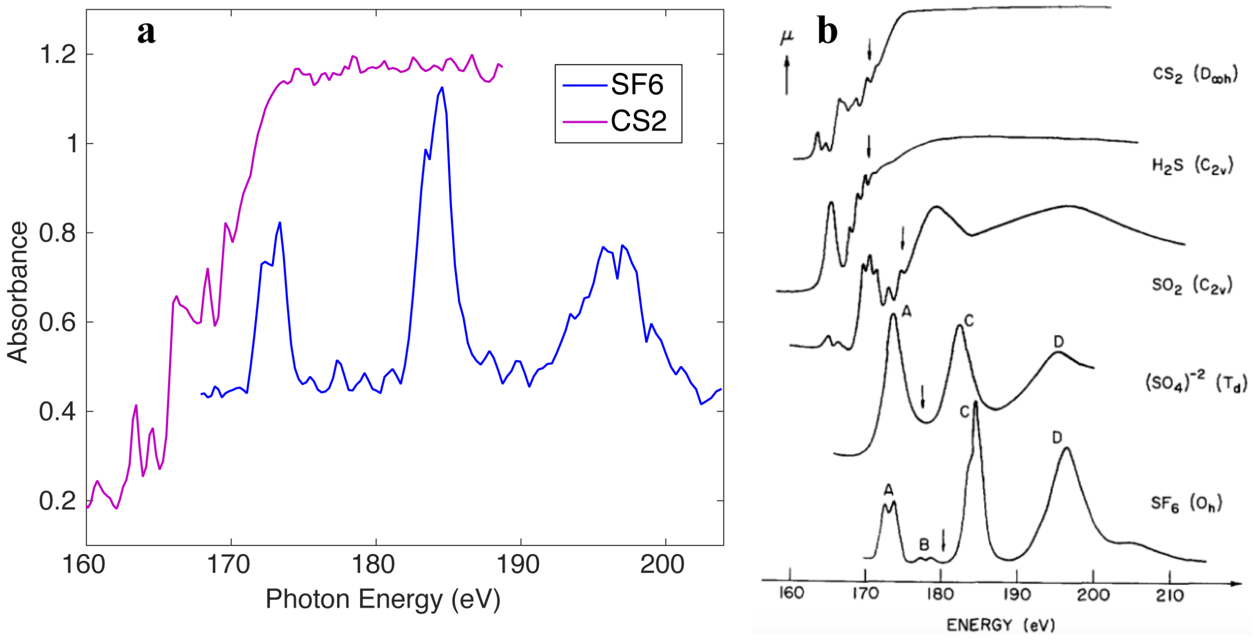

Figure 3.7: (a) NEXAFS of CS_2 and SF_6 using Soft X-ray HHG from Ne driven by a 1.3-μm wavelength laser. (b) Synchrotron data for NEXAFS of CS_2, H_2S, SO_2, $(SO_4)^{-2}$, and SF_6, which is captured from [131].

3.3.2 Transient absorption spectroscopy of Xe

The static XAS measurements demonstrate that the soft X-ray HHG light source we developed can be successfully used in spectroscopy applications. So the next step is to use this light source to probe molecular dynamics. We studied the ionization process of Xe gas using HHG from Ar. The residual 800-nm light of the OPA is focused by a lens with a 25-cm focal length into the gas cell to photon-ionize the Xe gas. The gas pressure of Xe inside of the gas cell is 30 Torr. The ionized gas induces additional absorption peaks. By recording HHG spectrum at different time steps relative to the pump beam, we can follow the photo-ionization dynamics of Xe by analyzing the absorption change of the HHG spectrum.

The neutral Xe 4d absorption peaks as shown in Fig. 3.8(a) match well with the data from synchrotron [130]. When the probe beam comes after the pump pulse, four introduced absorption peaks appear in the spectrum as shown in Fig. 3.8(b). The four absorption peaks are located at photon energies of 55.4 eV, 56.1 eV, 57.1 eV, and 57.6 eV. According to previous studies of the 4d gaint resonance of Xe ion [132], peak 1 and peak 2 correspond to the resonance of Xe^+ ($4d^{10}5p^5\ 2P \rightarrow 4d^95p^6\ 2D$), and the transitions are $2P_{3/2} \rightarrow 2D_{5/2}$ and $2P_{1/2} \rightarrow 2D_{3/2}$, respectively. Peak 3 and peak 4 correspond to the resonance of Xe^{2+} ($4d^{10}5p^4 \rightarrow 4d^95p^5$), which include four transitions theoretically. Additionally, the intensity ratios between peak 1 and peak 2, peaks 3 and peak 4 are close to the published oscillator strength ratios. Thus, the ability to resolve a set of congested absorption peaks demonstrates the fine frequency resolution of transient spectra using HHG light source. Furthermore, even without further compression, the HHG beam can be used to probe ultrafast dynamics on the order of tens of femtosecond. We recorded the transmitted HHG spectrum around the time zero of the pump and probe beams with a 10-fs step size to follow the ionization dynamics, as shown in Fig. 3.8(c) is the absorption dynamics obtained by subtracting the pump-off spectrum from the pump-on spectrum. The four absorption peaks build up within 75 fs after the time zero, indicating photo-ionization happens on the time scale of tens of femtoseocnd.

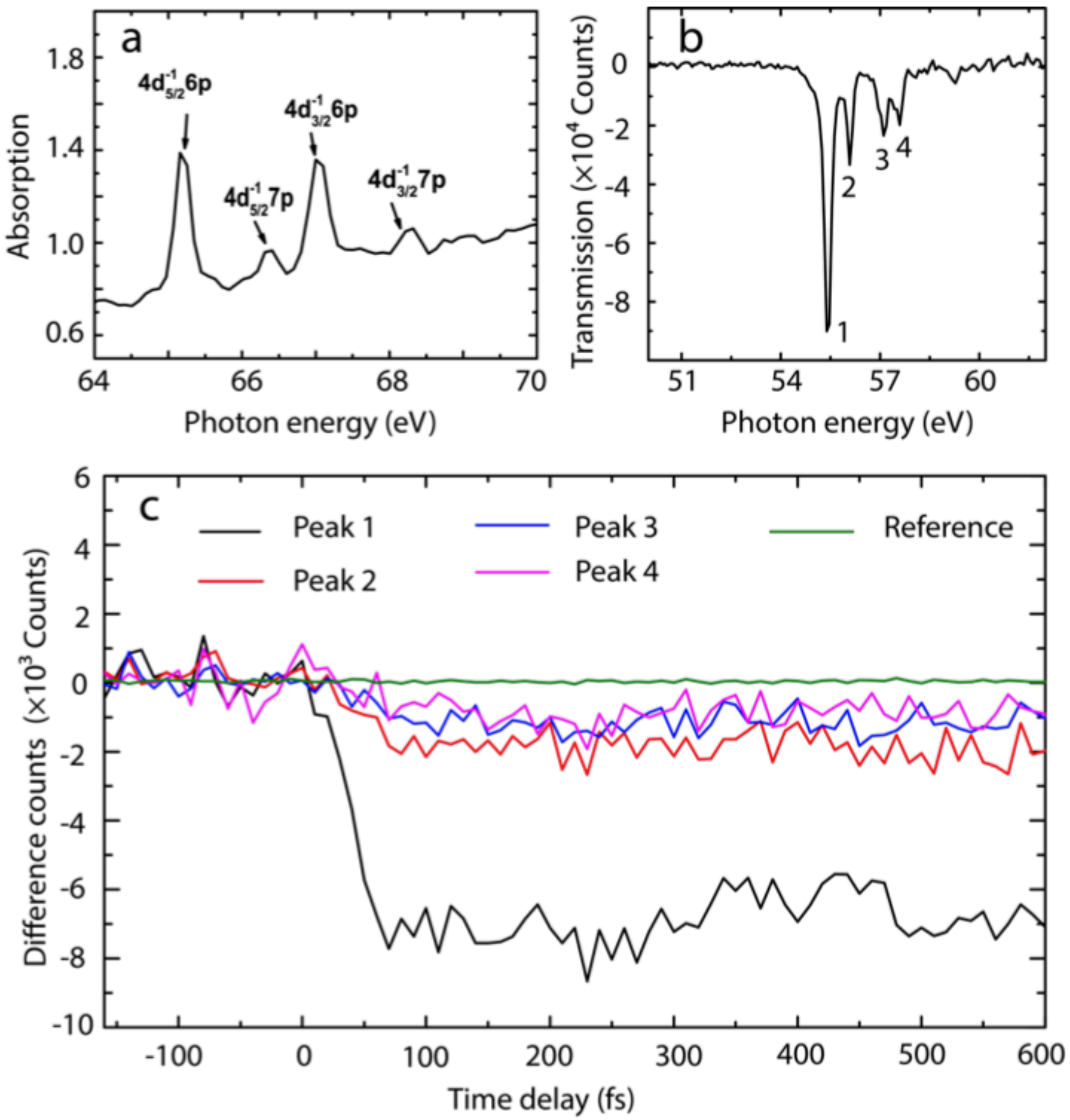

Figure 3.8: (a) 4d absorption spectrum of Neutral Xe. (b) 4d absorption spectrum of Xe^+ and Xe^{2+}. (c) Transient absorption dynamics of Xe^+ and Xe^{2+}.

3.3.3 Solid phase

After investigating the gas samples, the solid sample P3HT, Poly (3-hexylthiophene-2, 5-diyl), is measured because of its popularity for use in organic photovoltaics research and devices, and its potential of being used extensively as a semiconducting layer in organic thin film field effect transistor and solar cells. The sample is prepared by high-speed spin coating of P3HT solution on a thin (30-nm) silicon nitride membrane window. The 30-nm thick silicon nitride window absorbs 35% - 50% of the soft X-ray beam at photon energies from 100 eV to 200 eV. And the thickness of the sample is typically around tens to hundreds of nanometer depending on the solution density. The silicon nitride window is a 500-μm by 500-μm square, which is located at the center of a 7.5-mm by 7.5-mm square silicon substrate. Since the X-ray beam is focused down to 100 μm to 150 μm in diameter, the X-ray beam can go through the solid sample and window without any clipping. The motorized three-dimensional translation stage allows a good couple of the X-ray beam through the sample.

XAS of P3HT is measured using HHG from Ne driven by 1.3-μm laser beam as shown in Fig. 3.9(a), which is a HHG spectrum integrated over 10 min. Fig. 3.9(b) shows the HHG spectrum transmitted through the P3HT sample, taking under the same conditions as Fig. 3.9(a). From these two spectra, the absorbance of P3HT can be calculated, which resolves a pair of absorption peaks separated by 1.1 eV around 166 eV as shown in Fig. 3.9(d). In order to understand the transition of the peaks, I searched literature, and only found the absorption spectrum of thiophene (C_4H_4S) measured by Synchrotron (P3HT could be considered as the polymer of thiophene as shown by their chemical structures shown in Fig. 3.9(c) and (e)) [133]. In the absorption spectrum of thiophene, two absorption peaks X and Y are shown in the photon energy range we are discussing. Peak X corresponds to the transition of the S 2p electrons to closely spaced-unfilled molecular orbitals associated with the S-C bond in thiophene. And since thiophene is deposited on Pt

(111) substrate in the reference, peak Y is a substrate-enhanced atomic resonance in the continuum due to excitations to d-like final states [133]. Therefore, the absorption peaks shown in Fig. 3.9(d) are probably the transitions of the S 2p electrons to unfilled molecular orbitals of the S-C bond.

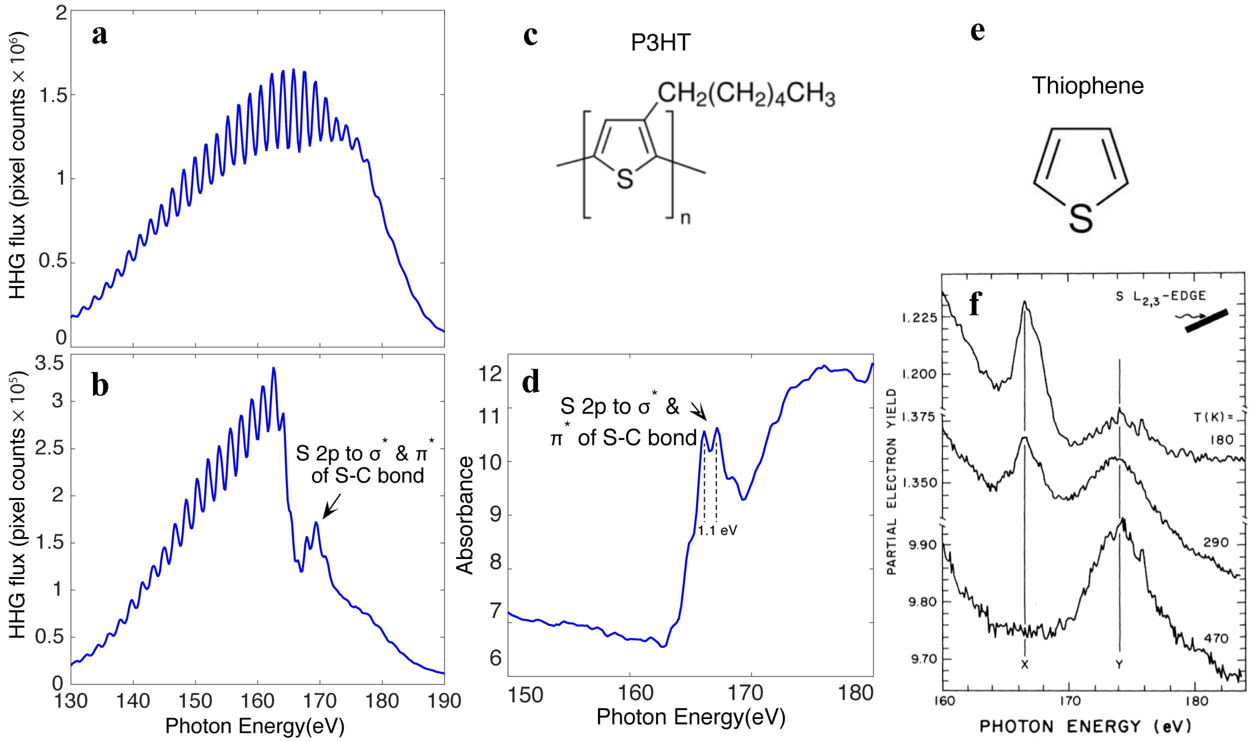

Figure 3.9: (a) HHG spectrum from Ne driven by laser field at a wavelength of 1.3 μm without the sample. The spectrum is integrated over 10 min. (b) HHG spectrum transmitted through the P3HT sample. The spectrum is taken by integration over 10 min. (c) Chemical structure of P3HT. (d) Absorbance of P3HT that resolves NEXAFS. (e) Chemical structure of thiophen. (f) NEXAFS of thiophene (C_4H_4S) on Pt (111). This figure is captured from [133].

3.3.4 Liquid phase

Over 70% of the earth's surface is covered by water [134]. On average, the adult human body is constituted of 50-65% of water [135]. Being such a common state of the environment, it is extremely important to understand water and molecules in the liquid phase. Simple molecules such as CH_3OH (methanol) and H_2O are well understood in the gas and solid phase, but their electronic and geometric properties are still controversial in the liquid state [136]. XAS is a powerful way to study these systems because of its element specificity and sensitivity to electronic, molecular, and geometrical structures. Since XAS is performed in vacuum because of the strong absorption of X-rays in atmosphere. One of the biggest challenges in performing liquid phase XAS experiments is sample preparation in vacuum. What's more, in order to conduct real time XAS experiments in liquid phase, we need to prepare refreshing liquid samples with a very short path length (~1 μm) under vacuum.

There are three ways to prepare such samples. 1. Liquid samples in vacuum can be prepared by using a liquid jet. In 2001, a liquid microjet technology was incorporated into a synchrotron X-ray experiment, thereby opening many new systems to study by this powerful technology [137]. The microjet is produced by using a syringe pump (Teledyne-Isco) to pressurize the liquid behind a fused silica capillary tip. Almost immediately (1 mm and 30 μs) after leaving the tip orifice, the liquid (30 μm in diameter) is intersected by the intense X-ray beam, wherein the sample is close to room temperature (>15 °C) [138]. In 2015, a liquid flatjet system was developed. The liquid flatjet is produced by two nozzles from which two impinging single jets form a 1-mm wide and 5-mm long liquid water sheet with a thickness of 1 - 2 μm, and using this flatjet XAS measurements in transmission was made on the nitrogen K-edge of aqueous NH_4^+ [139]. 2. Another way is to dissolve liquid samples in a liquid crystal film freely suspended within a metal frame. The liquid crystal film can be formed rapidly on-demand with thicknesses ranging from nanometers to micrometers. The liquid crystal used is 8CB (4'-octyl-4-cyanobiphenyl), which has a vapor pressure below 10^{-6} Torr, so films made at atmospheric pressure maintain their initial thickness after pumping to high vacuum [140].

In our experiment we use the third way, a liquid cell (from Insight Nanofluidics), in which a liquid film with a thickness of tens of nanometer to hundreds of nanometer is held between two 100-nm-thick (or 50-nm-thick) silicon nitride membranes suspended on a silicon substrate [136]. A pair of holes allows the liquid to flow in and out of the cell. The entire sample cell is housed in an o-ring sealed metal enclosure and mounted in the vacuum chamber. And the liquid is pumped in and out of the system by using a syringe pump from KD scientific (model 200 series).

The liquid cell has been used under atmosphere by research groups [141, 142], or when the sample chamber is filled with He gas because He gas is almost transparent to X-rays with photon energies above 200 eV [143]. However, this liquid cell does not work well in vacuum since there is a big pressure difference between the two sides of the thin silicon nitride membranes and the membranes will deform, causing a much larger and un-uniform sample thickness. We tested the liquid cell by checking the absorption of CH_2I_2 between 40 to 60 eV. There is an absorption dip right at 50 eV for CH_2I_2. Based on website CXRO, the transmission of a 200-nm thickness CH_2I_2 is about 0.6 as shown in Fig. 3.10(b). But based on our measurement as shown in Fig. 3.10(a), only 0.025% HHG light between 40 to 60eV passed through the sample, which suggests a sample thickness of around 3 μm. The deformation of the thin membranes causes a much larger sample thickness and only a small amount of the EUV light transmitted through the much thicker sample, which can be clearly seen in Fig. 3.10(a) that HHG went through the liquid sample is very dim and noisy.

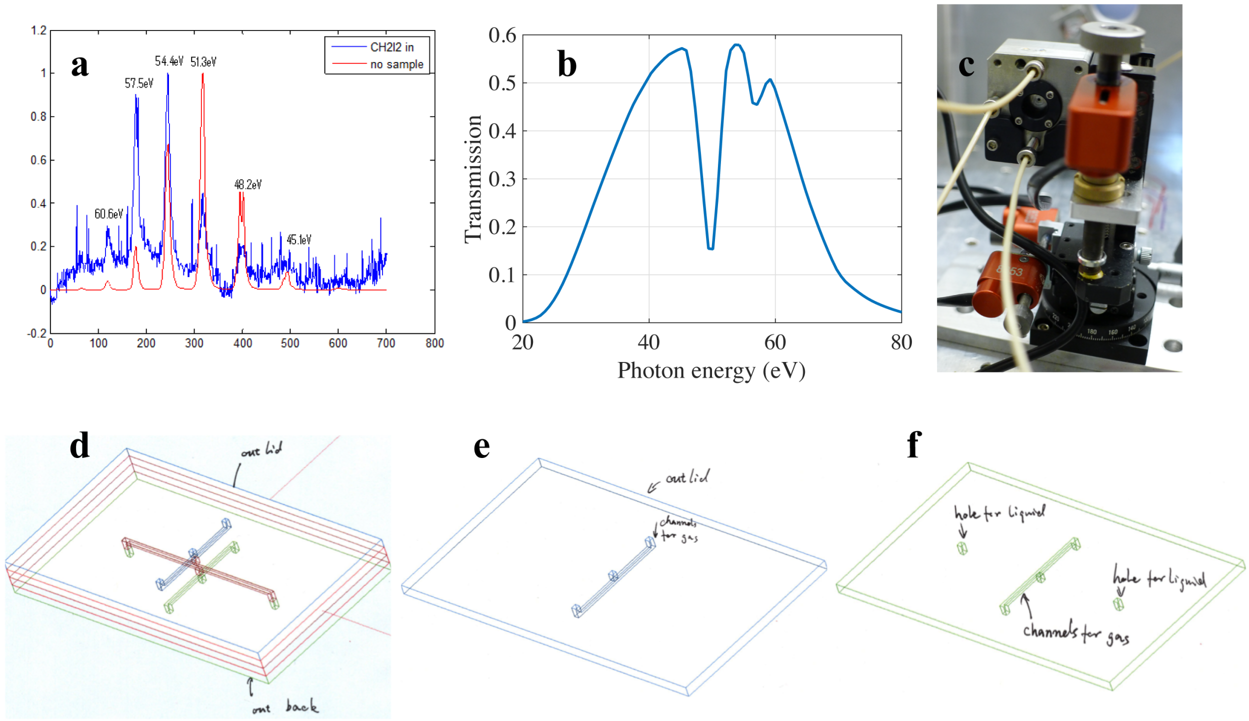

Figure 3.10: (a) HHG spectrum without going through CH_2I_2 (red curve) and with going through CH_2I_2 (blue curve). (b) Transmission of CH_2I_2 captured from CXRO. (c) 2nd version liquid cell. (d) 3rd version liquid cell, four silicon-subtract pieces (with thin silicon nitride membrane, and necessary other structures on each piece) stack together to create three compartments, one for liquid and two for gas. (e) Out lid piece of the 3rd version liquid cell. (f) Out back piece of the 3rd version liquid cell.

In order to get the liquid cell working in vacuum, we modified the design of the metal enclosure with JILA machine shop to create three compartments, one of which allows the flowing of liquid, and the other two allow the flow of He gas by adding two more thin silicon nitride membranes with 50-nm or 30-nm thickness to balance the interior pressure inside the liquid compartment. The thickness of the gas compartments is 12 mm in total (6 mm for each compartment). As shown in Fig. 3.10(c) is the modified metal enclosure, the top and bottom hoses allows the flowing of liquid through the liquid compartment, the hose on the left (one more on the back side) allows the flowing of gas through the two gas compartments. The black cap allows the mounting of the thin silicon nitride membrane for gas compartments. We need around 300 Torr of He gas to eliminate the deformation of the liquid cell by imaging the cell using interferometry. It turns out HHG with photon energies below 100 eV will be fully absorbed by the four silicon nitride thin films and the He gas. However, this version of liquid cell should work great for X-rays with photon energies above 100 eV where He gas is more transparent.

In order to get the liquid cell work for liquid systems under 100 eV, we modified the design again. As shown in Fig. 3.10(d), we add two more silicon nitride membranes, stacking together with the other two membranes and enclosing all of them together by the metal enclosure. The out lid and out back piece both have a gas flowing channel, two holes as gas inlet and outlet as shown in Fig. 3.10(e) and (f). The out back piece has another two more holes as liquid inlet and outlet. This version of liquid cell has three compartments created by four very thin silicon nitride windows sealed from the vacuum. Liquid sample flows through the central compartment, while the other two compartments are flowed with noble gas at atmosphere pressure, thus keeping the films of the central compartment from deformation. The noble gas only has a very short path length (less than 1 mm), resulting very few soft X-ray flux reductions. We employed the Colorado Nanofabrication Lab (CNL) in the University of Colorado to develop the out lid and out back pieces and successfully developed the liquid cell (please refer to appendix 1 for the cell fabrication process), and the machine shop in JILA developed the new metal enclosure that works for this version of liquid cell. The newly designed liquid cell and cell holder are under testing.

3.4 Summary

In summary, in this chapter I first introduced XAS. Then the experimental setup was presented. Finally, Static NEXAFS in gas, solid, and liquid phase, as well as XAS dynamics of Xe are discussed.

Chapter 4

Bright circularly polarized soft X-ray high harmonics for X-ray magnetic circular dichroism

In this chapter, I will present the development of the first soft X-ray CPHHG and use it for XMCD measurement of Gd/Fe multilayer to prove its brightness, stability, and circularity. Sing-atom and macroscopic physics of CPHHG will be covered. The spectral and temporal properties of CPHHG, the polarization state of CPHHG, and future directions to extend CPHHG to higher photon energies will be discussed. Moreover, flux characterization of CPHHG shows that CPHHG has a similar flux level with LPHHG.

4.1 Introduction

As discussed in earlier chapters, HHG results from an extreme nonlinear quantum response of atoms to intense laser fields. When implemented in a phase-matched geometry, bright, coherent HHG beams can extend to photon energies beyond 1.6 keV [5, 7]. What's more, HHG has been successfully used in many applications. For many years however, polarization of bright HHG, which is a fundamental property of light and light matter interaction, was limited to linear polarization – precluding many applications in probing and characterizing magnetic materials and nanostructures, as well as chiral phenomena in general. Although X-ray optics can in principle be used to convert EUV and X-ray light from linear to circular polarization, in practice such optics are challenging to fabricate and have poor throughput and limited bandwidth [38]. A more appealing option is the direct generation of elliptically polarized [39-41] and CP [43, 44, 144] high harmonics. However, these methods only generate CPHHG in the EUV region so far. CPHHG driven by collinearly propagated two-color counter-rotating CP beams is the first generation scheme that generates CPHHG in the soft X-ray region [33].

HHG driven by collinearly propagated two-color counter-rotating CP beams was first proposed and experimentally demonstrated in 1995 [43]. However, the process was not phase-matched and the polarization was not measured. Later on, this scheme was studied theoretically from single-atom view [44-49]. In 2014, the polarization of the high harmonics generated using this scheme was measured to be circular [31]. In early 2015, bright phase-matched CPHHG was generated in the EUV region at wavelengths $\lambda>18$ nm by using a combination of 0.8 μm and its second harmonic counter-rotating CP driving fields, and used for EUV magnetic circular dichroism measurements [32].

In the first half of this chapter I will show the first experimental demonstration of CPHHG in the soft X-ray region to wavelengths $\lambda<8$ nm, and use them to implement XMCD measurements using a tabletop-scale setup. By using counter-rotating driving lasers at 0.79 μm (1.57 eV) and 1.3 μm (0.95 eV), I generate bright soft X-ray CPHHG beams with photon energies greater than 160 eV [33, 145] and with photon flux comparable to the HHG flux obtained using LP 800-nm driving lasers [115]. Moreover, we implement the first advanced simulations of the coherent buildup of CPHHG to show how the macroscopic phase-matching physics and ellipticity of the driving lasers influence the HHG spectra, number of attosecond bursts, as well as the degree of circular polarization.

This work presents several new capabilities and findings. First, CPHHG provides a unique route for generating bright narrowband ($\lambda/\Delta\lambda>400$) harmonic peaks in the soft X-ray region, to complement the soft X-ray supercontinua that are produced with LP mid-IR lasers [7, 28, 115]. This capability is significant because it provides an elegant and efficient route for shaping soft X-ray light by manipulating the driving laser light, and is very useful for applications in high-resolution coherent imaging and photoelectron spectroscopies. Second, I will show that the macroscopic phase-matching physics of soft X-ray CPHHG driven by mid-IR lasers has similarities to LPHHG, where the number of bright attosecond bursts is limited by the finite phase matching temporal window. Third, I implement the first tabletop XMCD measurements at the $N_{4,5}$ absorption edges of Gd. The Gd/Fe multilayer sample is a candidate material for next-generation all-optical magnetic storage devices [146], but has been inaccessible to HHG XMCD until now. This capability also opens up the possibility of probing spin dynamics in rare-earth elements using HHG, which has been successfully employed for 3d-transition metals to uncover the fastest spin dynamics using EUV HHG [147, 148]. Finally and most importantly, these results demonstrate the universal nature of CPHHG that can be generated across the EUV and soft X-ray spectral regions using a broad range of driving laser wavelengths.

This generation scheme has intrigued broad interests and its temporal and spectral properties are widely studied [50-56]. In the second half of this chapter, I will present bright phase-matched CPHHG generated, for the first time, by using beams with wavelength of 2 μm and 0.79 μm. The harmonic spectra exhibit pairs of harmonics with opposite helicities and the harmonics are very close to evenly spaced, which are determined by conservation laws. Besides, the spectra exhibit helicity dependent intensity asymmetry, by analyzing the helicity dependent intensity asymmetry of CPHHG driven by different wavelengths from different gas targets, I will show that the helicity dependent intensity asymmetry is mostly caused by the helicity dependent single-atom physics [50, 51, 149], which exhibits different behaviors for different gas targets. What's more, this asymmetry can reverse and very interestingly, CPHHG from Ar exhibits a single helicity at high-photon-energy region of the spectrum, this provides a convenient way to generate CPHHG with a single helicity and CP attosecond pulse trains. Simulations of the main harmonics and the additional channels allowed by the imperfect circularity of the driving beams show guidance for choosing the wavelength of the two beams when using this scheme to generate CPHHG, and for generating CPHHG at higher photon energies. Finally, I will show that the cutoff energy of CPHHG generally falls between the cutoff energies (or phase-matching cutoff energies) of LPHHG of the two beams, and is much closer to the phase-matching cutoff energy of LPHHG of the beam with shorter wavelength. What's more, the cutoff energy of CPHHG can be greatly increased by increasing the ionization potential of the gas target and by increasing the wavelength of the driving beam with shorter wavelength.

4.2 Circularly polarized high harmonics by 1.3 μm + 0.79 μm

In this experiment, I use a single-stage Ti:sapphire regenerative amplifier with an output energy of 8.2 mJ per pulse, at a 1-kHz repetition rate, and a 0.79-μm central wavelength [115]. Approximately 80% of the output energy is directed into a three-stage OPA that generates a 1.6-mJ/pulse signal beam at 1.3 μm, as well as a 1-mJ/pulse idler beam at 2 μm. The polarizations of the signal beam and the remaining 20% of the 0.79-μm beam are then converted to counter-rotating circular polarization using half- and quarter-wave plates. A delay line is used for adjusting the relative time delay between the two fields. Both beams are then combined by a dichroic mirror and focused into a 150-μm inner diameter, 1-cm long, gas-filled hollow-core waveguide. The pulse durations of the 0.79-μm and 1.3-μm beams are ~55 fs and ~35 fs, respectively. As illustrated schematically in Fig. 4.1, the counter-rotating bi-chromatic drivers interact with a noble gas inside the fiber, generating CPHHG that propagate through a spectrometer and are recorded by a CCD. After the fiber, the two driving lasers are blocked using either 0.4 μm Al or 0.4 μm Zr filter, which transmit in the range of 20 eV to 72 eV and 70 eV to 190 eV [150], respectively.

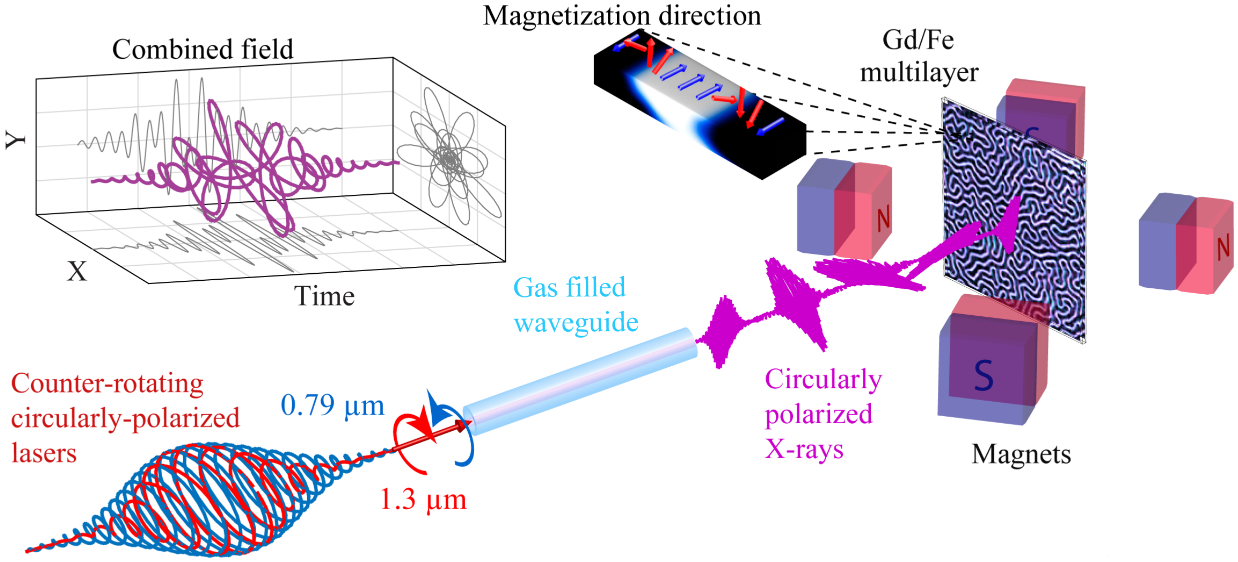

Figure 4.1: Experimental scheme of CPHHG. Bright soft X-ray CPHHG beams are generated by focusing 0.79-μm and 1.3-μm counter-rotating CP laser fields into a gas filled waveguide. They are then used for XMCD measurements at the $N_{4,5}$ absorption edges of Gd, as well as the $M_{2,3}$ absorption edge of Fe from an out-of-plane magnetized Gd/Fe multilayer sample. Left inset: combined field of the two drivers.

For the first set of experiments, I filled the waveguide with Ar, Ne or He gas. As shown in Fig. 4.2, all HHG spectra exhibit a well-separated HHG peak-pair structure, where the harmonics within each pair possess opposite helicity. The HHG spectra from Ar and Ne terminate slightly above 50 eV and 120 eV, respectively, while for He, bright CPHHG extends dramatically beyond the previous limit of 70 eV [32] to >160 eV. Moreover, CPHHG driven by 0.79-μm and 1.3-μm lasers covers a much broader spectrum compared with CPHHG driven by 0.8 μm and its second harmonic [32]. This is similar to the case for LPHHG, where long wavelength lasers generate the broadest HHG spectrum and can support the shortest transform-limited HHG pulse durations. Finally, the soft X-ray HHG spectra from Ne, and especially He, appear to merge into an underlying supercontinuum, which as discussed below, is a result of peak broadening caused by the narrow phase matching temporal window (~8 fs) [75], combined with additional peaks induced by slightly elliptical (~0.99) broadband driving lasers [31, 52, 53].

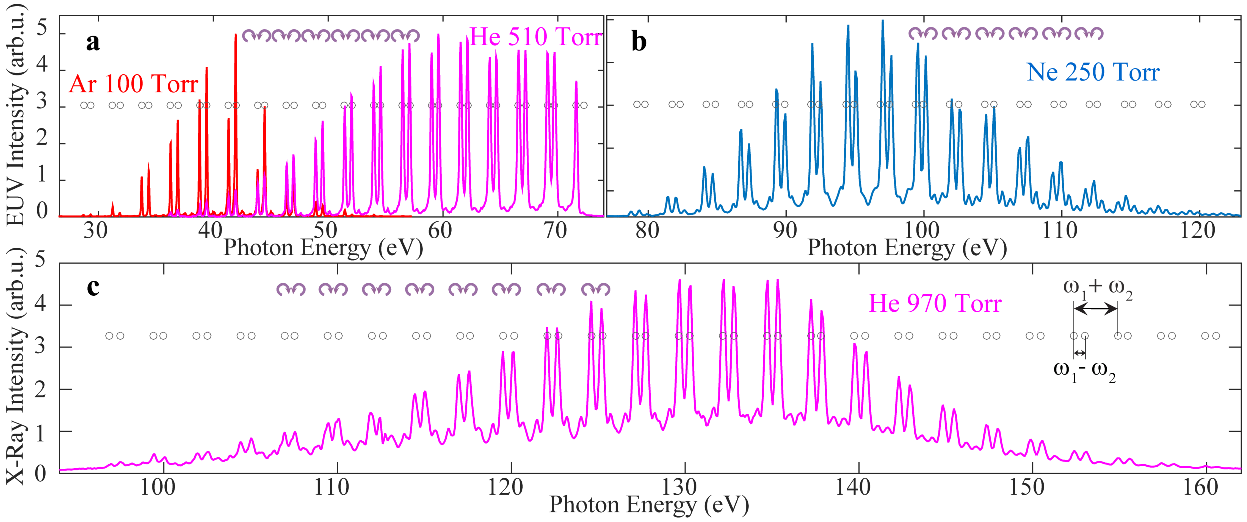

Figure 4.2: EUV and soft X-ray CPHHG. Experimental HHG spectra generated from Ar (a), Ne (b), and He (a and c) driven by counter-rotating CP 0.79-μm and 1.3-

μm laser fields. All spectra show a peak-pair structure, located at positions predicted by energy and spin angular momentum conservation (circles). The separation within each pair is $\omega_1 - \omega_2$, while different pairs are separated by $\omega_1 + \omega_2$.

We can describe the experimentally observed HHG spectra in terms of the conservation of energy and photon spin angular momentum [5, 31, 44, 52, 53]. In general, conservation of energy gives $\omega_c = n\omega_1 + l\omega_2$, for the circular harmonic ω_c generated from n photons of frequency ω_1 and l photons of frequency ω_2. Spin angular momentum conservation for generating circular polarization requires $l = n \pm 1$. Thus $\omega_c = n\omega_1 + (n \pm 1)\omega_2$. This gives rise to pairs of adjacent harmonics with opposite circular polarizations, and with a photon energy difference of $\omega_1 - \omega_2$ between the harmonics within each pair, and $\omega_1 + \omega_2$ between adjacent pairs. If we define $\omega_1 = q\omega_2$, where q can be any number, we obtain $\omega_c = n(q + 1)\omega_2 \pm \omega_2$. For the simple case of HHG driven by ω and 2ω, where $\omega_1 = 2\omega_2$, it follows that $\omega_c = (3n \pm 1)\omega_2$, thereby resulting in a unique spectrum where every third harmonic order is missing. For the driving laser wavelengths studied here (0.79 μm and 1.3 μm), $\omega_c \approx (2.65n \pm 1)\omega_2$. As Fig. 4.2 shows, the experimentally generated HHG peak positions well match those predicted by the selection rules.

4.2.1 Single-atom simulations

We performed microscopic and macroscopic simulations for CPHHG from He in order to unveil the physics underlying this unique soft X-ray HHG source. For the single-atom simulations, we identified the relevant quantum trajectories using the SFA and quantum orbit theory [48] and applying the corresponding semi-classical three step model [45-47]. For simplification, the microscopic simulations were done at a central wavelength of 0.78 μm (different from but close to the experimental value of 0.79 μm for simplification, this small modification of the driving wavelengths does not significantly change the physics except that the orientation of the trajectories will change slightly) since for driving wavelengths of 1.3 μm and 0.78 μm, the combined field (see Fig. 4.3(b)) repeats itself in an 8-fold symmetry shape every 13 fs. The driving field intensities used are $I_1 = 2.48\times 10^{14}\ W/cm^2$ and $I_2 = 2.24\times10^{14}\ W/cm^2$.

Figure 4.3(a) shows the dominant electron trajectories for a photon energy of 100 eV. In general, the electron tunnels a few atomic units away from the nucleus [151] and moves on a simple out-and-back trajectory, before recombining and emitting a harmonic photon. Ionization, recollision and HHG occur 8 times each 13 fs, as shown in Fig. 4.3(b). As a result, the HHG emission emerges as a series of 8 LP attosecond bursts every 13 fs, with each burst rotated with respect to the previous one, until the amplitude of the laser field drops below the threshold for HHG. Note that the linear polarization results from the sum of counter-rotating CP harmonics [49]. I would like to point out here that the complex 3D waveform of CPHHG has been experimentally fully reconstructed by using the laser-assisted photoelectric effect from surfaces. The results show in the temporal domain CPHHG does exhibit a sequence of quasi-LP bursts with a rotating polarization [152]

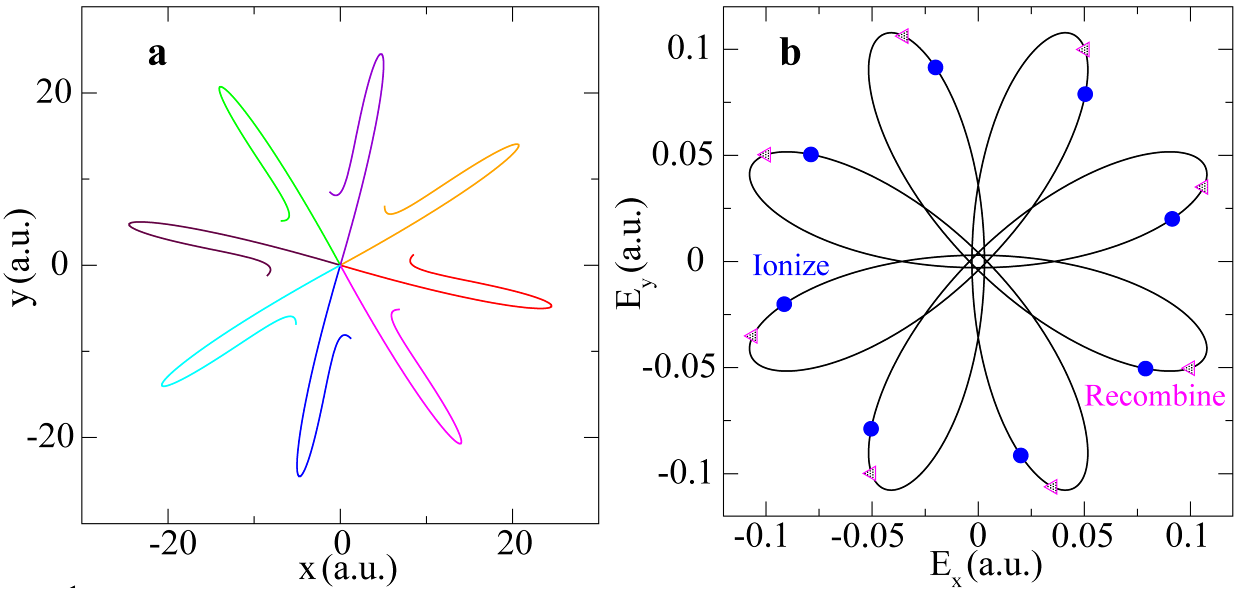

Figure 4.3: (a) Dominant electron trajectories for counter-rotating CP lasers that result in the emission of a 100 eV photon. (b) Laser wavelengths of 1.3 μm and 0.78 μm generate an 8-fold symmetric field, where the ionization (circles) and recombination (triangles) times for the trajectories in (a) are indicated.

Besides the dominant electron trajectories, the simulations reveal that there are two more classes of more complicated electron trajectories contributing to the HHG process, as evidenced by the three maxima corresponding to different travel times in Fig. 4.4(a). The electrons can be ionized at different times near the peak of the laser field, and thus they can travel in different trajectories, where each trajectory corresponds to different ionization times and different initial conditions. The largest contribution is from the trajectories that spend the shortest time in the continuum (Fig. 4.4(b)) and travel in a mostly "out-and-back" journey. However, these single-atom simulations show that trajectories with longer travel times make a significant contribution as well. Fig. 4.4(c) shows both an out-and-back trajectory and two additional trajectories that move in a more complicated 2D fashion. Fig.

4.4(d) shows the electric field experienced by the electron that travels in each of the three trajectories in Fig. 4.4(c), with their ionization and recombination times denoted.

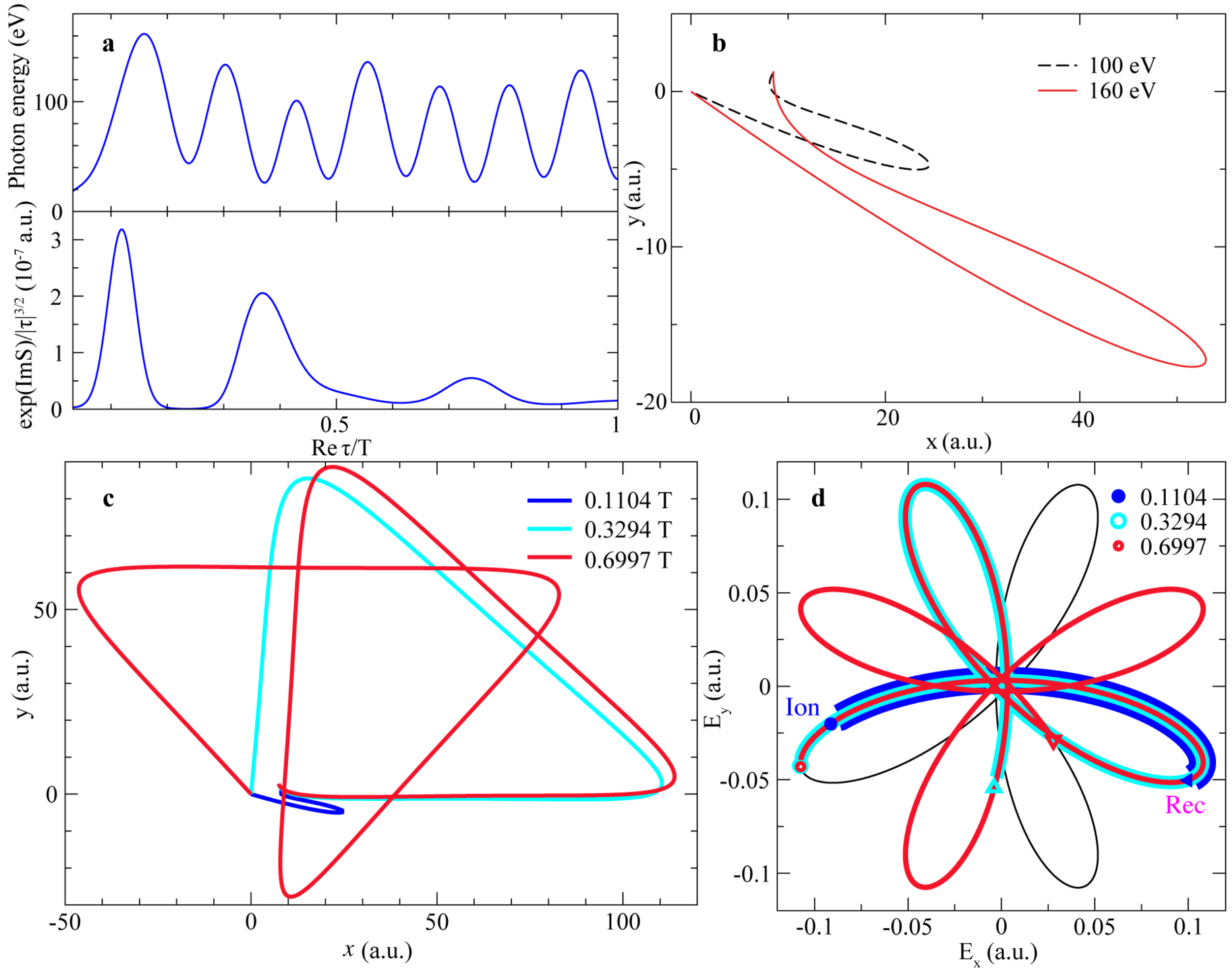

Figure 4.4: (a) Top: HHG photon energy as a function of the electron travel time τ (in units of the period $T = 2\pi/\omega_0$, $\omega_0 = 2\pi c/\lambda_0$, where λ_0 is the smallest common multiple of the driving laser wavelengths, i.e. $\lambda_0 = 3.9$ μm). The electron travel time refers to the total time it takes from ionization to recombination of the electron. Bottom: $\exp(\mathrm{Im}S)/|\tau|^{3/2}$, which is proportional to the probability of the HHG process, as a function of the electron travel time, where S is the action. (b)

Dominant trajectories for photon energies 100 eV and 160 eV. (c) Three example trajectories corresponding to a photon energy of 100 eV in the three maximum value regions at the bottom of (a), which have travel times of 0.1104 T (blue, dominant), 0.3294 T (green), and 0.6997 T (red). (d) Ionization (circles) and recombination (triangles) time are denoted on the combined driving field corresponding to the three trajectories in (c).

At the end of this section, I summarize some of the general principles of CPHHG driven by counter-rotating CP, bi-chromatic laser fields with wavelengths λ_1 and λ_2. We assume that the driving laser fields are perfectly CP with a flat envelope. If λ_1 and λ_2 have the smallest common multiple λ_0, the combined electric field will possess $n_1 + n_2$ fold symmetry, where $n_1 = \lambda_0/\lambda_1$ and $n_2 = \lambda_0/\lambda_2$. From the perspective of cycle time, the cycle times of λ_1 and λ_2 are $t_1 = \lambda_1/c$ and $t_2 = \lambda_2/c$. We have $n_1t_1 = n_2t_2 = \lambda_0/c$, thus the combined field has a periodicity of λ_0/c. Following the symmetry of the electric field, the field-driven electron trajectories will also possess $n_1 + n_2$ fold symmetry. The generated waveform will then be an attosecond pulse train, where each attosecond pulse is LP, but rotated with respect to the previous pulse. The polarization will have $n_1 + n_2$ unique orientations, and the pulse train will possess $n_1 + n_2$ fold symmetry.

For example, for the previously studied $\omega + 2\omega$ case [32], $\lambda_1 = \lambda_0/2$ and $\lambda_2 = \lambda_0$, so the combined field possesses 3-fold symmetry, and the generated attosecond pulse train consists of LP pulses orientated in 3 unique directions [49]. The combined field for $\lambda_1 = 0.78$ μm and $\lambda_2 = 1.3$ μm has a smallest common multiple of $\lambda_0 = 3.9$ μm, thus $n_1 = 5$ and $n_2 = 3$, so the combined field possesses 8-fold symmetry (Fig. 4.5(a)). However, for the case of $\lambda_1 = 0.79$ μm and $\lambda_2 = 1.3$ μm (Figs. 4.5(b,c)), $\lambda_0 = 130 \times 790$ nm $= 79 \times 1300$ nm $= 102700$ nm, thus $n_1 = 130$ and $n_2 = 79$, so the combined field possesses 130 + 79 = 209 fold symmetry and won't repeat until a cycle time of equivalent to a wavelength of 102700 nm. Moreover, the attosecond pulse train consists of LP bursts with 1 + λ_2/λ_1 bursts per longer wavelength driving field cycle (on average), which is 3 bursts per ω driving field cycle for the ω + 2ω case, and approximately 2.6 bursts per 1.3 μm field cycle for the 0.79 μm + 1.3 μm case that we study in this paper.

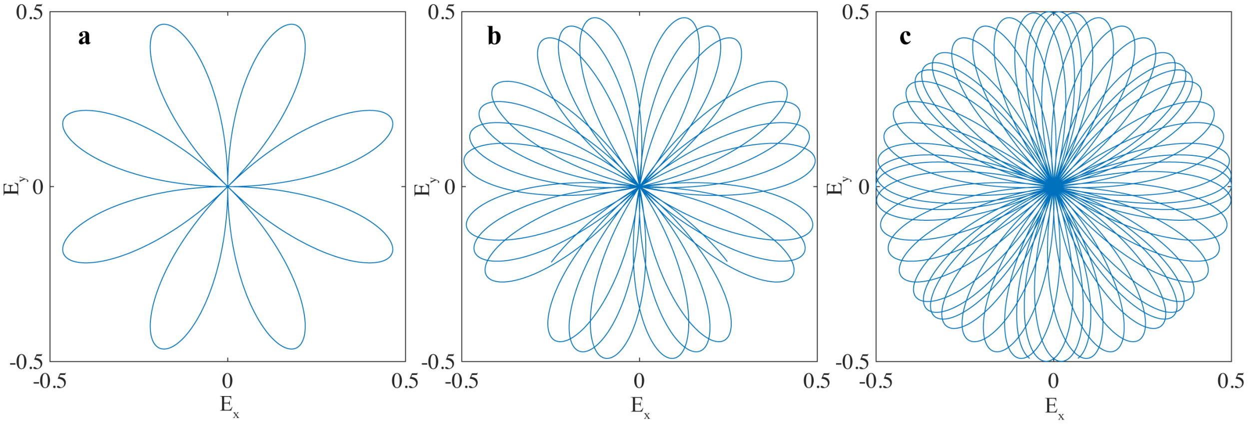

Figure 4.5: Combined fields of two-color counter-rotating CP laser beams. (a) 0.78 μm and 1.3 μm (b) 0.79 μm and 1.3 μm, over 10 cycles of the 1.3 μm field. (c) 0.79 μm and 1.3 μm, over 20 cycles of the 1.3 μm field.

4.2.2 Phase matching of circularly polarized high harmonics

As discussed in chapter 3, phase matching is essential for generating bright high harmonic beams that are useful for applications. In this section I will first talk about phase matching of CPHHG, which turns out to be robust by comparing with HHG by LP bi-chromatic fields. Then I will deduce the phase-matching equation of CPHHG. Finally I will show the advanced 1D phase-matching propagation simulations of CPHHG, from which we find out that the phase matching window of CPHHG driven by longer wavelength is shorter and only five bright bursts are emitted, hence the harmonic linewidth becomes broader. What's more imperfect circularity of the driving beams introduces new generation channels that leads to new small peaks surrounding the main harmonics, resulting an underlying supercontinuum when combining with broadened each harmonic peak.

For HHG driven by LP bi-chromatic fields, phase matching is challenging to fulfill because the conversion process is sensitive to any phase slip between the two fields. As shown in Fig. 4.6(a) when there is a phase slip between the two fields, either by not matched CEP between the two colors or different dispersion of the two colors in a dispersive medium, the waveform (the amplitude) of the combined field will change, thus the intrinsic phases of the re-colliding electrons will change, preventing stable HHG. Fortunately, when the two colors are counter-rotating CP, any phase slip between the two fields will not change the shape of the combined field, it simply causes a field rotation as shown in Fig. 4.6(b). This rotation does not influence the ionization and path length of the re-colliding electron and the intrinsic phase it accumulates, so will not influence the phase matching of the process [32]. Thus phase mismatch of CPHHG is determined only by the extrinsic phase. And phase matching of CPHHG is robust and can be achieved by tuning the gas pressure.

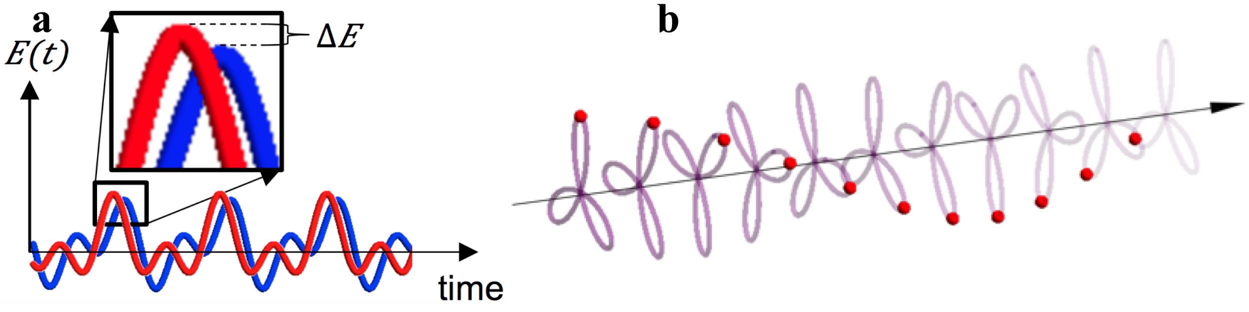

Figure 4.6: (a) Combined field of LP bi-chromatic fields (red) and when there is a phase slip between the LP bi-chromatic fields (blue). (b) A sequence of the combined field of counter-rotating CP bi-chromatic fields over time when phase slip is accumulating between the two fields. This figure is captured from [54].

Here I deduce the phase mismatch equation of CPHHG Δk, which is determined only by the extrinsic phase. So

$$\Delta k = k_c - nk_1 - lk_2 \qquad (4.1)$$

Here $k_c = \frac{2\pi}{\lambda_c}$, $k_1 = \frac{2\pi n_1}{\lambda_1} = \frac{2\pi(\Delta n_1+1)}{\lambda_1}$, and $k_2 = \frac{2\pi n_2}{\lambda_2} = \frac{2\pi(\Delta n_2+1)}{\lambda_2}$ are the wavevectors for circular high harmonic, the shorter-wavelength-driving beam, and the longer-wavelength-driving beam. n and $l = n \pm 1$ are the number of photons absorbed of the shorter-wavelength-driving beam and the longer-wavelength-driving beam to generate a circular harmonic photon as defined earlier. λ_c, λ_1, and $\lambda_2 = q\lambda_1$ are the vacuum wavelengths of the circular beam, the shorter-wavelength-driving beam, and the longer-wavelength-driving beam. The three wavelengths satisfy the equation: $\frac{1}{\lambda_c} = \frac{n}{\lambda_1} + \frac{l}{\lambda_2}$, so the phase mismatch equation can be rewrote as:

$$\Delta k = \frac{2\pi}{\lambda_c} - \frac{2\pi nq(\Delta n_1+1)}{\lambda_2} - \frac{2\pi l(\Delta n_2+1)}{\lambda_2} = -\frac{2\pi}{\lambda_2}(nq\Delta n_1 + l\Delta n_2) \qquad (4.2)$$

$$\Delta n_i = \frac{\lambda_i k_i}{2\pi} - 1 = -\frac{\mu_{11}^2 \lambda_i^2}{8\pi^2 a^2} + P\left[(1-\eta)\Delta n_{i\_1atm} - \frac{1}{2\pi}\eta N_{1atm} r_e \lambda_i^2\right] \qquad (4.3)$$

Here, $i = 1$ for the shorter-wavelength-driving beam and $i = 2$ for the longer-wavelength-driving beam. $\Delta n_{i\_1atm} = n_{i\_1atm} - 1$, where n_{i_1atm} is the index of fraction of the driving laser beam in one atmosphere of the gas medium. All the other parameters are defined in section 2.3 of chapter 2.

By setting equation 4.2 to zero, we can achieve the full phase-matching conditions, i.e. the coherent length is infinity, of CPHHG as the following equation:

$$\frac{\boldsymbol{\Delta n_1}}{\boldsymbol{\Delta n_2}} = -\frac{\boldsymbol{l}}{\boldsymbol{nq}} = -\frac{\boldsymbol{n \pm 1}}{\boldsymbol{nq}} \qquad (4.4)$$

From equation 4.4 we can see the two families of CPHHG with different helicities have different full phase-matching conditions and inside each family of CPHHG, only a single harmonic can be fully phase-matched.

To fully explain the HHG spectra and its polarization state, including the underlying supercontinuum structure observed in the soft X-ray region in Fig. 4.2(c), we need to consider CPHHG phase-matched propagation as well as the ellipticity of the driving lasers. To achieve this, we simulated the macroscopic phase-matched buildup of a CPHHG field by computing 1D propagation through 2-mm He gas, using the EM field propagator [153] where the single-atom dipole acceleration is computed using the enhanced strong field approximation (SFA+) method [154], which has been validated against the time-dependent Schrödinger Equation (TDSE) simulations in the near-IR [154] and mid-IR regimes [155]. We account for the time-dependent ionized population using the instantaneous ADK rates [89, 156], and for reabsorption of the harmonics in the generating medium by using the Beer's law. The input laser field is modeled by a bi-chromatic elliptically-polarized laser pulse in the form of $E(t) = \sum_{i=1,2} \frac{A_i(t) E_i}{\sqrt{1+\epsilon_i^2}} [cos(\omega_i t)\hat{x} + \epsilon_i sin(\omega_i t)\hat{y}]$ where ϵ_i is the ellipticity. The driving laser frequencies, ω_1 and ω_2, correspond to wavelengths of $\lambda_1 = 0.79$ μm and $\lambda_2 = 1.3$ μm, respectively. The temporal envelope, $A_i(t)$, has a trapezoidal shape with 3 cycles of linear turn-on, 10 cycles of constant amplitude (43.3 fs), and 3 cycles of linear turn-off (in cycles of the 1.3-μm driving field).

Since perfect phase matching cannot be simultaneously achieved for left CP (LCP) and right CP (RCP) HHG [32], the simulations were performed at driving laser intensities of $I_1 = 2.40\times10^{14}\ W/cm^2$ and $I_2 = 2.20\times10^{14}\ W/cm^2$, chosen to fulfill the optimal phase-matching conditions, i.e. the sum of the phase mismatches for the two colors is zero slightly before the peak of the pulse, at an ionization level between the critical ionization for the two laser wavelengths [5]. This choice also yields good agreement between the experimental and theoretical HHG spectra. In Fig. 4.7, I present 1D propagation simulations for bi-chromatic 0.79-μm and 1.3-μm drivers, propagating through 2-mm He at pressures of 100 Torr (a) and 300 Torr (c). For 300 Torr of He, a Gaussian mask in the temporal domain of 3 cycles FWHM is used after performing longitudinal propagation to further remove the non-phase-matched HHG radiation, reproducing the effect of transversal phase-matching.

From Fig. 4.7(d), it is clear that at higher gas pressures, the temporal window for bright harmonic emission is considerably narrower than at lower gas pressures (Fig. 4.7(b)). As a consequence, the harmonic bandwidths broaden in the spectral domain. On the other hand, in Fig. 4.7(d), the HHG emission still contains several bursts, enabling the differentiation of LCP and RCP harmonics in the spectrum. If the temporal window was narrower, spectral overlap between LCP and RCP harmonics might occur. And if the window narrowed further allowing only a single burst, an isolated LP pulse or a CP pulse (a LP supercontinuum or a CP supercontinuum in the spectral domain) would be obtained if harmonics from both polarization states or from just one polarization state are selected, respectively.

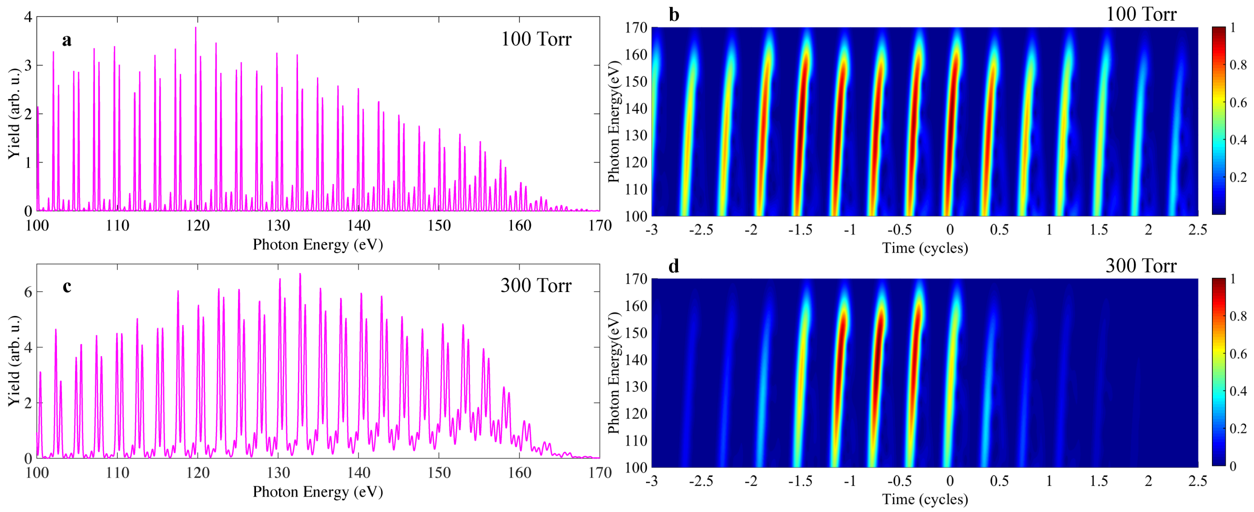

Figure 4.7: Simulated HHG spectrum from He at pressures of 100 Torr (a) and 300 Torr (c), as well as the corresponding time-frequency analysis (b, d) for counter-rotating driving wavelengths of 0.79 μm and 1.3 μm and ellipticities $\epsilon_1 = -0.985, \epsilon_2 = 0.985$. When the pressure is increased, the phase-matching window is shortened, so the number of attosecond pulses emitted is reduced, and consequently, the harmonic bandwidth in (c) is broadened. The time-frequency analysis is performed for the LCP harmonics. RCP harmonics exhibit very similar structure. From the strong peaks in (b) and (d), it is clear that short trajectories make the dominant contributions.

In Fig. 4.8(a) (cyan curve), I present the propagated HHG spectrum for counter-rotating CP driving laser fields with perfect circularity ($\epsilon_1 = -1, \epsilon_2 = 1$) through 2-mm He at a pressure of 400 Torr. However, the presence of small side-peaks adjacent to the main peaks in Fig. 4.2(b) and (c) provides a clue that additional channels are opening up, which can be explained using a simple photon model [31, 52, 53]. In the presence of a slight ellipticity in one or both of the driving lasers, photons of the wrong helicity may be absorbed, leading to small peaks with different helicities underlying and surrounding each main peak, which will be discussed in detail in the next section. This simple photon model can be used to explain the experimentally observed spectrum and also allows the ellipticity of the HHG spectrum to be extracted. The circularity of the HHG reduces from ~1 in the EUV to ~0.6 in the soft X-ray region (Fig. 4.10). However, each HHG peak will be perfectly CP if the driving lasers are perfectly CP.

In order to reproduce the underlying supercontinuum structure in the advanced macroscopic propagation simulations, we introduce a slight ellipticity into the driving laser pulses ($\epsilon_1 = -0.985, \epsilon_2 = 0.985$) in Fig. 4.8(a) (magenta curve), which can be expected because of the finite bandwidth of zero-order wave plates. New low-intensity harmonic peaks appear because additional new channels are allowed [31, 52, 53], which when combined with peak broadening that results from a short temporal phase-matching window, can reproduce the supercontinuum structure, in excellent agreement with experiment.

In Fig. 4.8(b), I present the predicted HHG emission in the temporal domain obtained by performing a Fourier transform of the magenta spectrum shown in Fig. 4.8(a). The attosecond pulse train has circular polarization when either left or right CPHHG orders are considered separately [49, 50]. When all HHG orders (left and right circular) are combined, a LP attosecond pulse train is generated, with subsequent bursts oriented in different directions and separated by (13/8) fs or 1.63 fs (since there are 8 bursts each 13 fs). Similar to the case for soft X-ray HHG driven by LP mid-IR driving lasers, soft X-ray CPHHG optimally phase matches [27, 75] (i.e. is brightest at the highest photon energies) at high gas pressures. Figures 4.8(b) and 4.7 show that for these pressures and wavelengths, the temporal window for bright phase-matched HHG emission is considerably narrower than at shorter laser wavelengths [75]. As a consequence, only five bright attosecond bursts are emitted, and the harmonic peaks broaden in the spectral domain. If the phase-matching window closes further, an isolated LP pulse or a CP pulse would be obtained if harmonics from both polarization states or from just one polarization state are selected, respectively. In comparison, when HHG is driven by LP mid-IR lasers, phase matching can isolate a single attosecond burst, and a supercontinuum of LP HHG is obtained [75].

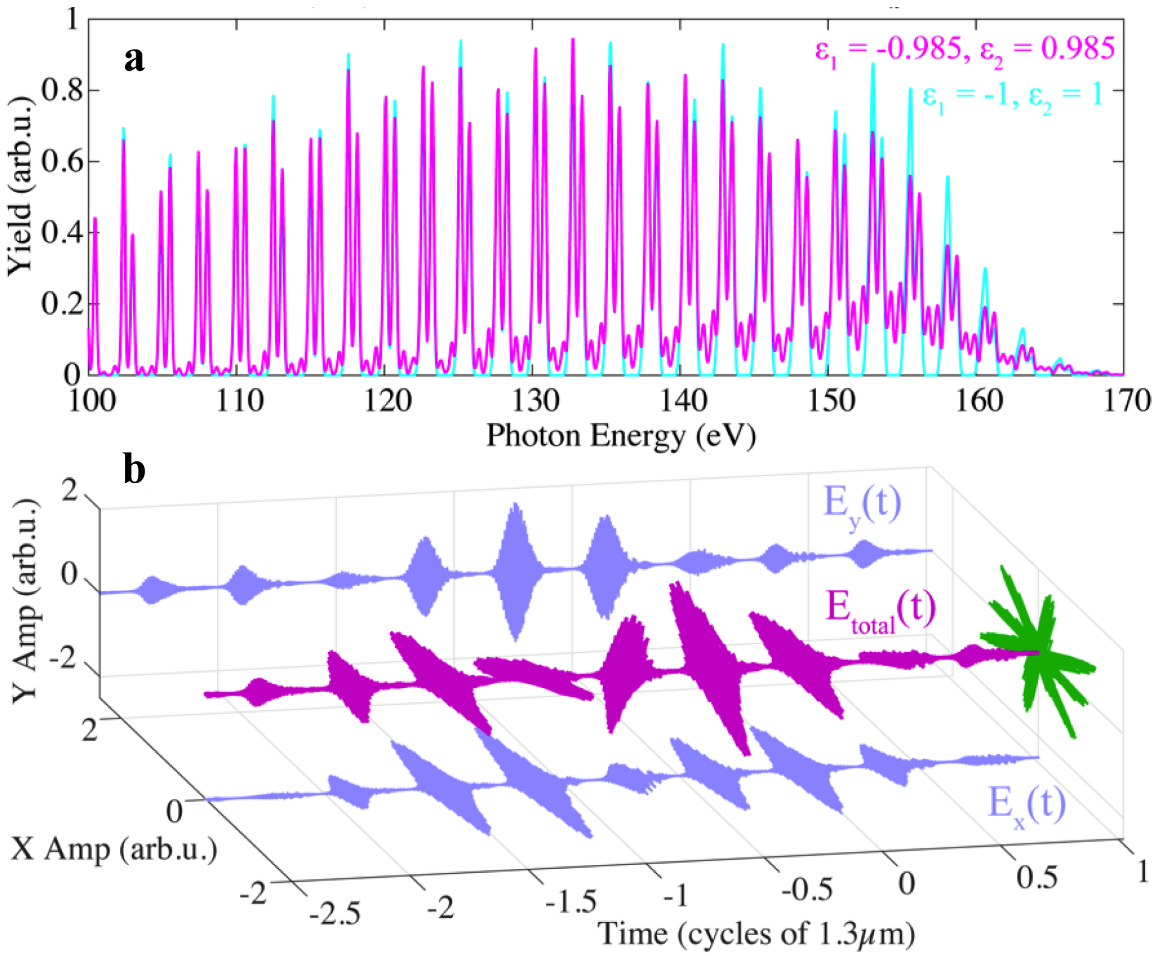

Figure 4.8: 1D propagation simulations of soft X-ray CPHHG from He. (a) Simulated HHG spectra after macroscopic propagation for counter-rotating CP laser drivers with perfect circularity ($\epsilon_1 = -1, \epsilon_2 = 1$, cyan) and slight ellipticity ($\epsilon_1 = -0.985, \epsilon_2 = 0.985$, magenta). Additional peaks appear when a slight ellipticity

is introduced. (b) Attosecond pulse trains ($E_x(t)$, $E_y(t)$, and $E_{total}(t)$) obtained by performing a Fourier transform of the magenta spectrum in (a), shows a short phase matching temporal window limits bright HHG to 5 attosecond bursts, with 2.6 LP bursts per 1.3-µm cycle.

4.2.3 Polarization analysis

In this section, I present an intuitive picture for the generation of additional peaks underlying and surrounding the main harmonic peaks resulting from imperfect circularity of the driving lasers [31, 52, 53]. We can describe these channels using a simple photon model [52], where we can imagine that the HHG process is drawing photons randomly from each driving laser beam, consistent with the conservation laws. CPHHG then corresponds to pulling all of the “correct” helicity photons from each beam, where we use “correct” to refer to getting all RCP photons from the RCP beam and all LCP photons from the LCP beam. We can think about the ellipticity of the beam as simply having a few of the “wrong” photons in each beam, where “wrong” means LCP photons in the RCP beam, and RCP photons in the LCP beam. When both of the driving lasers are perfectly CP, zero wrong photons are absorbed for CPHHG, as shown in Fig. 4.9(b) and the corresponding circles in Fig. 4.9(a). When the driving lasers have slight ellipticity, it is possible to absorb one wrong photon as shown in Figs. 4.9(c,d) and the corresponding squares in Fig. 4.9(a), two wrong photons as shown in Figs. 4.9(e-g) and the corresponding crosses in Fig. 4.9(a), and more than two wrong photons - which are not illustrated in Fig. 4.9 due to their low probability.

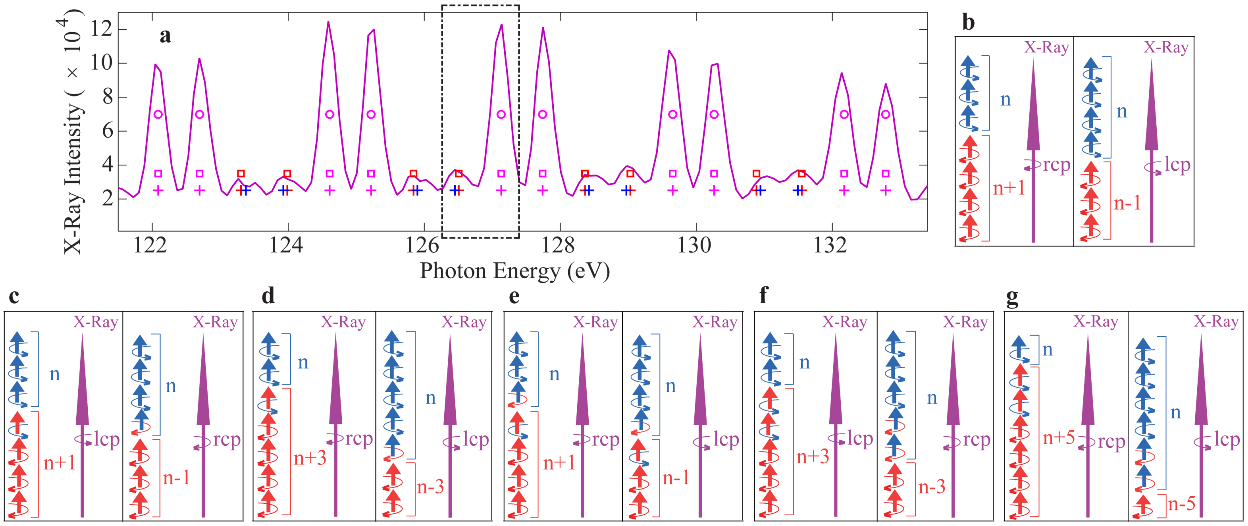

Figure 4.9: (a) Magenta curve: experimental CPHHG spectrum from He. Circles: channels when zero wrong photons are absorbed. Squares: channels when one wrong photon is absorbed. Crosses: channels when two wrong photons are absorbed. (b) With perfectly CP driving beams, zero wrong photons are absorbed, and only the l = n ± 1 channels are allowed. (c-g) With slightly elliptically polarized laser drivers, one (c, d) and two (e-f) wrong photons can be absorbed, (c, e) l = n ± 1; (d, f) l = n ± 3; (g) l = n ± 5, where n and l are the number of photons of 0.79 μm and 1.3 μm used to generate a CP HHG photon. The side peaks of the HHG spectrum match well with the predicted positions of these new channels, validating this analysis.

Conservation of energy and spin angular momentum gives $\omega_c = n\omega_1 + l\omega_2 = n\omega_1 + (n \pm 1)\omega_2$, for the circular harmonic of frequency ω_c generated from n photons of frequency ω_1 and l photons of frequency ω_2, where l = n ± 1 is required by photon spin angular momentum conservation when the driving fields are perfectly CP. When the driving laser field is not perfectly CP, additional channels, such as l = n ± 1 with one or more wrong photons absorbed, l = n ± 3 and l = n ± 5 etc. are allowed

[31, 52, 53], as illustrated in Figs. 4.9(c-g). Since Figs. 4.9(c,e) correspond to l = n ± 1 channels, these also appear at the same positions as the main peaks, as shown by the magenta squares and crosses in Fig. 4.9(a). Figures 4.9(d,f) correspond to l = n ± 3 channels, while g corresponds to l = n ± 5 channels – which are distinct from the main peaks (and marked as red squares and crosses and blue crosses in Fig. 4.9(a)). We find excellent agreement between the positions of these new channels predicted by this simple analysis and their location in the experimental HHG spectrum (Fig. 4.9(a)), confirming that these additional channels appear due to a slight ellipticity of the driving fields.

Since each beam is composed of a mixture of correct and wrong photons, with a fraction of correct photons p_i and a fraction of wrong photons $1 - p_i$ (here i = 1, 2 for the two drivers). Then, I can calculate the probability of each channel, i.e. the probability of absorbing n_i total photons from each beam with k_i wrong photons using the binomial distribution:

$$f(k_1, k_2;\, n_1, n_2, p_1, p_2) = \prod_{i=1}^{2} \binom{n_i}{k_i} {p_i}^{n_i - k_i} (1 - p_i)^{k_i} \tag{4.5}$$

for $k_i = 0, 1, 2, \ldots, n_i$, where $\binom{\boldsymbol{n_i}}{\boldsymbol{k_i}} = \frac{\boldsymbol{n_i}!}{\boldsymbol{k_i}!(\boldsymbol{n_i}-\boldsymbol{k_i})!}$. From this equation, we see that when the driver has very slight ellipticity, the probability of absorbing one wrong photon is about one order of magnitude lower than the probability of absorbing zero wrong photons, while the probability of absorbing two wrong photons is about two orders of magnitude lower than the probability of absorbing zero wrong photons. The probability of absorbing more than two wrong photons is even smaller. However, when the driving lasers deviate more from perfect circularity, the probability of absorbing more than two wrong photons starts to play a more important role.

Regarding the helicity of the main and side peaks, taking the harmonics inside the black box in Fig. 4.9(a) as an example, the magenta circle is RCP, the magenta square is LCP (about one order lower intensity than the magenta circle), the magenta cross is RCP (two orders of magnitude lower in intensity than the magenta circle): thus the main peak is RCP. For the small side peak, the red square is RCP, the red and blue crosses are LCP (one order of magnitude lower in intensity than the red square): hence the side peak is RCP, which is the same helicity as its nearest main peak. This is also validated by the XMCD measurements, as shown in Fig. 4.11.

The ellipticity of CPHHG can be analyzed using two methods: the simple photon model described above and a more advanced numerical simulation. In the simple photon model [31, 52, 53], I assume the fraction of correct photons to be 99.8% for Fig. 4.10(a) and 99.5% for Fig. 4.10(b) for both driving beams and simulate every harmonic peak (including the additional channels allowed by the ellipticity of the drivers) with a Gaussian curve. For Fig. 4.10(a), I assume a fractional bandwidth (the bandwidth of a HHG peak divided by its peak photon energy) of 0.3/67 (i.e. a bandwidth of 0.3 eV at 67eV) for absorbing zero wrong photon channels and a bandwidth of 0.5 eV for absorbing one to five wrong photons channels. For Fig. 4.10(b), I assume a bandwidth of 0.32 eV for absorbing zero wrong photon channels and 0.55 eV for absorbing one to five wrong photons channels. These parameters are chosen to best fit the experimental data. Then I add all of the Gaussian curves together and multiply by an envelope (to account for gas absorption, filter transmission, and HHG cutoff etc.) to get a simulated HHG spectrum. We see that the simulated and experimental HHG spectra match very well, and that the HHG circularity reduces from ~1 in the extreme ultraviolet (EUV) to ~0.6 in the soft X-ray region.

It is straightforward to understand why the circularity of the harmonics reduces at higher photon energies. For low-order harmonics, we need to add fewer photons, which have a high probability of selecting all correct ones. However, for higher HHG orders, we need to combine more photons, which becomes more challenging to do without including some photons with the wrong helicity. For example, if I assume the fraction of correct photons in both driving laser beams to be 99.5%, the probability of selecting 20 correct photons is ≈ 90%. But if I select 100 photons, the probability of selecting them all correctly is only ≈ 61%. So, when I am generating higher order harmonics, the requirement for pure circular drivers becomes much stricter. For example, if I want the possibility of adding 1000 correct photons (which will reach the L-edges at around 700 eV with mid-IR drivers) to be 95%, then the driving laser beams need to consist of 99.995 photons with the correct helicity.

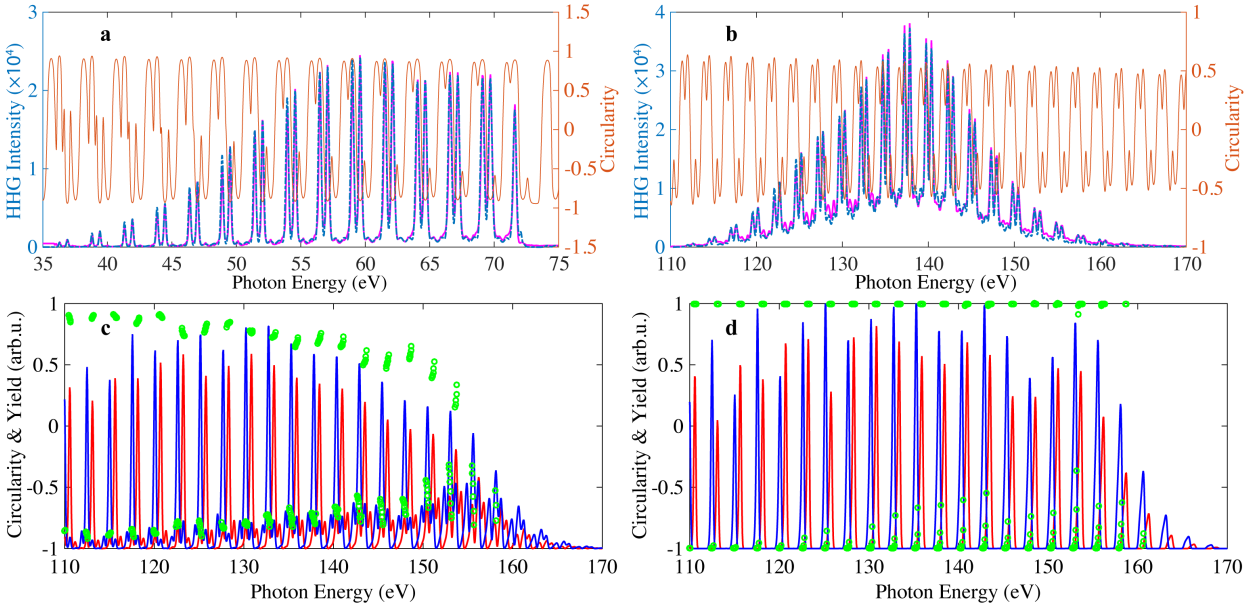

Figure 4.10: (a, b): Polarization analysis using the simple photon model for He phased matched at low gas pressure (510 Torr, EUV region) (a) and high gas pressure (970 Torr, soft X-ray region) (b). Magenta curves: experimental HHG spectra. Blue dashed curves: simulated HHG spectra using the simple photon model. Brown curves: circularity $((I_{RCP} - I_{LCP})/(I_{RCP} + I_{LCP}))$ of the HHG, which

decreases from ~1 in the EUV region (a) to ~0.6 in the soft X-ray region (b). (c, d): Polarization analysis of the simulated spectra presented in Fig. 3c when the drivers are slightly elliptical (c) and perfect CP (d). Red (blue) curves: RCP (LCP) components of the HHG spectra in Fig. 3(c). Green dots: circularity of the harmonics calculated from $(I_{RCP} - I_{LCP})/(I_{RCP} + I_{LCP})$.

Figures. 4.10(c,d) show a polarization analysis of the simulated spectra presented in Fig. 4.8(a), which include phase-matched propagation, for the case in which the drivers are slightly elliptical (c) and perfect CP (d). When the driving beams are slightly elliptically polarized, the HHG circularity gradually decreases at the peaks as the photon energy increases. However, when the driving lasers are perfectly CP, the HHG peaks have perfect circular polarization, which decreases as expected in regions where the peaks overlap.

Experimentally, I observe harmonic peaks sitting on top of a broad supercontinuum "baseline" in the CPHHG from Ne and He, which in fact can be completely described as the sum of the peaks of all the channels. As the phase-matching window closes, we are left with an attosecond pulse train consisting of fewer bursts as discussed in the last section, and the peaks become broader in the spectral domain. The merging of all those peaks in the wings leads to appearance of an underlying supercontinuum.

4.2.4 X-ray magnetic circular dichroism of Gd/Fe

Finally, we note that a unique aspect of CPHHG is its very high stability, as validated by the XMCD measurements shown in Fig. 4.12, since the shape of the combined driving laser field is largely insensitive to phase slip between the two driving lasers. Rather, the combined field will simply rotate [32]. This makes CPHHG highly stable - even if the two drivers are not phase locked - and thus very attractive for applications.

XMCD is helicity dependent absorption in magnetic materials. When the magnetization direction is fixed, the absorption coefficient of RCP and LCP beams is different. The same thing works when I fix the helicity of the beam and change the magnetization direction. XMCD measurements can serve both to spectrally characterize the polarization of a light source, and to make fundamental materials measurements. Here, I use an out-of-plane magnetized Gd/Fe multilayer sample to perform XMCD at the $N_{4,5}$ absorption edges of the rare-earth metal Gd around 145 eV, as well as at the Fe $M_{2,3}$ absorption edges around 54 eV. The observed magnetic contrast confirms that the soft X-ray HHG beams indeed exhibit circular polarization and are bright enough for applications.

As schematically depicted in Fig. 4.1, the Gd/Fe multilayer sample is surrounded by four permanent (NdFeB) magnets [41], which provide a magnetic field perpendicular to the sample. The four permanent magnets are mounted on a rotation stage such that their generated magnetic field could be applied perpendicular to the sample surface in either direction. The magnetic contrast is obtained by switching the magnetic field between parallel/antiparallel alignment relative to the HHG propagation vector. The external magnetic field $\mu_0 H$ at the sample was 230 mT, measured with a Hall probe – high enough to saturate the magnetization of the multilayer sample [157] as confirmed by vibrating sample magnetometry. The out-of-plane magnetized multilayer sample, which consists of 50 repetitions of Gd (0.45 nm)/Fe (0.41 nm) layer pairs, was deposited on a 50-nm silicon nitride membrane to enable a transmission geometry, and capped by 3-nm of Ta to prevent oxidation. For the XMCD measurements, I used the harmonics generated in He with 1.3-μm and 0.79-μm drivers, where the laser peak intensities and the gas pressure were optimized for phase matching at the higher and lower energy parts of the spectrum, corresponding to the Gd and Fe absorption edges, respectively (Figs. 4.2(a,c)). Since the phase mismatch becomes larger with broader bandwidth [32, 49], I was not able to phase match the entire spectrum at the same time. In addition, for Ar and He CPHHG spectra in Fig. 4.2(a,c) and the XMCD measurement in Fig. 4.11, the CCD used is Andor Newton DO940P-BN, for Ne CPHHG spectra in Fig. 4.2(b), the CCD used is Andor DO420-BN.

The transmitted intensity $\mathrm{I}^{\pm} = \mathrm{I}_0 \mathrm{e}^{-2\omega \mathrm{d} \mathrm{Im}(\mathrm{n}_{\pm})/\mathrm{c}}$ of a CPHHG beam with incident intensity I_0, through the sample with thickness d, was recorded with the magnetic field both parallel (I^{+}) and antiparallel (I^{-}) to the wave vector (k) of the X-rays with energy $\hbar\omega$. The refractive index is defined as $\mathrm{n}_{\pm} = 1 - (\delta \pm \Delta\delta) + \mathrm{i}(\beta \pm \Delta\beta)$, where β and $\Delta\beta$ are the absorptive index and its magneto-optical correction, respectively [158-160]. From $\mathrm{I}^{\pm}$ I obtain the XMCD asymmetry, defined as $\mathrm{A}_{\mathrm{XMCD}} = \frac{\mathrm{I}^{+} - \mathrm{I}^{-}}{\mathrm{I}^{+} + \mathrm{I}^{-}} = -\tanh(2\omega \mathrm{d} \Delta\beta/\mathrm{c})$, from which the magneto-optical (MO) absorption coefficient $\Delta\beta = \Re\left(\frac{\varepsilon_{xy}}{2\sqrt{\varepsilon_{xx}}}\right)$ is extracted and compared to previous synchrotron work [161-166], with ε_{ij} representing different components of the dielectric tensor. Note that the opposite sign of $\mathrm{A}_{\mathrm{XMCD}}$ for adjacent harmonics (Fig. 4.11) demonstrates that they have opposite helicities.

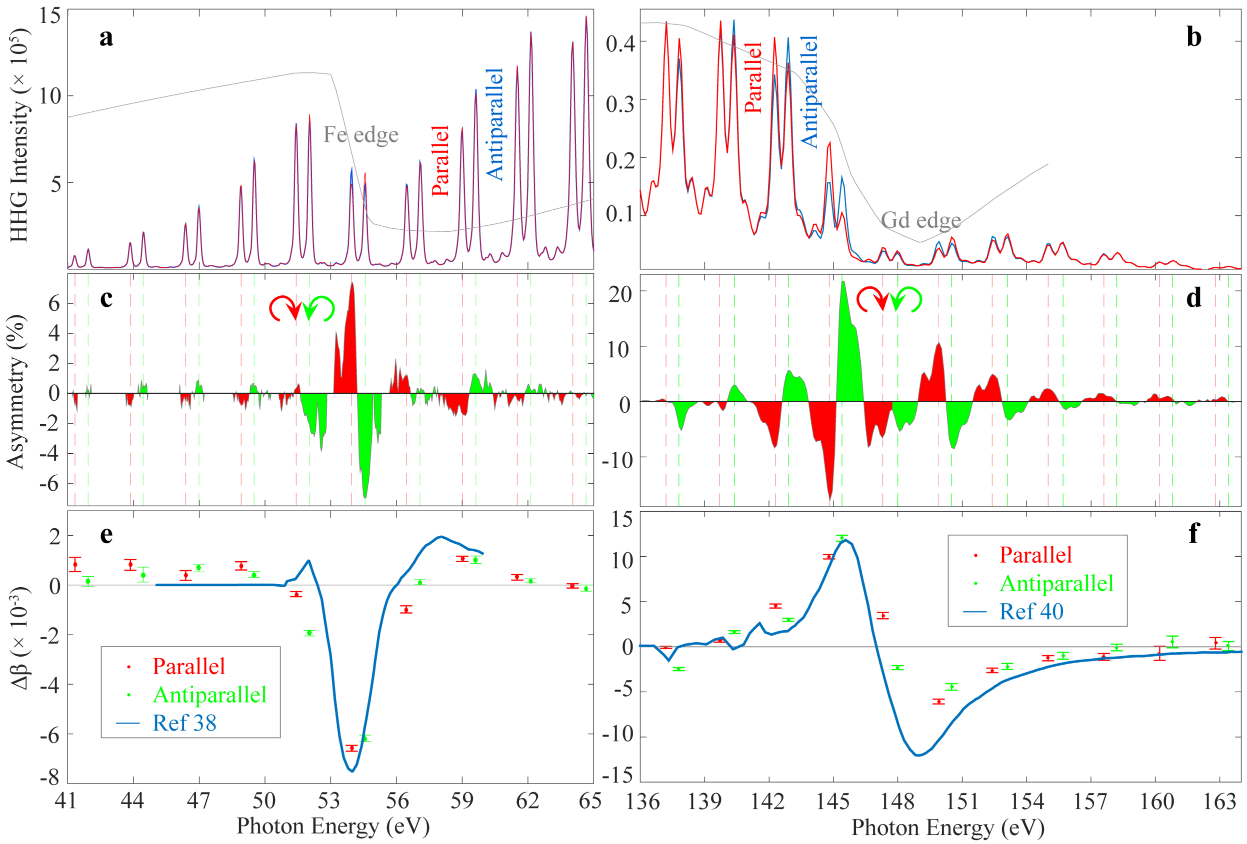

Figure 4.11: EUV and X-ray magnetic circular dichroism of Fe and Gd. (a, b) HHG spectra around the Fe $M_{2,3}$ and Gd $N_{4,5}$ edges, transmitted through a Gd/Fe multilayer as the magnetization direction is parallel (red) and antiparallel (blue) to the HHG propagation direction. Gray lines: transmission of Fe and Gd. (c, d): XMCD asymmetry of Fe and Gd, with opposite signs for left (green) and right (red) CPHHG demonstrating opposite circularity of adjacent harmonics. (e, f): Extracted MO absorption coefficients at the Fe $M_{2,3}$ and the Gd $N_{4,5}$ edges (after correcting for ellipticity) agree well with literature values [161, 163, 164].

By analyzing the strong XMCD signal, I extracted the MO absorption constant across a broad photon energy range above and below the Gd and Fe edges. As can be seen from Fig. 4.11, the excellent agreement between the extracted magneto-optical absorption coefficients and previous work [161, 164] shows that HHG can be successfully used for tabletop XMCD. The MO constants of Fe and Gd around the absorption edges show opposite signs. Since $\Delta\beta$ has the same sign for both elements [161, 164], this indicates an anti-ferromagnetic alignment between Fe and Gd layers, as expected for these multilayers [167]. Moreover, the XMCD results show that the small side peaks, which result from the imperfect circularity of the driving fields, also exhibit a high degree of circularity with the same circular polarization as their nearest main harmonic peak. These results demonstrate the brightness, stability, and high degree of circularity of the generated harmonics, which extends element-specific and magnetic-sensitive ultrafast pump-probe capabilities into the soft X-ray range and to the 4f rare earth ferromagnets, with potential to reach the L shell absorption edges of many magnetic materials in the keV range in the near future [7].

In Fig. 4.12, I show the XMCD measurements of Gd obtained by taking a 2 min single spectrum when the magnetization of the sample is parallel/antiparallel (I^+/I^-) with the HHG propagation direction. The excellent data quality of this single spectrum XMCD demonstrates the brightness of this CPHHG source. Note that the XMCD data shown in Fig. 4.11 was obtained by averaging 300 spectra, with a 40 second exposure time each. In my experimental setup the acquisition time of a XMCD spectrum was limited by the speed of the rotational stage that the permanent magnets are mounted on (it takes around 20 s to rotate from parallel to antiparallel). Thus, that experiment took 600 min in total and I get excellent statistics, which strongly demonstrate the stability of this CPHHG source. The fact that I can achieve good data over total exposure times from 4 minutes to 600 minutes demonstrates that this CPHHG source can be utilized in a pump-probe magnetization dynamics measurement.

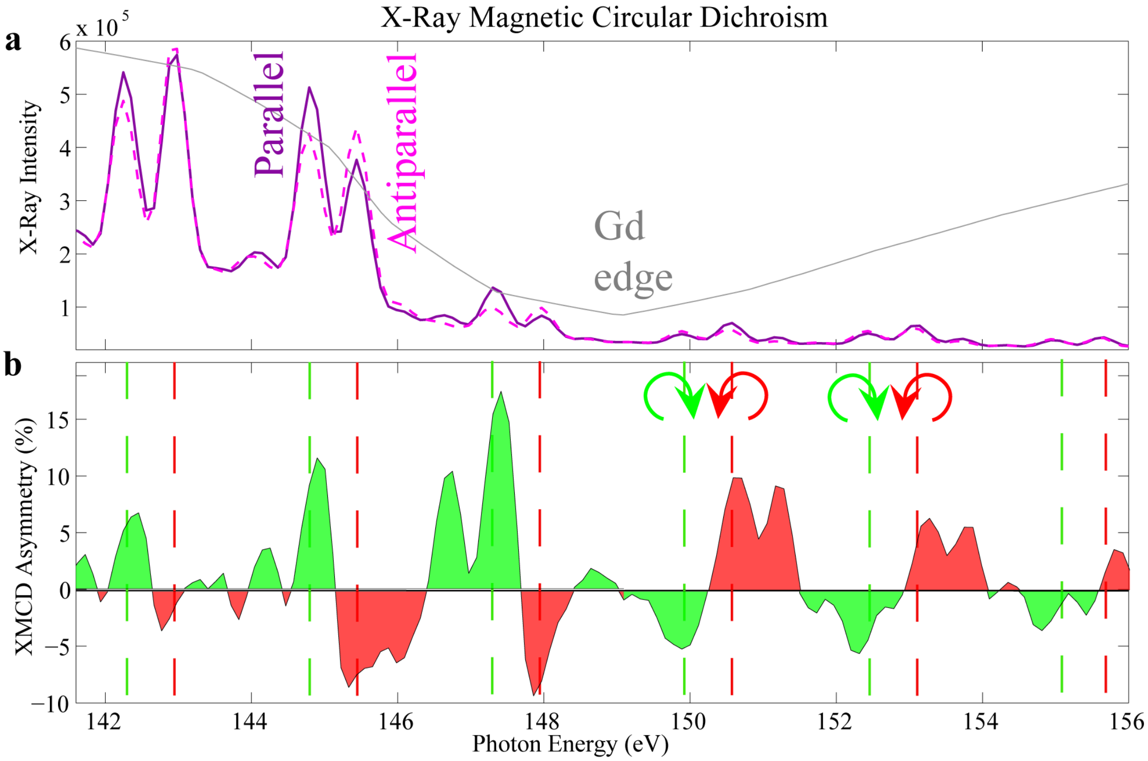

Figure 4.12: 4 min XMCD of Gd. (a): HHG spectra around the Gd $N_{4,5}$ edges, transmitted through a Gd/Fe multilayer as the magnetization direction is parallel (red) and antiparallel (blue) to the HHG propagation direction. The gray lines show the Gd absorption edge. (b): XMCD asymmetry of Gd obtained by taking a 2-min single spectrum when the magnetization is parallel/antiparallel to the HHG propagation direction [145].

Finally, I compare the magneto-optical (MO) constants extracted from the HHG XMCD measurement with literature values for Gd, in particular from Prieto et al. 2002 [164]. Note that the previous measurements had to be scaled for several reasons. Prieto et al. used a photocurrent method, and calibrated their absorption coefficient at two energy positions far away from the Gd edges using data from Henke et al. [168]. Prieto et al. found that the absorption coefficient of Gd $N_{4,5}$ is around 3 times higher than expected [164]. To account for this, in Fig. 4.13, I divide the absorption coefficient from Prieto et al. by a factor of 3.5, and the absorption coefficient from my experiment agrees very well with both the data from Prieto et al. and Henke et al. [168]. Since the MO constant is proportional to the absorption coefficient, the MO constant from Prieto et al. also needs to be divided by 3.5. Moreover, their definition of the MO constant is 2 times larger than the definition I use, so the MO constant from Prieto et al. is divided by a factor of 3.5×2 = 7 to be comparable with my data. Finally note that since the soft X-ray CPHHG are elliptically polarized, with ~0.6 degree of circular polarization, this is taken into account in extracting an accurate MO constant. After appropriate scaling and correcting for the degree of polarization, we see that the MO constants extracted from our data are in very good agreement with previous measurements, as shown in Fig. 4.11.

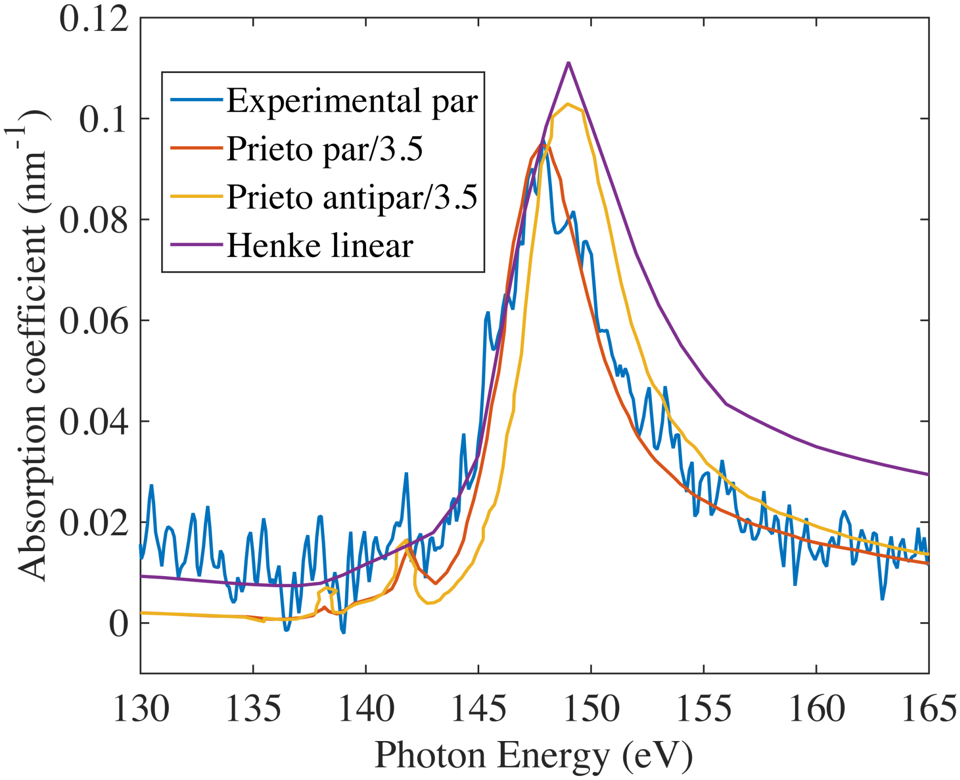

Figure 4.13: The absorption coefficient I measured (blue, unaveraged single spectrum data) agrees very well with the absorption coefficient from Henke et al. (purple) [168], and Prieto et al. after appropriate scaling (brown, yellow) [163, 164].

4.2.5 Flux characterization

In this section, the CPHHG photon flux was characterized for Ar, Ne, and He driven by two-color counter-rotating CP drivers 0.79 μm and 1.3 μm at a repetition of 1kHz. I start from the CCD recorded spectra, from which I can write the HHG spectra in counts per second. Then I find the electrons per count, photons per electrons, and quantum efficiency (QE) from the specifications of the CCD I used (for Ar and He, the CCD used is Andor Newton DO940P-BN, for Ne, the CCD used is Andor DO420-BN). The HHG beam also propagates through thin-film filters and a spectrometer. Thus, the final HHG flux in photons/s shown in Fig. 4.14 are obtained from: HHG spectrum from CCD with (counts/s) × (electrons/count) × (photons/electron) / QE / filter transmission / spectrometer efficiency.

For Ar, electrons/count = 12.5, photons/electron ≈ 1/11, QE ≈ 30%, two 200-nm aluminum filters (with transmission efficiency ≈ 20% after accounting for 20-nm oxidation on both sides) are used, spectrometer efficiency ≈ 1%.

For Ne, electrons/count = 7, photons/electron ≈ 1/26, QE ≈ 70%, two 200-nm zirconium filters (with transmission efficiency ≈ 40% after accounting for 20-nm oxidation on both sides) are used, spectrometer efficiency ≈ 0.1%.

For He, electrons/count = 12.5, photons/electron ≈ 1/30, QE ≈ 25%, one 200-nm aluminum filter (with transmission efficiency ≈ 40% after accounting for 20-nm oxidation on both sides) and one 200-nm silver filter (with transmission efficiency ≈ 10% after accounting for 20-nm oxidation on both sides) are used, spectrometer efficiency ≈ 0.1%. As shown in Fig. 4.14, the photon flux of CPHHG is about 10^9 photons/s/pixel, which is about 10^7 photons/pulse/1% bandwidth. This photon flux is comparable to LPHHG driven by a single LP laser beam as shown in Fig. 2.11.

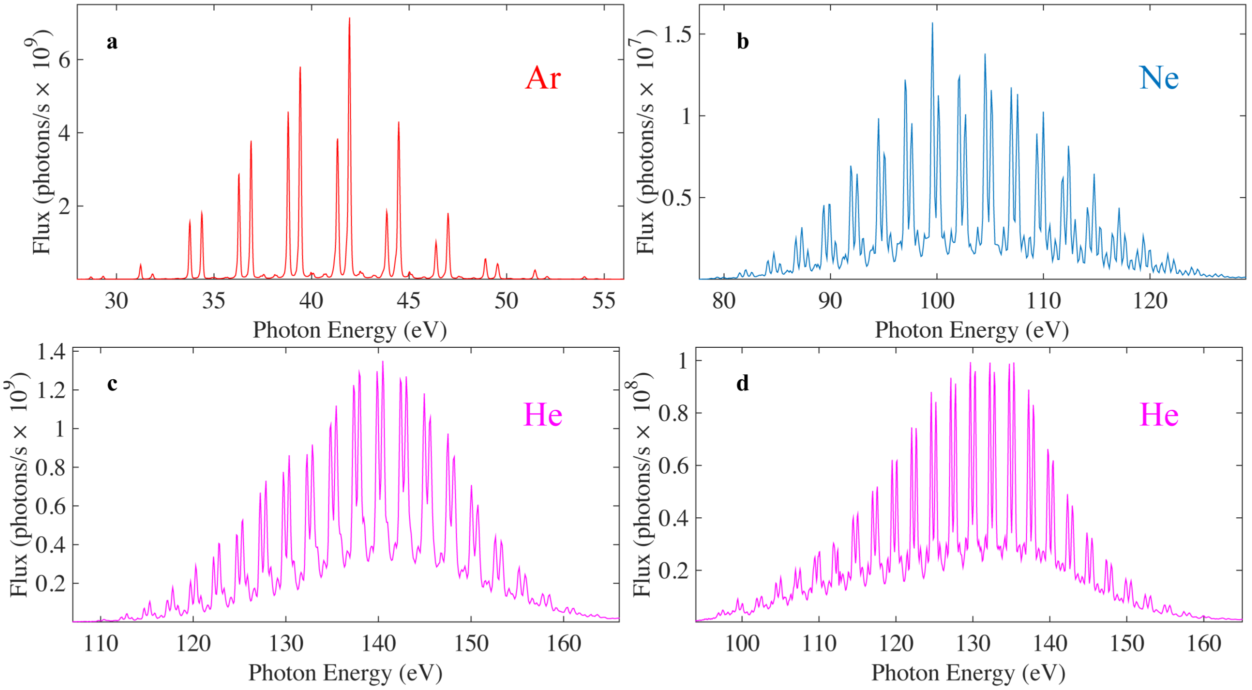

Figure 4.14: Experimental CPHHG flux for Ar (a), Ne (b), and He (c, d). Note that the driving bi-chromatic laser field intensity used in (c) is higher than in (d), which leads to a higher flux in (c) than in (d). However, since the phase-matching window in (c) is shorter than in (d), the harmonics of the former spectrum are broader and merge stronger than in the latter case.

4.3 Circularly polarized high harmonics by 2 μm + 0.79 μm

In this section, I will show bright phase-matched CPHHG generated by using collinearly propagated two-color counter-rotating CP beams, for the first time, with wavelengths of 2 μm and 0.79 μm, which extend phased-matched CPHHG to a broader wavelength combination and further confirmed the universal nature of this generation scheme. Conservation laws determine the harmonic spectra exhibit pairs of harmonics with opposite helicities and all the harmonics are close to evenly spaced. Besides, by analyzing the helicity dependent intensity asymmetry of

CPHHG driven by different wavelengths from different gas targets, I will show that the helicity dependent intensity asymmetry is mostly a result of the helicity dependent single-atom physics [50, 51, 149], which exhibits different behaviors for different gas targets. What's more, this asymmetry can reverse and very interestingly, CPHHG generated from Ar exhibits a single helicity for the high-photon-energy region of the spectrum, which provides a convenient way to generate CPHHG with a single helicity and CP attosecond pulse trains.

At the end of this section, I will show simulations of the main harmonics and the additional channels allowed by the imperfect circularity of the driving beams, which provide guidance for choosing the wavelengths of the two beams to generate CPHHG and for achieving CPHHG at higher photon energies. Finally I will show that the cutoff energy of CPHHG generally falls between the cutoff energies (or the phase-matching cutoff energies) of LPHHG of the two driving beams, and is much closer to the phase-matching cutoff energy of LPHHG driven by the shorter-wavelength beam. What's more, I will show the cutoff energy of CPHHG can be greatly increased by increasing the ionization potential of the gas target and by increasing the wavelength of the shorter-wavelength beam.

In my experiment, the output of a single-stage 8.4-mJ/pulse Ti:sapphire regenerative amplifier at 1 kHz with a pulse duration of 45 fs and a central wavelength of 0.79 μm [115] is split into two arms, one arm with 85% of the output energy (7 mJ/pulse) is directed into a three-stage OPA. The OPA converts its input energy into a 1.7-mJ/pulse signal beam with a central wavelength of 1.3 μm and a 0.9-mJ/pulse idler beam with a central wavelength of 2 μm. As Fig. 4.15(a) shows this idler beam and the other 0.79-μm arm are then focused, by lens with a focal length of 20 cm and 50 cm, respectively, collinearly into a hollow-core waveguide filled with noble gas. The waveguide has a length of 1 cm and an inner diameter of 150 μm. The energy of the 0.79-μm and 2-μm beams coupled through the fiber can be adjusted by an iris in each arm and are 0.9 mJ/pulse and 0.4 mJ/pulse, respectively when the irises are fully open. After the fiber, the two driving laser beams are blocked by thin film filters (Al filter for Xe and Ar, Zr filter for Ne), while the harmonic beam passes through the filters and travels through an X-ray spectrometer, finally its spectrum is recorded by an X-ray camera.

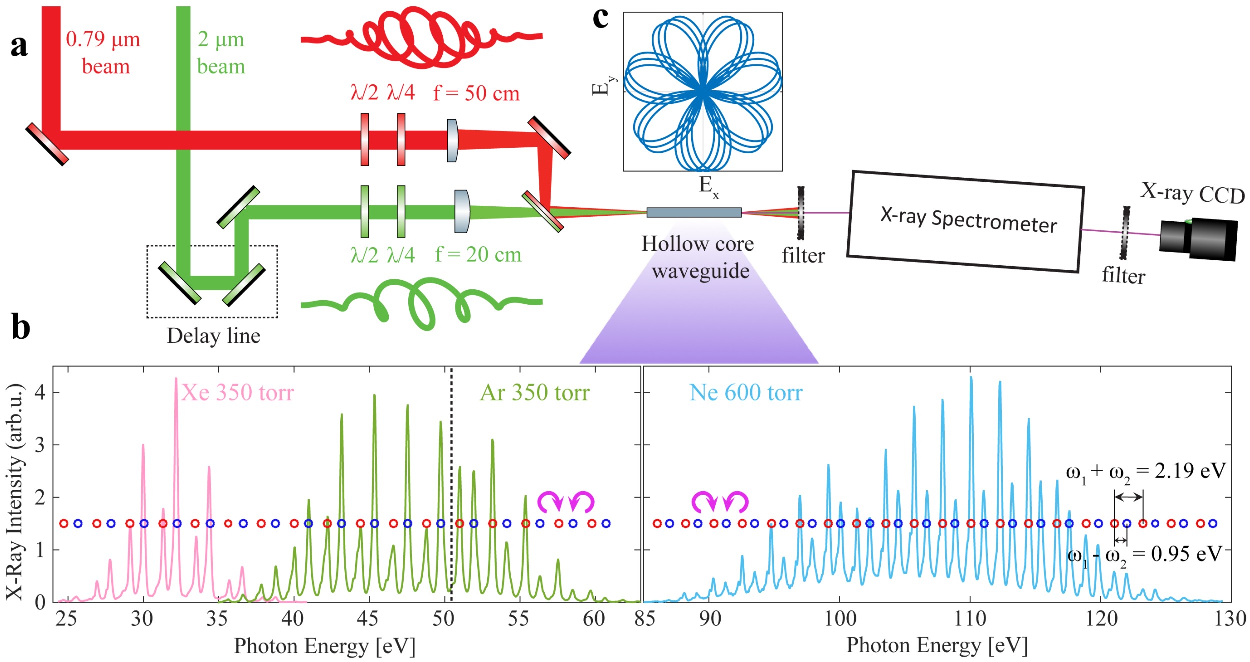

Figure 4.15: CPHHG driven by 2 μm and 0.79 μm. (a) Experimental setup. 2-μm and 0.79-μm beams are focused collinearly into a hollow-core waveguide filled with noble gas. A pair of half and quarter waveplates in each arm are used to convert the polarization of the two arms from linear to counter-rotating circular. Then the generated harmonic beam goes through an X-ray spectrometer and is recorded by an X-ray camera. (b) Experimental spectra generated from Xe, Ar, and Ne match perfectly with harmonics position (blue and red circles) predicted by energy, parity, and spin conversation laws. Harmonics at the position of red (blue) circles co-rotating with the 2-μm (0.79-μm) beam. The black dotted line shows position where

the helicity dependent intensity asymmetry reverses. (c) Combined electric field of the two colors has many sets of seven lobes, the following set of lobes does not repeat the previous ones and have a slight rotation compared to the previous set of lobes.

As discussed in the last section, harmonic spectra generated using two-color counter-rotating CP fields follow energy, parity, and spin conservation laws [31-33, 52, 53]. From conservation laws the spectra exhibit pairs of left and right CPHHG with a photon energy difference of $\omega_1 - \omega_2$ between the harmonics within each pair, and $\omega_1 + \omega_2$ between adjacent pairs, where ω_1 and ω_2 are the photon energies of the two driving laser beams. Here $\omega_1 = 1.57$ eV, $\omega_2 = 0.62$ eV, so the harmonics within each pair are separated by 0.95 eV, and adjacent harmonic pairs are separated by 2.19 eV. As Fig. 4.15(b) shows the experimental spectra exhibit pairs of harmonics with opposite helicities and the harmonics are close to evenly spaced as determined by conservation laws. The first harmonic (red circles) within each pair co-rotates with the 2-μm beam, while the second harmonic (blue circles) within each pair co-rotates with the 0.79-μm beam. The experimental spectra match perfectly with harmonic positions (red and blue circles in Fig. 4.15(b)) predicted by conservation laws. What's more, the spectra show an underlying supercontinuum, which is very subtle in Xe and Ar, and very obvious in Ne. As explained in the last section, two effects lead to the underlying supercontinuum, on one hand, experimentally the driving laser fields are not perfectly CP, this imperfect circular polarization results in new generation channels that generate additional harmonic peaks surrounding and underlying the main harmonics. On the other hand, the short temporal phase-matching window causes the broadening of each harmonic peak. These two effects lead to the merging of harmonics at the bottom of the spectra and the appearance of an underlying supercontinuum.

4.3.1 Helicity dependent intensity asymmetry

Another interesting feature of the spectra is the intensity of the two harmonics within each pair shows a big asymmetry. As Fig. 4.15(b) shows, for CPHHG from Xe, the second peak within each pair has a much stronger intensity. For CPHHG from Ar, the second peak within each pair is stronger for low-photon-energy harmonics, then the asymmetry reverses at around 51 eV and the first peak becomes stronger for high-photon-energy harmonics. For CPHHG from Ne, the first peak within each pair is always stronger. Figure 4.16(a) shows the calculated intensity asymmetry of the spectra shown in Fig. 4.15(b) and in Fig 4.2 (CPHHG driven by 1.3 μm + 0.79 μm from Ar, Ne, and He). The value of the intensity asymmetry ranges from -1 to 1. When the intensity of the first peak (second peak) is zero, the intensity asymmetry equals -1 (1), and when the two peaks have the same intensity, the intensity asymmetry equals zero. As Fig. 4.16(a) shows, CPHHG from Xe and Ar have relatively bigger intensity asymmetries, CPHHG from Ne have relatively smaller intensity asymmetries, while the intensity asymmetries of CPHHG from He are almost zero.

There are many studies investigating the reasons of the intensity asymmetry of the two helicities within each harmonic pair. Reference [54] shows that helicity dependent phase matching facilitates the generation of high harmonic beams with a high intensity asymmetry. Reference [50, 51, 149] show that the single-atom physics of this generation scheme is helicity dependent, and CPHHG generated using this scheme is sensitive to the angular momentum of the initial state. When the initial state is s ground state (like He), the intensity of the two harmonics within each pair are almost the same, while when the initial state is p ground state (like Xe, Ar, and Ne), high harmonics with opposite helicities have very different intensities. The results in Fig. 4.16(a) match well with the single-atom physics and it is convincing to believe that the helicity dependent single-atom physics, which shows very different behaviors for different gas target, greatly affect the experimentally observed helicity dependent intensity asymmetry of CPHHG.

Since the initial state of He has only the s ground state, so CPHHG from He does not exhibit single-atom helicity dependence, thus the intensity asymmetry of CPHHG from He comes from helicity dependent phase matching, which is super smaller since the intensity asymmetry of He is almost zero. Reference [55] states that the intensity asymmetry between the two helicities within each pair can be modified by controlling the intensity ratio between the two driving beams, for the data set used in Fig. 4.16(a), the intensity of the driving beams with longer wavelength (I_r) and shorter wavelength (I_b) satisfies the equation $0.5 < I_r / I_b < 1.5$, so the effect caused by the intensity ratio between the two driving beams is very small here.

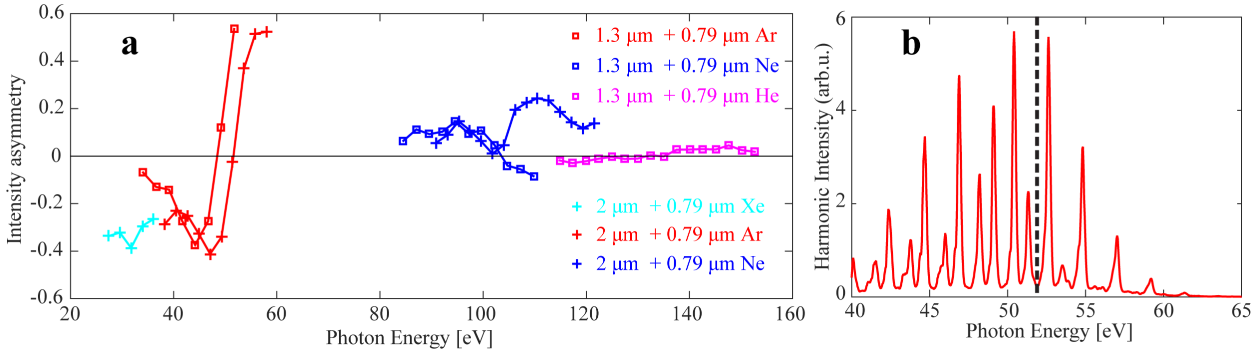

Figure 4.16: (a) Intensity asymmetry of the two harmonics within each pair calculated by Asymmetry = $(S_r - S_b)/(S_r + S_b)$ for CPHHG driven by 1.3 μm + 0.79 μm from Ar, Ne, and He, and driven by 2 μm + 0.79 μm from Xe, Ar, and Ne. Here S_r

(S_b) is the intensity of the first (second) peak within each pair, which co-rotates with the longer-wavelength (shorter-wavelength) driving beam, calculated by integrating over the harmonic from tail to tail. The x-axis is the average photon energy of the two peaks. Since the first peak has a photon energy of $n\omega_1 + (n + 1)\omega_2$, the second peak has a photon energy of $(n + 1)\omega_1 + n\omega_2$, the average photon energy of the two peaks is $(n + ½) (\omega_1 + \omega_2)$, where n is a positive integer. (b) CPHHG spectrum driven by 2 μm + 0.79 μm laser beams from Ar, which shows a big intensity asymmetry and exhibits a single helicity at the high-photon-energy region (above the photon energy indicated by the dashed line) of the spectrum.

The harmonic pairs not only have strong helicity dependent intensity asymmetry, this intensity asymmetry also reverses. As shown in Fig. 4.15(b) and Fig. 4.16(a), the intensity asymmetry reverses in harmonics generated from Ar and Ne. This behavior can be explained within single-atom picture as in reference [50, 51, 149]. However, it is still in doubt about the exact mechanism causing the intensity asymmetry reversion. Very interestingly, Fig. 4.16(b) shows CPHHG exhibit a single helicity at the high-photon-energy part of the spectrum, where the harmonic intensity of one of the two helicities is almost zero or zero. This provides a convenient way to generate CPHHG with a single helicity and CP attosecond pulse train.

4.3.2 Cutoff of circularly polarized high harmonics

In order to provide guidance about the photon energies obtained by using driving beams with different wavelengths from different gas targets, here I analyze the experimental cutoff energies of CPHHG. Figure 4.17(a) shows the comparison of

CPHHG cutoff energy with LPHHG cutoff energies of the two driving beams. Experimentally, CPHHG cutoff energy is first obtained, then keep everything the same, block beam one (two) and rotate the quarter wavelength of beam two (one) to maximize the HHG flux (change the polarization of beam two (one) from circular to linear) to obtain the LPHHG cutoff energy of beam two (one). The intensity ratio of the longer-wavelength driving beam to the shorter-wavelength driving beam is bigger than 0.5 and smaller than 1.5. We see within this intensity ratio, the CPHHG cutoff energy falls between the two LPHHG cutoff energies, and is much closer to the shorter-wavelength driven LPHHG cutoff energy.

Since the intensity of the two driving beams and the gas pressure used in Fig. 4.17(a) are adjusted to optimize the flux and cutoff energy of CPHHG, so the intensity and gas pressure are not optimized for full phase matching of LPHHG. Thus, the LPHHG cutoff energies in Fig. 4.17(a) are not full phase-matching LPHHG cutoff energies. In Fig. 4.17(b) the CPHHG cutoff energy is compared with the full phase-matching LPHHG cutoff energies, which are captured from Ref. [102]. We see that the CPHHG cutoff energy in general falls between the two LPHHG phase-matching cutoff energies, and is way closer to the phase-matching cutoff energy of the shorter wavelength.

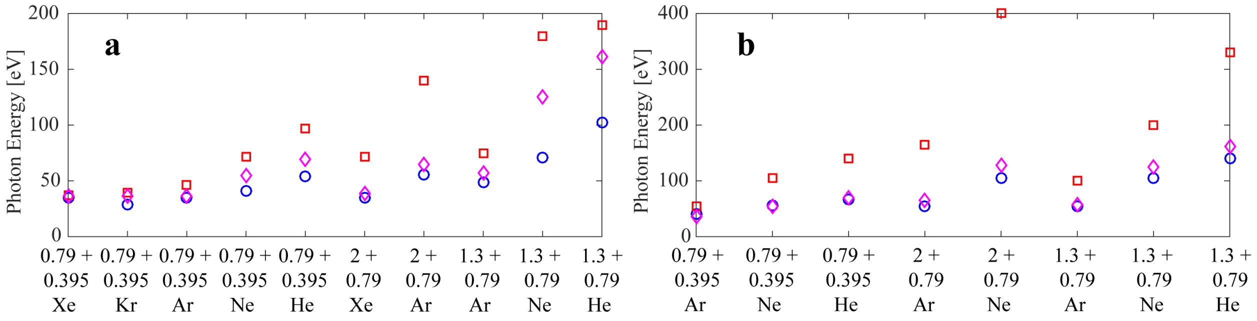

Figure 4.17: (a) Experimental CPHHG cutoff energy (magenta diamonds), compared with the LPHHG cutoff energies of the longer-wavelength driving beam (red

squares) and the shorter-wavelength driving beam (blue circles). (b) Experimental CPHHG cutoff energy (magenta diamonds), compared with the phase-matching cutoff energies of LPHHG driven by the longer-wavelength beam (red squares) and the shorter-wavelength beam (blue circles), which are captured from Ref. [102]. The x-axis in (a) and (b) are the wavelengths of the two driving beams (in μm) and the gas target used.

The results in Fig. 4.17 indicate ways to generate CPHHG at higher photon energies. First, using gas target with higher ionization potential can dramatically increase the CPHHG cutoff, as evidenced by comparing the cutoff energies of CPHHG driven by the same laser wavelengths from different gas targets. Helium allows the highest CPHHG cutoff, then Ne, finally Ar. This is true for all the three wavelength combinations shown in Fig. 4.17. This behavior is similar to cutoff energy behaviors of LPHHG. Second, CPHHG at higher photon energies can be generated by using longer-wavelengths driving beams, and the cutoff has a much dramatic increase when the shorter wavelength of the two driving beams is increased, which is evidenced by two facts. First, for CPHHG from Ar, when the wavelengths of the driving beams change from 1.3 μm + 0.79 μm to 2 μm + 0.79 μm, the cutoff stays almost the same, and CPHHG from Ne shows the same behavior. Second, the cutoff of CPHHG is way closer to the LPHHG phase-matching cutoff of the shorter-wavelength driving beam.

Similar to LPHHG cutoff, the CPHHG cutoff can be increased by increasing the driving beams intensity. However, when too high intensities are used, the gas target will be over ionized. On one aspect, over-ionization will destroy phase matching and reduce the flux of CPHHG. On the other hand, the phase-matching window becomes shorter, and the harmonic linewidth becomes broader, thus the underlying supercontinuum level will increase and the circularity of the harmonics will reduce. For CPHHG cutoff presented in Fig. 4.17, the intensities of the driving beams are optimized. However it is possible to achieve higher CPHHG cutoff driven by the same wavelengths when the pulses of the driving beams are optimized, such as using driving beams with much shorter pulse durations.

4.3.3 Future directions

As discussed earlier, CPHHG driven by two-color counter-rotating CP fields is a universal way to generate CPHHG and it is promising to generate CPHHG at much higher photon energies. In this section, I will first talk about guidance to chose the wavelengths of the two driving beams. Then I will discuss ways to achieve higher-photon-energy CPHHG.

The harmonic spectra shown in Fig. 4.15(b) further confirm the universal nature of this generation scheme, and extend bright phase-matched harmonic generation using this scheme from ω + 1.65 ω (1.3 μm + 0.79 μm) [33], and ω + 2 ω (0.79 μm + 0.395 μm) [32] to ω + 2.53 ω (2 μm + 0.79 μm). This generation scheme works for a broad range of wavelengths, but not any. As Fig. 4.18 shows, the red peaks are the main harmonic pairs with left and right helicities, the blue peaks are the additional channels allowed by the imperfect circular polarization of the driving laser fields [31, 33, 52, 53]. Experimentally we minimize the blue peaks to generate CPHHG, and the main harmonics are very close to perfect circular polarization when the blue peaks are well suppressed.

The blue peaks and red peaks are well separated from each other in Fig. 4.18(a-c), which allows well suppression of the blue peaks by adjusting the circularity of the driving laser fields and the spatial and temporal overlap between the two beams. While in Fig. 4.18(d), the blue and red peaks sit at the same position. In this case, we do not know the peaks are linear or circular and the blue peaks can’t be suppressed. So although theoretically these two wavelengths allow the generation of CPHHG, experimentally it is almost impossible to get it work. However, if the polarization of the harmonics can be measured on real time or if there is a good way to ensure the close to perfect counter-rotating circular polarization of the two driving beams and the close to perfect temporal and spatial overlap between the two beams, this wavelength combination can still work experimentally. But either of these two cases is challenging to realize experimentally now.

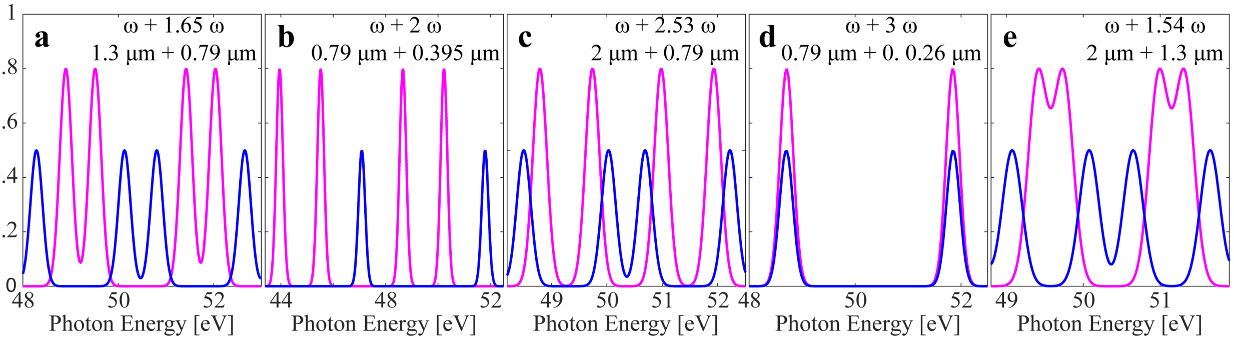

Figure 4.18: Wanted CPHHG harmonic pairs generated by channels of l = n ± 1 (red peaks), and unwanted harmonics allowed by the imperfect circularity of the driving lasers through additional generation channels of l = n ± 3 (blue peaks) [33] for driving beams at wavelength of ω + 1.65 ω (1.3 μm + 0.79 μm) (a), ω + 2 ω (0.79 μm + 0.395 μm) (b), ω + 2.53 ω (2 μm + 0.79 μm) (c), ω + 3 ω (0.79 μm + 0.26 μm) (d), and ω + 1.54 ω (2 μm + 1.3 μm) (e). In experiment, initially both the red and blue harmonics are present, then the circularity of the two driving beams, as well as the spatial and temporal overlap between the two beams are optimized to minimize the blue peaks to generate CPHHG.

Another case that is hard to generate CPHHG is when the two beams are too close in wavelength as Fig. 4.18(e) shows. We know the energy spacing between left and right harmonics within each pair is the photon energy difference of the two driving beams. If the two beams are two close in wavelength, the left and right harmonics within each pair will merge together and the overall polarization becomes linear. Assume the full width at half maximum of the left and right harmonics are f_1 and f_2, respectively. Typical values of f_1 and f_2 are around 0.15 eV for Ar, 0.3 eV for Ne, and 0.35 eV for He for CPHHG driven by the wavelengths in Fig. 4.18(a-c). And f_1 and f_2 are expected to be bigger values when CPHHG is driven by lasers with longer wavelengths since the phase matching window is going to be shorter [75]). Equation $f_1 + f_2 \leq 2(\omega_1 - \omega_2)$ needs to be fulfilled to allow a good separation between the two harmonics within each pair. In summary, the wavelengths of the two beams need to be carefully chosen so that the blue and red peaks are well separated from each other to allow the experimental minimization of the blue peaks, and the left and right harmonics within each pair are well separated from each other to avoid merging of the two helicities.

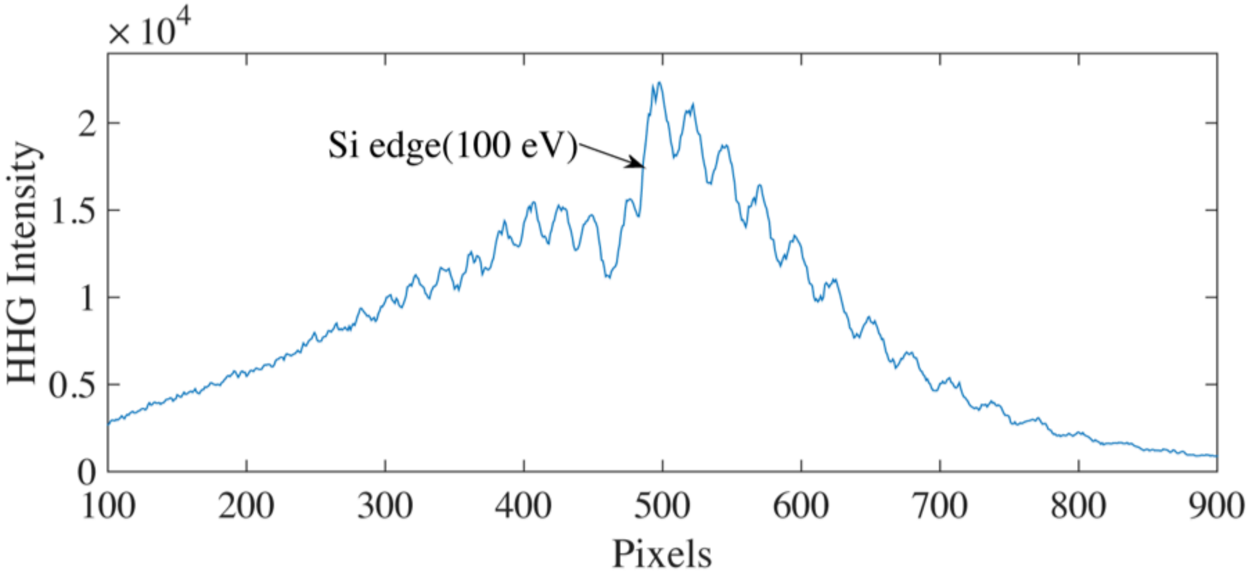

Figure 4.19: Experimental CPHHG spectrum driven by 2 μm + 1.3 μm. The separation of left and right harmonics within each pair can be barely recognized and a supercontinuum level is dominant.

When CPHHG is driven by laser beams with wavelengths of 2 μm and 1.3 μm as shown in Fig. 41.9. A supercontinuum structure is dominant and we can barely recognize the separation of left and right harmonics within each pair, just like the simulation shows in Fig. 4.18(e). There are several reasons for this spectral structure. First, lasers with longer wavelength have smaller photon energies while generate HHG at higher photon energies, so more photons need to be absorbed to generate a harmonic photon. Thus the probability of absorbing the “wrong” photons and the amplitude of the additional channels are bigger [33, 52, 53], which leads to a higher underlying supercontinuum level and a smaller circularity. Second, the temporal phase-matching window is shorter [75], so the harmonic linewidth is broader, which leads to easier merging of left and right harmonics within each pair and a higher underlying supercontinuum level. Third, for the two wavelengths used here $\omega_1 - \omega_2$ = 0.33 eV, which is even smaller than the full width half maximum of a single harmonic and could not allow the well separation of the left and right harmonics within each pair.

Based on the discussions in this chapter, several directions can be elevated to generate CPHHG at higher photon energies. First, improving the circularity of the driving laser fields, which will reduce the probability of absorbing the "wrong" photons. This can be done by improving the optics, which technologically depends on the development of optics. Another option is the inline geometry presented in Ref. [169], which is a very promising way to ensure the high degree of circular polarization of the driving beams. Second, generating CPHHG from ion using laser beams with short wavelength [93], which will reduce the probability of absorbing the "wrong" photons since the photon energies of the driving beams are bigger. What's more, this method greatly increases the phase matching window, thus decrease the harmonic linewidth, and increase the separation of two harmonics within each pair. Finally the two driving beams should be well separated in wavelength to allow good separation of left and right harmonics within each pair. In our case, the output of the OPA can be tuned to 2.52 μm (the idler beam) and 1.15 μm (the signal beam), these two wavelengths give an energy separation of 0.59 eV between the two harmonics within each pair and are expected to improve the situation a lot.

4.4 Circularly polarized high harmonics in non-collinear geometry

Another method to generate CPHHG was demonstrated recently by our group. In this experiment, angularly isolated beams of CP EUV light are generated through the first implementation of non-collinear HHG driven by two counter-rotating CP laser beams as shown in Fig. 4.20. This non-collinear technique allows the separation of the harmonics from the pump beam, the production of angularly-separated left and right CP harmonics at the same wavelength, and the capability of separating different harmonic orders without using a spectrometer [42].

As shown in Fig. 4.20(c), in the wave model, the two beams sum to yield an electric field with a rotating linear polarization across the transverse direction of the laser focus. It behaves like a 'rotating polarization grating' that generates circular polarization in the far field. In the photon model, the output direction of each harmonic follows the simple vector addition rule as shown in Fig. 4.20(b). This allows left and right circular harmonics pointing in different directions, even allows the separation of different harmonic orders without a spectrometer. Thus this method can isolate circular harmonics with a single helicity. Considering the high expense and low efficiency of EUV optics, this geometry constitutes a substantial advantage [42].

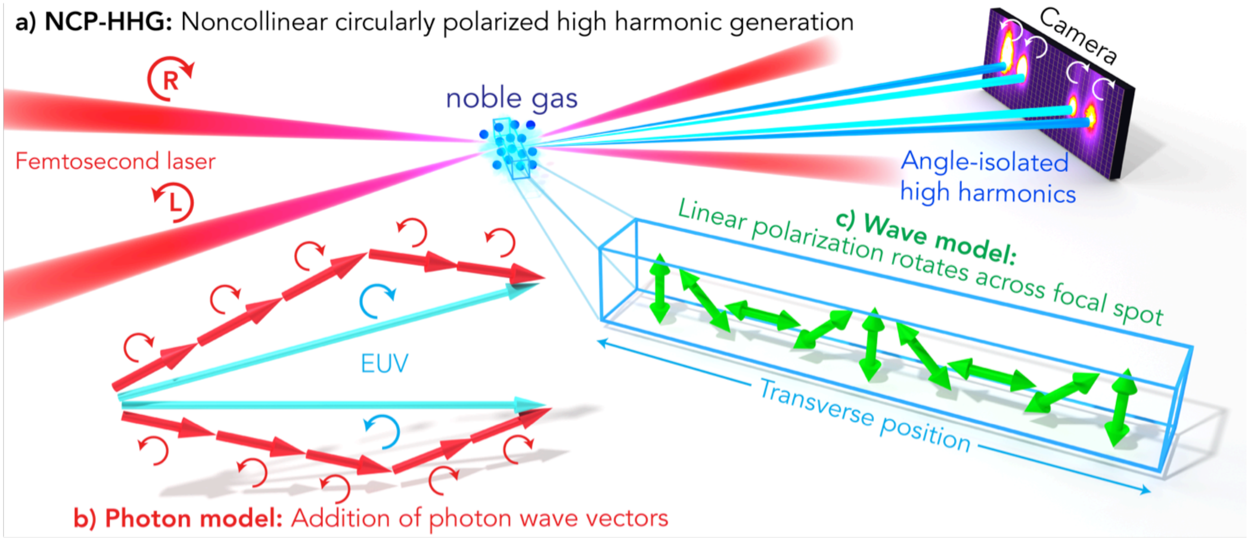

Figure 4.20: Non-collinear CPHHG. (a) In the experiment, two counter-rotating CP laser pulses are focused into a noble gas (Xe, Ar or Ne) to produce both left and right

CPHHG beams. (b) In the photon model, the output direction of each harmonic follows the simple vector addition of the wavevectors for each absorbed photon. (c) In the wave model, the two CP beams sum to yield an electric field that exhibits linear polarization, which rotates as a function of the transverse position across the laser focus, producing a ‘rotating polarization grating’ that generates circular polarization in the far field. This figure is captured from [42].

What’s more, in contrast to CPHHG in collinear geometry where the two driving beams need to be well separated in wavelength, CPHHG in non-collinear geometry can be driven by two laser beams at the same wavelength. Thus the cutoff energy of non-collinear CPHHG is similar to LPHHG. Very importantly, non-collinear CPHHG allows the generation of CP isolated attosecond pulses when few-cycle laser pulses are used [42, 170].

4.5 Summary

In summary, in the first half of this chapter I demonstrated the first bright phase-matched soft X-ray HHG with circular polarization using two-color counter-rotating CP 0.79-μm and 1.3-μm driving lasers. The unique harmonic spectrum is explained by the microscopic and macroscopic physics of the generation process. This powerful new light source allowed us to perform the first tabletop soft XMCD measurements at the $N_{4,5}$ absorption edges (~145 eV) of the technologically important rare earth metal Gd. Such materials are of wide interest since they are potentially important for next generation data storage media using all-optical switching, and were inaccessible to investigation via tabletop HHG until now. Finally, this work demonstrates that CPHHG can be implemented across a broad range of photon energies, enhancing our ability to control X-ray light using laser light, and provides a breakthrough tool for probing ultrafast magnetization dynamics using tabletop soft X-rays.

In the second half of this chapter, I presented bright phase-matched CPHHG generated, for the first time, by using beams with wavelength of 2 μm and 0.79 μm, which extends phased-matched CPHHG to a broader wavelengths and further confirmed the universal nature of this generation scheme. In addition, I showed that the helicity dependent intensity asymmetry of the spectra is mostly caused by the helicity dependent single-atom physics. What's more, this asymmetry can reverse and CPHHG generated from Ar exhibits a single helicity for the high-photon-energy region of the spectrum, which provides a convenient way to generate CPHHG with a single helicity and CP attosecond pulse trains. Moreover, the experimental cutoff energies of CPHHG are discussed by comparing with LPHHG cutoff energies of the two driving beams, which provides guidance about cutoff energies can be achieved when using different wavelengths and different gas targets. Finally simple simulations show guidance for choosing the wavelengths of the two beams, and future directions for generating CPHHG at higher photon energies are discussed.

At the end of this chapter, non-collinear CPHHG was briefly introduced. This technique allows the separation of left and right CPHHG beams and even the separation of every harmonic order without using a spectrometer. And this method can be used to generate isolated CP attosecond pulses.

Bibliography

[1] E. Whaites, R. A. Cawson, "Essentials of Dental Radiography and Radiology", *Elsevier Health Sciences* pp. 15–20 (2002)

[2] J. M. Glownia, J. Cryan, J. Andreasson et al., "Time-resolved pump-probe experiments at the LCLS", *Opt. Express* **18**(17), 17620–17630 (2010)

[3] H. T. Lemke, C. Bressler, L. X. Chen et al., "Femtosecond X-ray absorption spectroscopy at a hard x-ray free electron laser: Application to spin crossover dynamics", *J. Phys. Chem. A* **117**(4), 735–740 (2013)

[4] T. E. Glover, D. M. Fritz, M. Cammarata et al., "X-ray and optical wave mixing", *Nature* **488**(7413), 603–608 (2012)

[5] A. Rundquist, C. G. Durfee, Z. Chang, C. Herne, S. Backus, M. M. Murnane, and H. C. Kapteyn, "Phase-Matched Generation of Coherent Soft X-rays", *Science* **280**(5368), 1412–1415 (1998)

[6] R. A. Bartels, A. Paul, H. Green et al., "Generation of spatially coherent light at extreme ultraviolet Wavelengths," *Science* **297**(5580), 376–378 (2002)

[7] T. Popmintchev, M.-C. Chen, D. Popmintchev et al., "Bright coherent ultrahigh harmonics in the keV X-ray regime from mid-infrared femtosecond lasers", *Science* **336**(6086), 1287–1291 (2012)

[8] C. G. Durfee, A. R. Rundquist, S. Backus, C. Herne, M. M. Murnane, and H. C. Kapteyn, "Phase matching of high-order harmonics in hollow waveguides", *Phys. Rev. Lett.* **83**(11), 2187–2190 (1999)

[9] E. Constant, D. Garzella, P. Breger, E. Mével, Ch. Dorrer, C. Le Blanc, F. Salin, and P. Agostini, "Optimizing high harmonic generation in absorbing gases: Model and experiment", *Phys. Rev. Lett.* **82**(8), 1668–1671 (1999)

[10] I. P. Christov, M. M. Murnane, and H. C. Kapteyn, "High-harmonic generation of attosecond pulses in the "single-cycle" regime", *Phys. Rev. Lett.* **78**(7), 1251–1254 (1997)

[11] G. Sansone, E. Benedetti, F. Calegari et al., "Isolated single-cycle attosecond pulses", *Science* **314**(5798), 443–446 (2006)

[12] E. Goulielmakis, M. Schultze, M. Hofstetter et al., "Single-cycle nonlinear optics", *Science* **320**(5883), 1614–1617 (2008)

[13] R. Velotta, N. Hay, M. B. Mason, M. Castillejo, and J. P. Marangos, "High-order harmonic generation in aligned molecules", *Phys. Rev. Lett.* **87**(18), 183901 (2001)

[14] N. L. Wagner, A. Wüest, I. P. Christov et al., "Monitoring molecular dynamics using coherent electrons from high harmonic generation", *Proc. Natl. Acad. Sci. U.S.A.* **103**(36), 13279–13285 (2006)

[15] Z. H. Loh, M. Khalil, R. E. Correa et al., "Quantum state-resolved probing of strong-field-ionized xenon atoms using femtosecond high-order harmonic transient absorption spectroscopy", *Phys. Rev. Lett.* **98**(14), 143601 (2007)

[16] W. Li, X. Zhou, R. Lock, S. Patchkovskii, A. Stolow, H. C. Kapteyn, and M. M. Murnane, "Time-Resolved Dynamics in N_2O_4 Probed Using High Harmonic Generation", *Science* **322**(5905), 1207–1211 (2008)

[17] R. Haight and D. R. Peale, "Tunable photoemission with harmonics from subpicosecond lasers", *Rev. Sci. Instrum.* **65**(6), 1853–1857 (1994)

[18] R. Haight and P. F. Seidler, "High resolution atomic core level spectroscopy with laser harmonics", *Appl.Phys. Lett.* **65**(5), 517–519 (1994)

[19] M. Probst and R. Haight, "Unoccupied molecular orbital states of tris (8-hydroxy quinoline) aluminum: Observation and dynamics", *Appl. Phys. Lett.* **71**(2), 202–204 (1997)

[20] K. Read, H. S. Karlsson, M. M. Murnane et al., "Excitation dynamics of dye doped tris (8-hydroxy quinolone) aluminum films studied using time-resolved photoelectron spectroscopy", *J. Appl. Phys.* **90**(1), 294–300 (2001)

[21] M. E. Siemens, Q. Li, R. Yang et al., "Quasi-ballistic thermal transport from nanoscale interfaces observed using ultrafast coherent soft X-ray beams", *Nat. Mater.* **9**(1), 26–30 (2010)

[22] E. Turgut, C. La-o-Vorakiat, J. M. Shaw et al., "Controlling the competition between optically induced ultrafast spin-flip scattering and spin transport in magnetic multilayers", *Phys. Rev. Lett.* **110**(19), 197201 (2013)

[23] S. Hellmann, T. Rohwer, M. Kalläne, K. Hanff, C. Sohrt, A. Stange, A. Carr, M. M. Murnane, H. C. Kapteyn, L. Kipp, M. Bauer, and K. Rossnagel, "Time-

domain classification of charge-density-wave insulators", *Nat. Commun.* **3**, 1069 (2012)

[24] M. D. Seaberg, D. E. Adams, E. L. Townsend et al., "Ultrahigh 22 nm resolution coherent diffractive imaging using a desktop 13 nm high harmonic source", *Opt. Express* **19**(23), 22470–22479 (2011)

[25] M. D. Seaberg, B. Zhang, D. F. Gardner et al., "Tabletop Nanometer Extreme Ultraviolet Imaging in an Extended Reflection Mode using Coherent Fresnel Ptychography", *Optica* **1**(1), 39-44 (2014)

[26] T. Popmintchev, M.-C. Chen, O. Cohen, M. E. Grisham, J. J. Rocca, M. M. Murnane, and H. C. Kapteyn, "Extended phase matching of high harmonics driven by mid-infrared light", *Opt. Lett.* **33**(18), 2128–2130 (2008)

[27] T. Popmintchev, M.-C. Chen, A. Bahabad et al., "Phase matching of high harmonic generation in the soft and hard X-ray regions of the spectrum", *Proc. Natl. Acad. Sci. U.S.A.* **106**(26), 10516–10521 (2009)

[28] M.-C. Chen, P. Arpin, T. Popmintchev et al., "Bright, coherent, ultrafast soft x-ray harmonics spanning the water window from a tabletop light source", *Phys. Rev. Lett.* **105**(17), 173901 (2010)

[29] G. Andriukaitis, T. Balinas, S. Ališauskas et al., "90 GW peak power few-cycle mid-infrared pulses from an optical parametric amplifier", *Opt. Lett.* **36**(15), 2755–2757 (2011)

[30] H. Xiong, H. Xu, Y. Fu et al., "Generation of a coherent x ray in the water window region at 1 kHz repetition rate using a mid-infrared pump source", *Opt. Lett.* **34**(11), 1747–1749 (2009)

[31] A. Fleischer, O. Kfir, T. Diskin, P. Sidorenko, O. Cohen, "Spin angular momentum and tunable polarization in high-harmonic generation", *Nat. Photonics* **8**, 543–549 (2014)

[32] O. Kfir, P. Grychtol, E. Turgut et al., "Generation of bright phase-matched circularly-polarized extreme ultraviolet high harmonics", *Nat. Photonics* **9**, 99–105 (2015)

[33] T. Fan, P. Grychtol, R. Knut et al., "Bright circularly polarized soft X-ray high harmonics for X-ray magnetic circular dichroism", *Proc. Natl. Acad. Sci. U.S.A.* **112** (46), 14206-14211 (2015)

[34] I. Radu, K. Vahaplar, C. Stamm et al., "Transient ferromagnetic-like state mediating ultrafast reversal of antiferromagnetically coupled spins", *Nature* **472**, 205–208 (2011)

[35] M. H. M. Janssen and I. Powis, “Detecting chirality in molecules by imaging photoelectron circular dichroism”, *Phys. Chem. Chem. Phys.* **16**, 856 (2014)

[36] J. Bahrdt, A. Gaupp, W. Gudat et al., “Circularly polarized synchrotron radiation from the crossed undulator at BESSY”, *Rev. Sci. Instrum.* **63**, 339 (1992)

[37] A. A. Lutman, J. P. MacArthur, M. Ilchen et al., “Polarization control in an X-ray free-electron laser”, *Nat. Photonics* **10**, 468–472 (2016)

[38] B. Vodungbo, A. B. Sardinha, J. Gautier et al., “Polarization control of high order harmonics in the EUV photon energy range”, *Opt. Express* **19**, 4346–4356 (2011)

[39] X. Zhou, R. Lock, N. Wagner, W. Li, H. C. Kapteyn, and M. M. Murnane, “Elliptically Polarized High-Order Harmonic Emission from Molecules in Linearly Polarized Laser Fields”, *Phys. Rev. Lett.* **102**, 073902 (2009)

[40] A. Ferré, C. Handschin, M. Dumergue et al., “A table-top ultrashort light source in the extreme ultraviolet for circular dichroism experiments”, *Nat. Photonics* **9**, 93–98 (2015)

[41] G. Lambert, B. Vodungbo, J. Gautier et al., “Towards enabling femtosecond helicity-dependent spectroscopy with high-harmonic sources”, *Nat. Commun.* **6**, 6167 (2015)

[42] D. D. Hickstein, F. J. Dollar, P. Grychtol et al., “Non-collinear generation of angularly isolated circularly polarized high harmonics”, *Nat. Photonics* **9**, 743–750 (2015)

[43] H. Eichmann, A. Egbert, S. Nolte, C. Momma, B. Wellegehausen, W. Becker, S. Long, and J. K. McIver, “Polarization-dependent high-order two-color mixing”, *Phys. Rev. A* **51**, R3414 (1995)

[44] S. Long, W. Becker, and J. K. McIver, “Model calculations of polarization-dependent two-color high-harmonic generation”, *Phys. Rev. A* **52**(3), 2262–2278 (1995)

[45] D. B. Milošević, W. Becker, and R. Kopold, “Generation of circularly polarized high-order harmonics by two-color coplanar field mixing”, *Phys. Rev. A* **61**, 063403 (2000)

[46] D. B. Milošević, W. Becker, and R. Kopold, “High-harmonic generation by two-color circularly polarized field mixing”, *Atoms, Molecules and Quantum Dots in Laser Fields: Fundamental Processes, Conference Proceedings* **71**, 239–252 (2001)

[47] D. B. Milošević, W. Becker, R. Kopold, and W. Sandner, “High-harmonic generation by a bichromatic bicircular laser field”, *Laser Phys.* **11,** 165–168 (2001)

[48] W. Becker, F. Grasbon, R. Kopold, D. B. Milošević, G. G. Paulus, and H. Walther, “Above-threshold ionization: From classical features to quantum effects”, *Adv. At. Mol. Opt. Phys.* **48**, 35–98 (2002)

[49] D. B. Milošević, and W. Becker, “Attosecond pulse trains with unusual nonlinear polarization”, *Phys. Rev. A* **62**, 011403 (2000)

[50] D. B. Milošević, “Generation of elliptically polarized attosecond pulse trains”, *Opt. Lett.* **40**, 2381 (2015)

[51] D. B. Milošević, “Circularly polarized high harmonics generated by a bicircular field from inert atomic gases in the p state: a tool for exploring chirality-sensitive processes”, *Phys. Rev. A* **92**, 043827 (2015)

[52] E. Pisanty, S. Sukiasyan, and M. Ivanov, “Spin conservation in high-order-harmonic generation using bicircular fields”, *Phys. Rev. A* **90**, 043829 (2014)

[53] D. B. Milošević, “High-order harmonic generation by a bichromatic elliptically polarized field: Conservation of angular momentum”, *J. Phys. B: At. Mol. Opt. Phys.* **48**, 171001 (2015)

[54] O. Kfir, P. Grychtol, E. Turgut et al., “Helicity-selective phase-matching and quasi-phase matching of circularly polarized high-order harmonics: towards chiral attosecond pulses”, *J. Phys. B: At. Mol. Opt. Phys.* **49**, 123501 (2016)

[55] K. M. Dorney, J. L. Ellis, C. Hernández-García et al., “Helicity-selective enhancement and polarization control of attosecond high harmonic waveforms driven by bichromatic circularly polarized laser fields”, *Phys. Rev. Lett.* Under review (2017)

[56] X. Zhang, L. Li, X. Zhu, X. Liu, Q. Zhang, P. Lan, and P. Lu, “Helicity reversion in high-order-harmonic generation driven by bichromatic counter-rotating circularly polarized laser fields”, *Phys. Rev. A* **94**, 053408 (2016)

[57] C. Bressler and M. Chergui, “Ultrafast X-ray Absorption Spectroscopy”, *Chem. Rev.* **104**, 1781-1812 (2004)

[58] T. H. Maiman, “Stimulated Optical Radiation in Ruby”, *Nature* **187**(4736), 493-494. (1960)

[59] A. L. Schawlow and C. H. Townes, “Infrared and Optical Masers”, *Phys. Rev.* **112**, 1940 (1958)

[60] P. A. Franken, A. E. Hill, and C. W. Peters, “Generation of Optical Harmonics”, *Phys. Rev. Lett.* **7**, 118 (1961)

[61] R. W. Terhune, P. D. Maker, and C. M. Savage, “Optical Harmonic Generation in Calcite”, *Phys. Rev. Lett.* **8**, 404 (1962)

[62] P. D. Maker and R. W. Terhune, “Study of Optical Effects Due to an Induced Polarization Third Order in the Electric Field Strength”, *Phys. Rev.* **137**, A801 (1965)

[63] G. H. C. New and J. F. Ward, “Optical Third-Harmonic Generation in Gases”, *Phys. Rev. Lett.* **19**, 556 (1967)

[64] J. Wildenauer, “Generation of the ninth, eleventh, and fifteenth harmonics of iodine laser radiation”, *J. Appl. Phys.* **62**, 41 (1987)

[65] N. H. Burnett, H. A. Baldis, M. C. Richardson, and G. D. Enright, “Harmonic generation in CO_2 laser target interaction”, *Appl. Phys. Lett.* **31**, 172 (1977)

[66] A. McPherson, G. Gibson, H. Jara et al., “Studies of multiphoton production of vacuum-ultraviolet radiation in the rare gases”, *J. Opt. Soc. of Am. B* **4**, 595-601 (1987)

[67] M. Ferray, A. L’Huillier, X. F. Li, L. A. Lompre, G. Mainfray, and C. Manus, “Multiple-harmonic conversion of 1064 nm radiation in rare gases”, *J. Phys. B: At, Mol. Opt. Phys.* **21**, L31-L35 (1988)

[68] X. F. Li, A. L’Huillier, M. Ferray, L. A. Lompré, and G. Mainfray, “Multiple-harmonic generation in rare gases at high laser intensity”, *Phys. Rev. A* **39**, 5751 (1989)

[69] S. Backus, C. G. Durfee, M. M. Murnane, and H. C. Kapteyn, “High power ultrafast lasers”, *Rev. Sci. Instrum.* **69**(3), 1207-1223 (1998)

[70] J. Zhou, J. Peatross, M. M. Murnane, H. C. Kapteyn, and I. P. Christov, “Enhanced High-Harmonic Generation Using 25 fs Laser Pulses”, *Phys. Rev. Lett.* **76**, 752 (1996)

[71] Z. Chang, A. Rundquist, H. Wang, M. M. Murnane, and H. C. Kapteyn, “Generation of Coherent Soft X Rays at 2.7 nm Using High Harmonics”, *Phys. Rev. Lett.* **79**, 2967 (1997)

[72] P. M. Paul, E. S. Toma, P. Breger, G. Mullot, F. Augé, Ph. Balcou, H. G. Muller, and P. Agostini, “Observation of a Train of Attosecond Pulses from High Harmonic Generation”, *Science* **292**(5522), 1689-1692 (2001)

[73] Y. Mairesse, A. de Bohan, L. J. Frasinski et al., “Attosecond Synchronization of High-Harmonic Soft X-rays”, *Science* **302**(5650), 1540-1543 (2003)

[74] P. B. Corkum, N. H. Burnett, and M. Y. Ivanov, “Subfemtosecond pulses”, *Opt. Lett.* **19**(22), 1870-1872 (1994)

[75] M.-C. Chen, C. Mancuso, C. Hernández-García et al., “Generation of bright isolated attosecond soft X-ray pulses driven by multicycle midinfrared lasers”, *Proc. Natl. Acad. Sci. U.S.A.* **111**(23), E2361–E2367 (2014)

[76] E. A. Gibson, A. Paul, N. Wagner et al., “Coherent Soft X-ray Generation in the Water Window with Quasi-Phase Matching”, *Science* **302**(5642), 95-98 (2003)

[77] X. Zhang, A. L. Lytle, T. Popmintchev et al., “Quasi-phase-matching and quantum-path control of high-harmonic generation using counterpropagating light”, *Nat. Phys.* **3**, 270-275 (2007)

[78] J. L. Krause, K. J. Schafer, and K. C. Kulander, “High-order harmonic generation from atoms and ions in the high intensity regime”, *Phys. Rev. Lett.* **68**, 3535–3538 (1992)

[79] P. B. Corkum, “Plasma perspective on strong field multiphoton ionization”, *Phys. Rev. Lett.* **71**, 1994 (1993)

[80] M. Lewenstein, Ph. Balcou, M. Yu. Ivanov, A. L’Huillier, and P. B. Corkum, “Theory of high-harmonic generation by low-frequency laser fields”, *Phys. Rev. A* **49**, 2117–2132 (1994)

[81] T. Popmintchev, M.-C. Chen, P. Arpin, M. M. Murnane, and H. C. Kapteyn, “The attosecond nonlinear optics of bright coherent X-ray generation”, *Nat. Photonics* **4**(12), 822–832 (2010)

[82] J. Tate, T. Auguste, H. G. Muller, P. Salieres, P. Agostini, and L. F. DiMauro, “Scaling of wave-packet dynamics in an intense midinfrared field”, *Phys. Rev. Lett.* **98**(1), 13901 (2007)

[83] K. Schiessl, K. L. Ishikawa, E. Persson, and J. Burgdörfer, “Wavelength dependence of high-harmonic generation from ultrashort pulses”, *J. Mod. Opt.* **55**(16), 2617–2630 (2008)

[84] M. V. Frolov, N. L. Manakov, and A. F. Starace, “Wavelength scaling of high-harmonic yield: threshold phenomena and bound state symmetry dependence”, *Phys. Rev. Lett.* **100**(17), 173001 (2008)

[85] NDE-ED.ORG, “Production of Radiation for Industrial Radiography”, available from website: https://www.ndeed.org/EducationResources/CommunityCollege/RadiationSafety/theory/production.htm

[86] L.V. Keldysh, “Ionization in the field of a strong electromagnetic wave”, *J. Exp. Theor. Phys.* **20**(5), 1307 (1965)

[87] E. Mevel, P. Breger, R. Trainham, G. Petite, P. Agostini, A. Migus, J.-P. Chambaret, and A. Antonetti, “Atoms in strong optical fields: Evolution from multiphoton to tunnel ionization”, *Phys. Rev. Lett.* **70**(4), 406–409 (1993)

[88] T. Popmintchev, “Tunable Ultrafast Coherent Light in the Soft and Hard X-ray Regions of the Spectrum: Phase Matching of Extreme High-Order Harmonic Generation”, PhD thesis at the University of Colorado at Boulder (2010)

[89] M. V. Ammosov, N. B. Delone, V. P. Krainov, “Tunnel ionization of complex atoms and of atomic ions in an alternating electromagnetic field”, *J. Exp. Theor. Phys.* **64**, 1191-1194 (1986)

[90] M. Protopapas, C. H. Keitel, and P. L. Knight, “Atomic physics with super-high intensity lasers”, *Rep. Prog. Phys.* **60**, 389–486 (1997)

[91] P. B. Corkum, N. H. Burnett, and F. Brunel, “Above-threshold ionization in the long-wavelength limit”, *Phys. Rev. Lett.* **62**(11), 1259–1262 (1989)

[92] C. Jin, “Theory of Nonlinear Propagation of High Harmonics Generated in a Gaseous Medium”, PhD Thesis at Kansas State University, USA (2013)

[93] D. Popmintchev, C. Hernández-García, F. Dollar et al., “Efficient soft X-ray high harmonic generation in multiply-ionized plasmas: the ultraviolet surprise”, *Science* **350**, 1225 (2015)

[94] Ch. Spielmann, N. H. Burnett, S. Sartania et al., “Generation of Coherent X-rays in the Water Window Using 5-Femtosecond Laser Pulses”, *Science* **278**(5338), 661-664 (1997)

[95] P. Agostini, F. Fabre, G. Mainfray, G. Petite, and N. K. Rahman, “Free-free transitions following six-photon ionization of xenon atoms”, *Phys. Rev. Lett.* **42**, 1127–1130 (1979)

[96] G. G. Paulus, W. Nicklich, H. Xu, P. Lambropoulos, and H. Walther, “Plateau in above threshold ionization spectra”, *Phys. Rev. Lett.* **72**, 2851–2854 (1994)

[97] D. N. Fittinghoff, P. R. Bolton, B. Chang, and K. C. Kulander, “Observation of nonsequential double ionization of helium with optical tunneling”, *Phys. Rev. Lett.* **69**, 2642–2645 (1992)

[98] B. Walker, B. Sheehy, L. F. DiMauro, P. Agostini, K. J. Schafer, and K.C. Kulander, “Precision measurement of strong field double ionization of helium”, *Phys. Rev. Lett.* **73**, 1227–1230 (1994)

[99] K. Schiessl, K. L. Ishikawa, E. Persson, and J. Burgdörfer, “Quantum path interference in the wavelength dependence of high-harmonic generation”, *Phys. Rev. Lett.* **99**, 253903 (2007)

[100] A. D. Shiner, C. Trallero-Herrero, N. Kajumba et al., “Wavelength Scaling of High Harmonic Generation Efficiency”, *Phys. Rev. Lett.* **103**, 073902 (2009)

[101] A. Paul, E. A. Gibson, X. Zhang et al., “Phase-matching techniques for coherent soft X-ray generation”, IEEE J. Quantum Electron. **42**, 14 (2006)

[102] M.-C. Chen, “Modifying Driving Laser Wavelength to Generate Coherent, Ultrafast X-rays from Phase-Matched High-Order Harmonics”, PhD thesis at the University of Colorado at Boulder (2012)

[103] E. Seres, J. Seres, and C. Spielmann, “X-ray absorption spectroscopy in the keV range with laser generated high harmonic radiation”, *Appl. Phys. Lett.* **89**(18), 181919 (2006)

[104] B. Shan and Z. Chang, “Dramatic extension of the high-order harmonic cutoff by using a long-wavelength driving field”, *Phys. Rev. A* **65**, 011804(R) (2001)

[105] J. Seres, E. Seres, A. J. Verhoef, G. Tempea et al., “Laser technology: Source of coherent kiloelectronvolt X-rays”, *Nature* **433**, 596 (2005)

[106] G. Cerullo and S. De Silvestri, “Ultrafast optical parametric amplifiers”, *Rev. Sci. Instrum.* **74**(1), 1–17 (2003)

[107] L. V. Dao, C. Hall, H. L. Vu, K. B. Dinh, E. Balaur, P. Hannaford, and T. A. Smith, “Phase-matched generation of highly coherent radiation in water window region”, *Appl. Opt.* **51**(18), 4240–4245 (2012)

[108] N. Ishii, K. Kaneshima, K. Kitano, T. Kanai, S. Watanabe, and J. Itatani, “Carrier-envelope phase-dependent high harmonic generation in the water window using few-cycle infrared pulses”, *Nat. Commun.* **5**, 3331 (2014)

[109] D. C. Brown, “The promise of cryogenic solid-state lasers”, *IEEE J. Sel. Top. Quantum Electron.* **11**(3), 587–599 (2005)

[110] J.-M. Heritier, S. Fournier, G. J. Germann, B. Resan, R. Viselga, and A. Fry, “Cryogenically cooled Ti:Sapphire amplifiers”, *Proc. SPIE* **6451**, 64510V (2007)

[111] S. Backus, R. Bartels, S. Thompson, R. Dollinger, H. C. Kapteyn, and M. M. Murnane, “High-efficiency, single-stage 7-kHz high-average-power ultrafast laser system”, *Opt. Lett.* **26**(7), 465–467 (2001)

[112] I. Matsushima, H. Yashiro, and T. Tomie, “A 37% efficiency, kilohertz repetition rate cryogenically cooled ti:sapphire regenerative amplifier”, *Jpn. J. Appl. Phys.* **44**(25), L823–L826 (2005)

[113] S. M. Teichmann, F. Silva, S. L. Cousin, M. Hemmer, and J. Biegert, “0.5-keV Soft X-ray attosecond continua”,*Nat. Commun.* **7**, 11493 (2016)

[114] S. L. Cousin, F. Silva, S. Teichmann, M. Hemmer, B. Buades, and J. Biegert, “High-flux table-top soft x-ray source driven by sub-2-cycle, CEP stable, 1.85-μm 1-kHz pulses for carbon K-edge spectroscopy”, *Opt. Lett.* **39**, 5383–5386 (2014)

[115] C. Ding, W. Xiong, T. Fan et al., “High flux coherent super-continuum soft X-ray source driven by a single-stage, 10mJ, Ti:sapphire amplifier-pumped OPA”, *Opt. Express* **22**(5), 6194-6202 (2014)

[116] Ch. Bressler, C. Milne, V.-T. Pham et al., “Femtosecond XANES study of the light-induced spin crossover dynamics in an iron(II) complex”, *Science* **323**, 489–492 (2009)

[117] W. Ackermann, G. Asova, V. Ayvazyan et al., “Operation of a free-electron laser from the extreme ultraviolet to the water window”, *Nat. Photonics* **1**, 336–342 (2007)

[118] P. Emma, R. Akre, J. Arthur et al., “First lasing and operation of an ångstrom- wavelength free-electron laser”, *Nat. Photonics* **4**, 641–647 (2010)

[119] T. Ishikawa, H. Aoyagi, T. Asaka et al., “A compact X-ray free-electron laser emitting in the sub-ångström region”, *Nat. Photonics* **6**, 540– 544 (2012)

[120] E. Allaria, R. Appio, L. Badano et al., “Highly coherent and stable pulses from the FERMI seeded free-electron laser in the extreme ultraviolet”, *Nat. Photonics* **6**, 699–704 (2012)

[121] C. S. Schnohr and M. C. Ridgway (eds.), chapter 1 of “X-Ray Absorption Spectroscopy of Semiconductors”, Springer Series in Optical Sciences 190, DOI 10.1007/978-3-662-44362-0_1 (2015)

[122] J. J. Rehr and R. C. Albers, “Theoretical approaches to x-ray absorption fine structure”, *Rev. Mod. Phys.* **72**, 621 (2000)

[123] A. Messiah, “Quantum mechanics”, 9th edition (1976)

[124] http://chemwiki.ucdavis.edu/Physical_Chemistry/Spectroscopy/Xray_Spectroscopy/XANES%3A_Theory

[125] J. E. Penner-Hahn, “X-ray Absorption Spectroscopy”, the University of Michigan, Ann Arbor, MI, USA

[126] J. J. Rehr, J. J. Kas, F. D. Vila, M. P. Prange, and K. Jorissen, “Parameter-free calculations of X-ray spectra with FEFF9”, *Phys. Chem. Chem. Phys.* **12**, 5503 (2010)

[127] A. Filipponi, A. Di Cicco, and C. R. Natoli, “X-ray-absorption spectroscopy and n-body distribution functions in condensed matter. I. Theory”, *Phys. Rev. B* **52**, 15122 (1995)

[128] E. Hudson, D. A. Shirley, M. Domke et al., “High-resolution measurements of near-edge resonances in the core-level photoionization spectra of SF6”, *Phys. Rev. A* **47**, 361-373 (1993)

[129] M. Stener, P. Bolognesi, M. Coreno et al., “Photoabsorption and S 2p photoionization of the SF6 molecule: resonances in the excitation energy range of 200-280 eV”, *J. Chem. Phys.* **134**(17), 174311 (2011)

[130] O.-P. Sairanen, A. Kivimäki, E. Nõmmiste, H. Aksela, and S. Aksela, “High-resolution pre-edge structure in the inner-shell ionization threshold region of rare gases Xe, Kr, and Ar”, *Phys. Rev. A* **54**(4), 2834–2839 (1996)

[131] J. L. Dehmer, “Evidence of Effective Potential Barriers in the X-Ray Absorption Spectra of Molecules”, *J. Chem. Phys.* **56**, 4496-4504 (1972)

[132] P. Andersen, T. Andersen, F. Folkmann, V. K. Ivanov, H. Kjeldsen, and J. B. West, “Absolute cross sections for the photoionization of 4d electrons in Xe^+ and Xe^{2+} ions”, *J. Phys. B: At. Mol. Opt. Phys.* **34**, 2009-2019 (2001)

[133] J. Stöhr, J. L. Gland, E. B. Kollin, R. J. Koestner, A. L. Johnson, E. L. Muetterties, and F. Sette, “Desulfurization and Structural Transformation of Thiophene on the Pt(111) Surface”, *Phys. Rev. Lett.* **53**, 2161-2164 (1984)

[134] “World Geographic Overview”, (n.d.). Central Intelligence Agency, https://www.cia.gov/library/publications/the-world-factbook/geos/xx.html#Geo

[135] A. M. Helmenstine, (n.d.). "How Much of The Human Body Is Water?", http://chemistry.about.com/od/waterchemistry/f/How-Much-Of-Your-Body-Is-Water.htm

[136] S. Schreck, G. Gavrila, C. Weniger, and P. Wernet, "A sample holder for soft x-ray absorption spectroscopy of liquids in in transmission mode", *Rev. Sci. Instrum.* **82**, 103101 (2011)

[137] K. R. Wilson, B. S. Rude, T. Catalano, R. D. Schaller, J. G. Tobin, D. T. Co, and R. J. Saykally, "X-ray Spectroscopy of Liquid Water Microjets", *J. Phys. Chem. B* **105** (17), 3346–3349 (2001)

[138] C. P. Schwartz, J. S. Uejio, A. M. Duffin, W. S. Drisdell, J. D. Smith, and R. J. Saykally, "Soft X-ray absorption spectra of aqueous salt solutions with highly charged cations in liquid microjets", *Chem. Phys. Lett.* **493** 94–96 (2010)

[139] M. Ekimova, W. Quevedo, M. Faubel, P. Wernet, and E. T. J. Nibbering, "A liquid flatjet system for solution phase soft-x-ray spectroscopy", *Struct. Dyn.* **2**, 054301 (2015)

[140] P. L. Poole, C. D. Andereck, D. W. Schumacher et al., "Liquid crystal films as on-demand, variable thickness (50-5000 nm) targets for intense lasers", arXiv:1405.5901v1

[141] M. L. Cowan, B. D. Bruner, N. Huse et al., "Ultrafast memory loss and energy redistribution in the hydrogen bond network of liquid H2O," *Nature* **434**(7030), 199-202 (2005)

[142] D. Kraemer, M. L. Cowan, A. Paarmann et al., "Temperature dependence of the two-dimensional infrared spectrum of liquid H2O", *Proc. Natl. Acad. Sci. U.S.A.* **105**(2), 437-442 (2008)

[143] N. Huse, T. K. Kim, and L. Jamula, "Photo-Induced Spin-State Conversion in Solvated Transition Metal Complexes Probed via Time-Resolved Soft X-ray Spectroscopy", *J. Am. Chem. Soc.* **132** (19), 6809–6816 (2010)

[144] X. M. Tong, and S. I. Chu, "Generation of circularly polarized multiple high-order har- monic emission from two-color crossed laser beams", *Phys. Rev. A* **58**, 2656–2659 (1998)

[145] T. Fan, P. Gychtol, R. Knut et al., "Bright circularly polarized soft X-ray high harmonics for X-ray magnetic circular dichroism", *CLEO: 2015 Postdeadline Paper Digest* (Opt. Soc. Am., Washington, DC), JTh5C.1.

[146] S. Mangin, M. Gottwald, C-H. Lambert et al., "Engineered materials for all-optical helicity-dependent magnetic switching", *Nat. Mater.* **13**, 286–292 (2014)

[147] S. Mathias, C. La-O-Vorakiat, P. Grychtol, "Probing the timescale of the exchange interaction in a ferromagnetic alloy", *Proc. Natl. Acad. Sci. U.S.A.* **109**(13), 4792–4797 (2012)

[148] D. Rudolf, C. La-O-Vorakiat, M. Battiato et al., "Ultrafast magnetization enhancement in metallic multilayers driven by superdiffusive spin current", *Nat. Commun.* **3**, 1037 (2012)

[149] L. Medišauskas, J. Wragg, H. van der Hart, and M. Yu. Ivanov, "Generating isolated elliptically polarized attosecond pulses using bichromatic counterrotating circularly polarized laser fields", *Phys. Rev. Lett.* **115**, 153001 (2015)

[150] Center for X-ray Optics (1995–2010) X-ray interactions with matter: Optics. Available at henke.lbl.gov/optical_constants/

[151] D. D. Hickstein, P. Ranitovic, S. Witte et al., "Direct visualization of laser-driven electron multiple scattering and tunneling distance in strong-field ionization", *Phys. Rev. Lett.* **109**(7), 073004 (2012)

[152] C. Chen, Z. Tao, C. Hernández-García et al., "Tomographic reconstruction of circularly polarized high-harmonic fields: 3D attosecond metrology", *Sci. Adv.* **2**, el1501333 (2016)

[153] C. Hernández-García, J. A. Pérez-Hernández, J. Ramos, E. Conejero Jarque, L. Roso, and L. Plaja, "High-order harmonic propagation in gases within the discrete dipole approximation", *Phys. Rev. A* **82**, 033432 (2010)

[154] J. A. Pérez-Hernández, L. Roso, and L. Plaja, "Harmonic generation beyond the strong-field approximation: The physics behind the short-wave-infrared scaling laws", *Opt. Express* **17**(12), 9891–9903 (2009)

[155] C. Hernández-García, J. A. Pérez-Hernández, T. Popmintchev et al., "Zeptosecond High Harmonic keV X-Ray Waveforms Driven by Midinfrared Laser Pulses", *Phys. Rev. Lett.* **111**, 033002 (2013)

[156] A. Becker, and F. Faisal, "Intense-field many-body S-matrix theory", *J. Phys. At. Mol. Opt. Phys.* **38**, R1–R56 (2005)

[157] A. Tripathi, J. Mohanty, S. H. Dietze, O. G. Shpyrko, E. Shipton, E. E. Fullerton, S. S. Kim, and I. McNulty, "Dichroic coherent diffractive imaging", *Proc. Natl. Acad. Sci. U.S.A.* **108**(33), 13393–13398 (2011)

[158] S. Valencia, A. Gaupp, W. Gudat, H-Ch. Mertins, P. M. Oppeneer, D. Abramsohn, and C. M. Schneider, "Faraday rotation spectra at shallow core levels: 3p edges of Fe, Co, and Ni", *New J. Phys.* **8**, 254 (2006)

[159] P. M. Oppeneer, "Magneto-optical Kerr spectra", Handbook of Magnetic Materials, ed Buschow KHJ (Elsevier, Amsterdam) **13**, 229–422 (2001)

[160] J. Stöhr, H. C. Siegmann, "Magnetism: From Fundamentals to Nanoscale Dynamics" (Springer, Berlin) (2006)

[161] M. Pretorius, "Magnetooptische Effekte mit linear polarisierter Synchrotronstrahlung im Bereich der 3p-Absorptionskanten der 3d-Übergangsmetalle Fe, Co und Ni", PhD thesis (Universit at Hamburg, Hamburg, Germany) (1999)

[162] H. Höchst, D. Rioux, D. Zhao, and D. L. Huber, "Magnetic linear dichroism effects in reflection spectroscopy: A case study at the Fe $M_{2,3}$ edge", *J. Appl. Phys.* **81**, 7584–7588 (1997)

[163] J. E. Prieto, F. Heigl, O. Krupin, G. Kaindl, and K. Starke, "Magneto-optics of Gd and Tb in the soft X-ray resonance regions", *Phys. Rev. B* **68**, 134453 (2003)

[164] J. E. Prieto, F. Heigl, O. Krupin, G. Kaindl, and K. Starke, "Prediction of huge X-ray Faraday rotation at the Gd $N_{4,5}$ threshold", *Phys. Rev. B* **66**, 172408 (2002)

[165] Y. Takayama, M. Shinoda, K. Obu et al., "Magnetic circular dichroism of X-ray emission for gadolinium in 4d–4f excitation region", *J. Phys. Soc. Jpn.* **71**, 340–346 (2002)

[166] K. Starke, F. Heigl, A. Vollmer, M. Weiss, G. Reichardt, and G. Kaindl, "X-Ray Magneto-optics in Lanthanides", *Phys. Rev. Lett.* **86**, 3415 (2001)

[167] D. Haskel, G. Srajer, J. C. Lang, J. Pollmann, C. S. Nelson, J. S. Jiang, and S. D. Bader, "Enhanced Interfacial Magnetic Coupling of Gd/Fe Multilayers", *Phys. Rev. Lett.* **87**, 207201 (2001)

[168] Center for X-ray Optics (2015) X-ray attenuation length. Available at henke.lbl.gov/optical_constants/atten2.html

[169] O. Kfir, E. Bordo, G. I. Haham, O. Lahav, A. Fleischer, and O. Cohen, "In-line production of a bi-circular field for generation of helically polarized high-order harmonics", *Appl. Phys. Lett.* **108**, 211106 (2016)

[170] C. Hernández-García, C. G. Durfee, D. D. Hickstein et al., “Schemes for generation of isolated attosecond pulses of pure circular polarization”, *Phys. Rev. A* **93**, 043855 (2016)

Appendix A

Liquid cell fabrication procedures

In this appendix, I will discuss the detailed steps of fabricating the liquid cell, i.e. the four silicon nitride membranes stacked together and housed by a metal enclosure to create three compartments. The two central silicon nitride membranes, which are purchased from Insight Nanofluidics, create a central compartment that allows the flowing of liquid. The out lid (out back) and the central up (central down) silicon nitride membranes create a compartment that allows gas to flow through the space between them to compensate the pressure inside the liquid compartment. As shown in Fig. 3.10(e), we need to create two holes, one silicon nitride window, and a gas flowing channel on the silicon substrate for the out lid piece. And as shown in Fig. 3.10(f), we need to create four holes, one silicon nitride window, and a gas flowing channel on the silicon substrate for the out back piece. The fabrication process of the out lid and out back pieces will be described.

1st step: Make the masks

The first step is to make masks for the out lid and out back pieces. Since for both of these two pieces, we need to create holes, windows, and channels, it is hard to get this done if the silicon substrate is coated with silicon nitride on one side. So I ordered silicon substrates that are coated with 300-nm thickness silicon nitride on both sides. To create all the structures, three masks are needed for each piece as shown in Fig. A1(b-d) and A2(b-d).

First, perform 300-nm silicon nitride etch (using machine RIE II) and silicon etch (using KOH bath) using mask Fig. A1(b) and A2(b) for the out lid and out back pieces, respectively. All the red parts will be etched. Thus three (five) 300-nm thickness silicon nitride windows are created on the back side of the substrate for the out lid (out back) piece. Note the red lines in Fig. A1(b) and A2(b) are etched by the same process too, so for the red lines only 300-nm silicon nitride are left after the process. We will break the red lines by hand at the end after finishing all the steps, so many pieces are created for a single batch. This is necessary since the whole process will take at least two days. Actually, the red lines will start to break after the first step, I will need to put tape on the back side after finishing the back side process to prevent the piece from breaking during the following processes.

Second, perform 300-nm silicon nitride etch on the front side (using machine RIE II) using mask Fig. A1(c) and A2(c). Thus two (four) holes are created for the out lid (out back) piece. Third, perform 270-nm silicon nitride etch on the front side (using machine RIE II) using mask Fig. A1(d) and A2(d). Thus a 270-nm deep gas channel and a 30-nm silicon nitride window are created for both pieces. After finishing all these steps, two holes (four holes), a 30-nm silicon nitride window, and a 270-nm deep gas flowing channel will be created for the out lid (out back) piece. The following are the detailed steps.

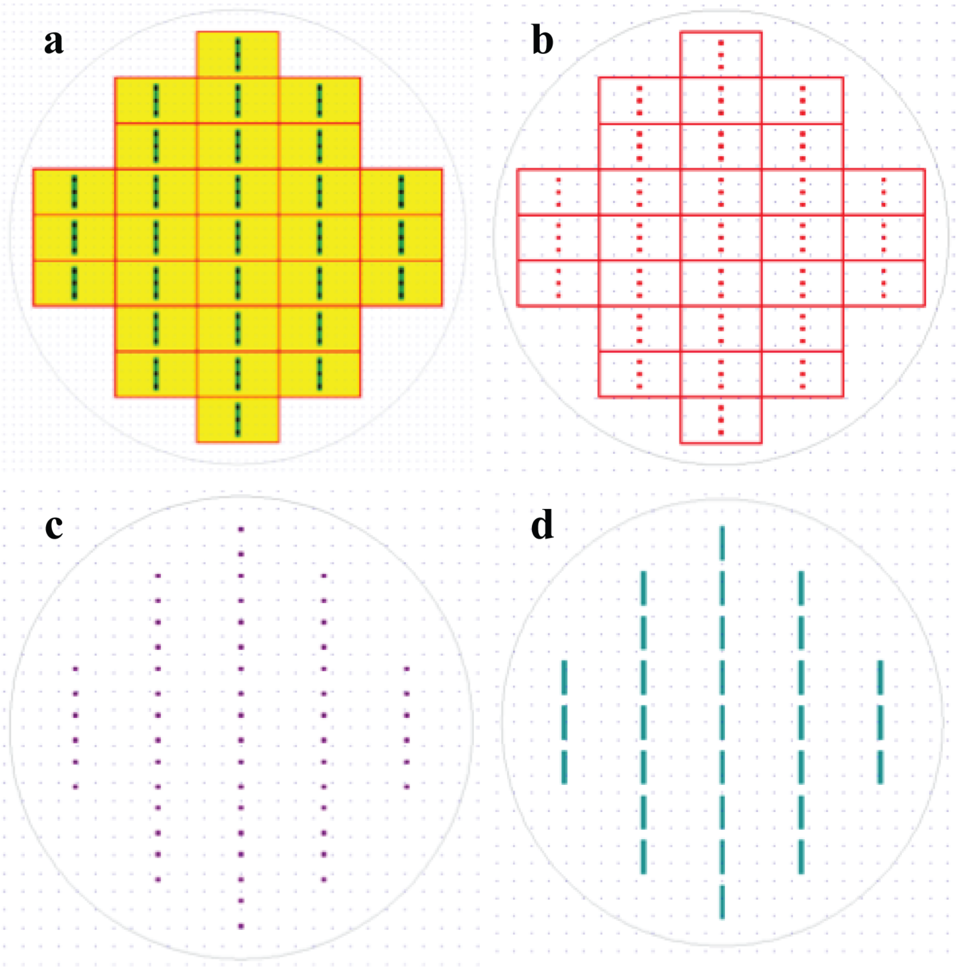

Figure A1: Masks for the out lid piece. The whole features (a) and the three masks (b, c, d) for the out lid piece.

1. Make the mask design as shown in Fig. A1 and A2 in the software CLEWIN, and save the design as CIF file.
2. Make mask in the machine Heidelberg. Order masks and boxes on the CNL website (User Menu > Supplies > Heidelberg Masks and Boxes). Mask is made of sodalime glass (which is transparent), chromium and photoresist. Load the CIF file into the Heidelberg. Preview, fill, invert it and mirror check

at y (so it shows the same pattern on the computer). This machine makes lithography masks on 4” x 4” squares.

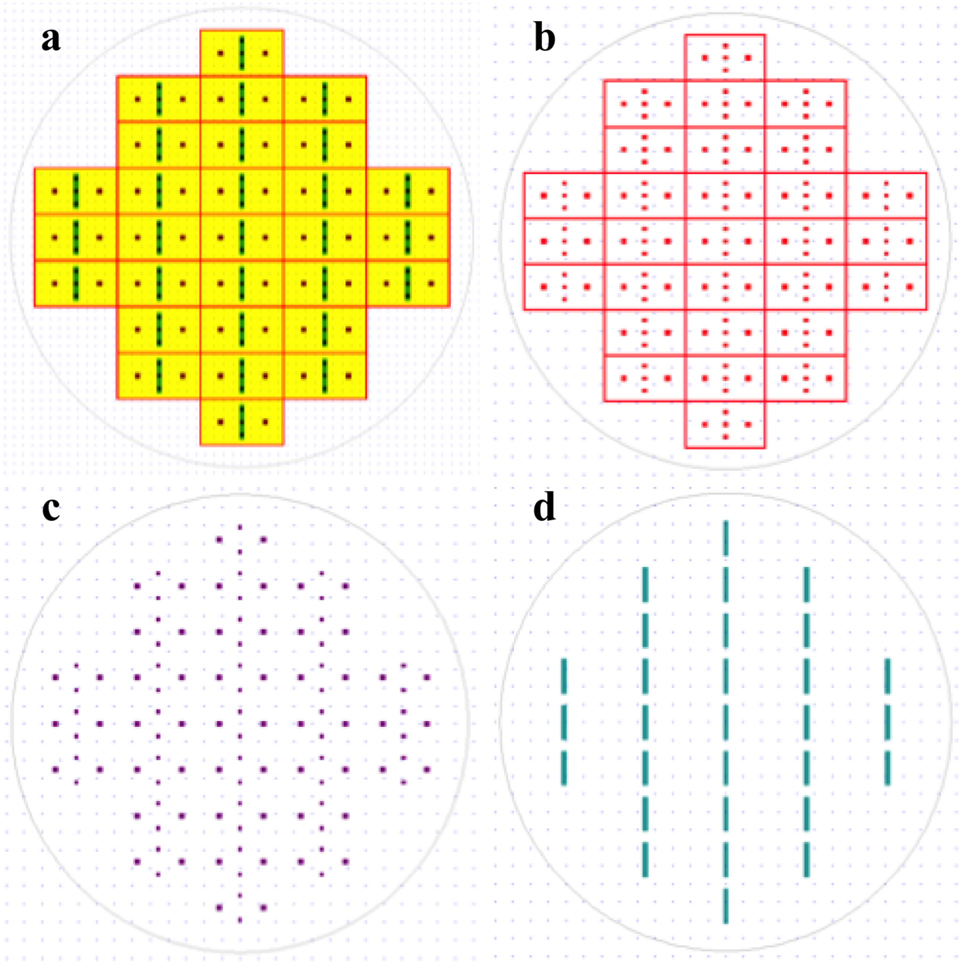

Figure A2: Masks for the out back piece. The whole features (a) and the three masks (b, c, d) for the out back piece.

3. Develop Mask
    a. Place mask in a new batch of CD 30 for 1 min 15 s
        i. Agitate the mask every second

    ii. Should see parts of the mask etching away
    iii. Rinse in DI water and blow dry with N_2 gas

    CD-30 removes photoresist that is exposed.

  b. Place mask in CR 75 for 1 min 15 s
    i. CR 75 does not have to be replaced every time but should be changed if the etching is very slow
    ii. Agitate the mask every second
    iii. Sometimes it takes longer than 1 min 15 s, just continue to etch/ agitate until the mask looks the right
    iv. Rinse in DI water

    CR-75 removes chromium that is not covered by photoresist.

  c. Check the mask is etched all the way and there are defined lines on the mask. Use the microscope (make sure use filters to protect the photoresist which is not exposed) to look and continue to use CR 75 if there is cloudiness along the edges.
  d. Place mask in developer (AZ 400T) for 15 min
    i. Rinse and dry with N_2.

    AZ 400T is a stripper that removes photoresist on the pattern.

- ❖ The mask made is pretty robust and can be used years and years later. When the mask gets dirty, use acetone bath to clean it, usually 10-15 min. When it is covered with photoresist, use AZ 400T bath to clean it, usually 10-15 min.

2nd Step: Back side etch (RIE II for silicon nitride and KOH bath for silicon using mask Fig. A1(b) and A2(b))

1. Clean the wafer with acetone and isopropanol (make the acetone and isopropanol overlap for a few seconds). Dry. Do this for both sides. If the

substrate is silicon, clean in BOE bath for 30 s, which attacks any silicon oxide that has formed on top. BOE is dangerous, so make sure you have been instructed before you do this step. Rinse with DI water. Make sure the water is flowing. Here since silicon is covered with silicon nitride and BOE can attack silicon nitride, so we ignore the BOE both.

2. Apply photoresist (NR-9) one both sides. Using the spinners at 4000 rpm for 40 s, with acceleration set to be biggest. Blinking pressure reading means vacuum is on, blinking 'VACUUM' means the vacuum is off.
    a. Turn on the hotplates to 150 ^{o}C and 100 ^{o}C
    b. Use a chuck and place the wafer on the spinner. Then press the vacuum button to hold it there.
    c. Use a pipette to apply NR-9 to the wafer, here you can pour directly at a low position, avoiding any air bubble
        i. Apply to the front side of the wafer
        ii. Be careful to not over apply because if the NR-9 flows over the wafer it will be pulled in by vacuum and adhere to the back of the wafer.
        iii. If the chuck becomes sticky, use IPA or acetone to clean off the photoresist.
        iv. Replace the blue liners in your spinner after use
    d. Prebake on hotplate with the front side up for 1 min @ 150 ^{o}C
    e. Then apply photoresist to the back side of the wafer
    f. Prebake on the hotplate with the back side up for 1 min @ 150 ^{o}C

❖ You can change the thickness of the deposited photoresist might by spining faster or slower. To set the timer on the spinner, press F1 (the menu should start flashing) and use arrow keys to set the RPM and time. Then press F1 AGAIN to leave edit mode and press start. The timer should start and the spinner will stop at the designated time. Now you should see the wafer as the following picture. Blue is silicon, brown is silicon nitride, purple is photon resist.

3. Expose the back side of the wafer using the MJB3
   a. Expose in MJB3 for the correct time (first check and test the time needs to be exposed after switching to a new lamp, the exposure time is 10-30 s, probably 15 s)
      i. Load the mask so that the chromium (silver) side ends up and purple (photoresist) side down
      ii. Load the wafers with the back side up.
      iii. Use the microscope and the computer to line up the mask so that the patterns are aligned (Here we do not need to align the pattern, but the lines needs to be collinear or vertical with the Si wafer direction because the etching process takes place in a certain direction.)
   b. Post-bake on hotplate for 1 min @ 100 ^{o}C
   c. Develop using DI water 5 s, RD6 10 s, DI water 5 s. NOTE: make sure water and RD6 overlap for a few seconds, but use RD6 exclusively for 10 s.
   d. I should be able to see visually where the photoresist has been washed away. Use microscope (using filter)

- The developing time is related to the thickness of the photoresist. If you want less or more photoresist then the developing time should change accordingly. Now the wafer should look like the following picture.

4. RIE II to ablate 300-nm silicon nitride (First check and test the time needed to etch 300-nm Silicon nitride)
   a. Use recipe suggested on directions: file cnloxide (recipe: 50 mTorr/150 W, 5 CHF_3 + 15 CF_4)
   b. Load the wafers 2-3 cm to the right of center of the glass plate for best results.
   c. Load wafers photoresist side up.
   d. You cannot set an etch time on the RIE II so you will have to manually stop it at the correct etching time by pressing END STEP. If you do not, it will run for a full 60 min.
   e. Wafers should appear silver in the center, this means you etched down to the Si layer. Make sure that the rest of the wafer remains purple (not silver) or that portion will also etch in KOH
   f. While RIE II is running, turn on KOH bath.
   g. Make sure you wash off any remaining photoresist on both sides using acetone + DI water (make sure you do this before the final KOH bath)

Now the wafer should look like the following picture.

- The first time I made those cells RIE II etching time for 300 nm is 15 min, for 270 nm is 10.5 min.

  Later the machine has some problem, the plasma changed to red means there might be O_2 plasma. Then etching time changed to 9 min for 270 nm.

  Last time etching time: Mask I 15 min (300 nm) Mask II 20 min (300 nm) Mask III 10.5 min (~270 nm) for good plasma and 9 min (~270 nm) for O_2 plasma. Etching 300 nm using O_2 plasma takes 12 min.

5. KOH bath for 15 hours @ 80 °C.

Ask for a Teflon basket to prevent the samples dropping into the bath. Be careful, as KOH is a dangerous chemical that we are heating. Use the right protection (lab coat, gloves, glasses). Avoid spilling. You can always etch more lately if it is not totally etched away.

   a. KOH bath takes 20-25 minutes to heat up
   b. Remember to fill the bath with water every few hours to keep constant temp and prevent shorting. You can use the DI water ‘gun’ (open the valve before using it and close it when you’re done). If it is full, then it can last for a whole night.
   c. 1 hour prior to removing samples, turn on the 3 bath rinse using the large timer (looks like a clock) on the outside of the fume hood. This will ensure clean water for your rinse.
   d. Remove wafers carefully and rinse in 3 bathes rinse on left of fume hood.

        i. Be careful: make sure to lift the wafers very slowly because the viscosity of the water could break the wafers.

    e. Filters should appear transparent in the middle, if not, continue to etch until they are.

    f. Dry wafers, but be very careful. The wafers are fragile and you might break them. Dry from a large distance and from the side.

- KOH does not etch Silicon nitride (<1nm/ hour) and etches Si at ~24 microns/h

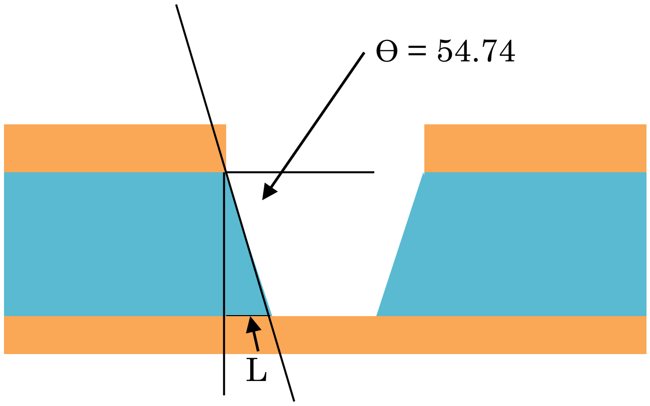

Si is anisotropic etching

Wafer thickness H = 370 µm

<u>Note:</u>

Heidelberg mask needs to be designed larger than the actual window itself because KOH etches at an angle. You start larger than you need and end up with the right size of silicon nitride window on the bottom.

$L = H / \tan \Theta = 370\ \mu m / \tan(54.74) = 262\ \mu m$

$2L = 524\ \mu m$

The size of liquid holes is 1000 um (actually 480 um), the opening for the gas holes and window is 700 um (actually 180 um), the gas channel is 1000 * 7000 um. All holes are one-way etching.

3rd step: Front side etch (RIE II for Silicon nitride using mask Fig. A1(c) and A2(c))

Using a tape (the special tape in CNL) to tape the back side of the wafer to prevent it from breaking apart in the following steps.

1. Apply NR-9 (photoresist) on the front side
2. Expose the front side of the wafer using the MJB3 (maybe 15 s) needs careful alignment.
3. RIE II to ablate 300-nm Silicon nitride (First check and test the time to etch 300-nm Silicon nitride)

   Last time the etching time for normal plasma is 10.5 min, for O_2 plasma is 9 min.

4th step: Front side etch (RIE II for Silicon nitride using mask Fig. A1(d) and A2(d))

1. Apply NR-9 (photoresist) on the front side
2. Expose the front side of the wafer using the MJB3 (maybe 15 s) needs careful alignment.
3. RIE II to ablate 270-nm Silicon nitride (First check and test the time to etch 270-nm Silicon nitride)

   Last time the etching time for normal plasma is 20 min, for O_2 plasma is 12 min

- ❖ Check under microscope the structure of the pattern. Measure the thickness of the silicon nitride window using ellipsometer. Measure the deepness of the gas flowing channel using profilometer.

- Cleaning procedure for the wafer (even after all the patterns are developed): 1 Acetone & Isopropanol on spinner (take almost all organic away). 2 Nanostripper (Maybe 15 min @ 80 °C, take all organic materials away). 3 Supersonic in the bath usually take 10 to 15 min. Based on last time's experience, this step can very easily break the window, so carefully handle the wafer in this step.